Geometrically Nonlinear Aeroelastic Scaling

Anthony P. Ricciardi

Dissertation submitted to the Faculty of the
Virginia Polytechnic Institute and State University
in partial fulfillment of the requirements for the degree of

Doctor of Philosophy
in
Aerospace Engineering

Robert A. Canfield, Chair
Mayuresh J. Patil, Co-Chair
Rakesh K. Kapania
Ned Lindsley
Layne T. Watson

December 11, 2013
Blacksburg, Virginia

Keywords: Nonlinear, Aeroelasticity, Scaling

Geometrically Nonlinear Aeroelastic Scaling

Anthony P. Ricciardi

Abstract

Aeroelastic scaling methodologies are developed for geometrically nonlinear applications. The new methods are demonstrated by designing an aeroelastically scaled model of a suitably nonlinear full-scale joined-wing aircraft. The best of the methods produce scaled models that closely replicate the target aeroelastic behavior. Internal loads sensitivity studies show that internal loads can be insensitive to axial stiffness, even for globally indeterminate structures. A derived transverse to axial stiffness ratio can be used as an indicator of axial stiffness importance. Two findings of the work extend to geometrically linear applications: new sources of local optima are identified, and modal mass is identified as a scaling parameter. Optimization procedures for addressing the multiple optima and modal mass matching are developed and demonstrated. Where justified, limitations of commercial software are avoided through development of custom tools for structural analysis and sensitivities, aerodynamic analysis, and nonlinear aeroelastic trim.

Acknowledgments

I start this dissertation by acknowledging those who have helped me the past four and a half years. I'm sincerely grateful to Dr. Canfield, my committee chair and advisor, for his great patience and sound guidance. I appreciate that Dr. Canfield continued to support me, even when I was adamant about pursuing research outside of the specific area we originally planned. I'm also genuinely grateful to have Dr. Patil as my advisor and committee co-chair. His constant participation and guidance was also invaluable. Two good advisors are two assets. Our weekly meetings helped me though the tough challenges and, more importantly, shaped my perspective and outlook.[1]

I was fortunate to have a particularly engaged committee. They cared enough to give detailed feedback on the work, and to be hard on me when I needed it. I would like to thank Dr. Lindsley for his uniquely positive attitude combined with his exceptional openness. I thank Dr. Kapania for his helpful suggestions and high standards, and I thank Dr. Watson for his brilliant attention to detail and his frequently outspoken but always sound input.

The collaboration with and support from the Multidisciplinary Science and Technology Center of the Air Force Research Laboratory was an exceptional privilege. I would especially like to thank Drs. Lindsley, Kolonay, Blair, and Camberos for their input. Input from the technical and strategic advisory committees was valuable. I am also grateful to the NASA Virginia Space Grant Consortium for their fellowship support.

I greatly appreciate my collaborators from the joined-wing flight test program. Charles Eger managed a seemingly impossible finite element model conversion and subsequent high-fidelity optimization study. Jeff Garnand-Royo documented and implemented a beautifully

[1] I have a few words of advice for future graduate students. Work hard. Choose your path carefully. Be skeptical of everything. You must be your own advocate, but great advisors are priceless. I'd highly recommend working with Dr. Canfield and/or Dr. Patil.

methodical flight test program. Jenner Richards wowed everyone by doing it all. He had, by far, the prevailing hand in designing, modeling, fabricating, and implementing every aspect of the project. I also thank Dr. Suleman for his guidance on the flight test program.

I would like to thank the great staff we have at Virginia Tech's Aerospace and Ocean Engineering Department. Especially Steve Edwards and Jonathan Spence for being so able and quick to resolve computer hardware and licensing issues. Rachel Hall Smith was always helpful with resolving administrative work and particularly helpful with bureaucratically challenging situations. I'm grateful for the office mates I've had in 327 Femoyer: Shaobin Liu, David Cross, Taekwang Ha, and Charles Eger. They provided necessary distractions on so many long days and late nights in the office. I would like to thank Dr. Woolsey for encouraging me to return for graduate school and for his continued advice along the way. I'm also grateful to Advanced Research Computing at Virginia Tech for maintaining the parallel cluster computing resources used for this work.

I would like to thank all of my family for their support and love. I especially want to thank my dad and stepmom, Ric and Sandy, for their frequent encouragement and writing help, my mom and stepdad, Mary and Bill, for their support and kindness, and my sister and brother-in-law, Teresa and Erik, for being there for me. I have to give a special thanks to my girlfriend, Erin, for taking care of me every day. I also thank my friends, too many to mention, that make life more fun and enjoyable. Lastly, I thank the many students and teachers I have known. I've learned from all of you.

Anthony Ricciardi

Anthony Ricciardi
December, 2013

This material is based on research sponsored by Air Force Research Laboratory under agreement number FA8650-09-2-3938. The U.S. Government is authorized to reproduce and distribute reprints for Governmental purposes notwithstanding any copyright notation thereon. The views and conclusions contained herein are those of the authors and should not be interpreted as necessarily representing the official policies or endorsements, either expressed or implied, of the Air Force Research Laboratory or the U.S. Government.

Contents

List of Figures

List of Tables

Chapter 1

Introduction

1.1 Aeroelastic Scaling Background and Thesis Statement

Experimental testing of aeroelastically scaled models is a common undertaking for flight vehicle development programs [29]. The typical objective is verification of predicted aeroelastic characteristics of the vehicle. In some cases, the objective is simply to verify computational models. For these cases, the model needs only to represent the full-scale vehicle in a qualitative sense. In other cases, the scaled model is intended to closely reproduce the aeroelastic response of the full-scale vehicle [29]. This more general form of the aeroelastic model design problem is the one addressed in this work.

Consider the scenario illustrated in Fig. 1.1. Engineers have developed a high-fidelity computational model representing a full-scale concept. The concept has a wingspan value of b. Wind tunnel size, cost, or safety considerations favor scaled aeroelastic testing rather full-scale testing. A half-span test article is built. Certain aeroelastic response quantities must be scaled in similar conditions. Flutter speed and divergence speed may be of interest. Static displacement is easily visualized in the graphic. If the full-scale has a predicted tip deflection Δ, the half-span model should have tip deflection $\Delta/2$ in scaled conditions.

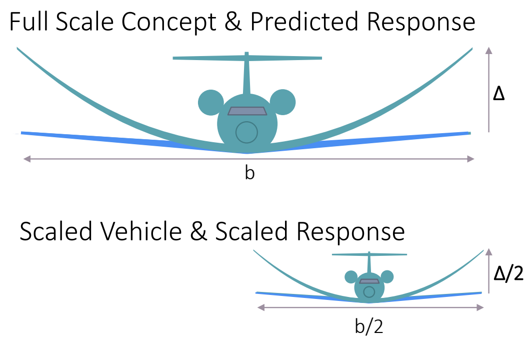

Figure 1.1: Full-scale and scaled vehicle with aeroelastic response.

Aeroelastic scaling requires consideration of aerodynamic and structural physics. Aerodynamic similitude is achieved analytically. Flight conditions such as airspeed and altitude are selected for matching scaled parameters like Froude number and density ratio, for example. Case specific scaling goals will dictate the nondimensional scaling parameter selection. Mach number and Reynolds number will be important parameters in respective cases with high compressibility and viscous effects. Geometric scaling of the outer mold line (OML) is typically required. Figure 1.2a shows an example of wings with geometrically scaled outer mold lines.

(a) Geometrically scaled outer mold lines.

(b) Geometrically scaled internal structure.

Figure 1.2: Design examples.

Structural similitude is not *realistically* achievable by geometrically scaling the structural components (Fig. 1.2b). Corresponding analytical scaling requirements will generally specify that a geometrically scaled structure should be made from materials that have unobtainable properties. There is also a high probability that the manufacturing techniques used for the full-scale design cannot be duplicated at a smaller scale. The only feasible option is to redesign the internal structure and optimize it such that it's scaled mass, damping, and stiffness properties are consistent with the full-scale vehicle.

An example redesign is illustrated in Fig. 1.3. The full-scale concept uses load bearing skins supported by spars, stringers, and ribs. Scaled models are often configured with non-load-bearing skin fairings and simple internal structures. The depicted ladder structure is one of several scaled model configurations recommended by Bisplinghoff *et al.* [12].

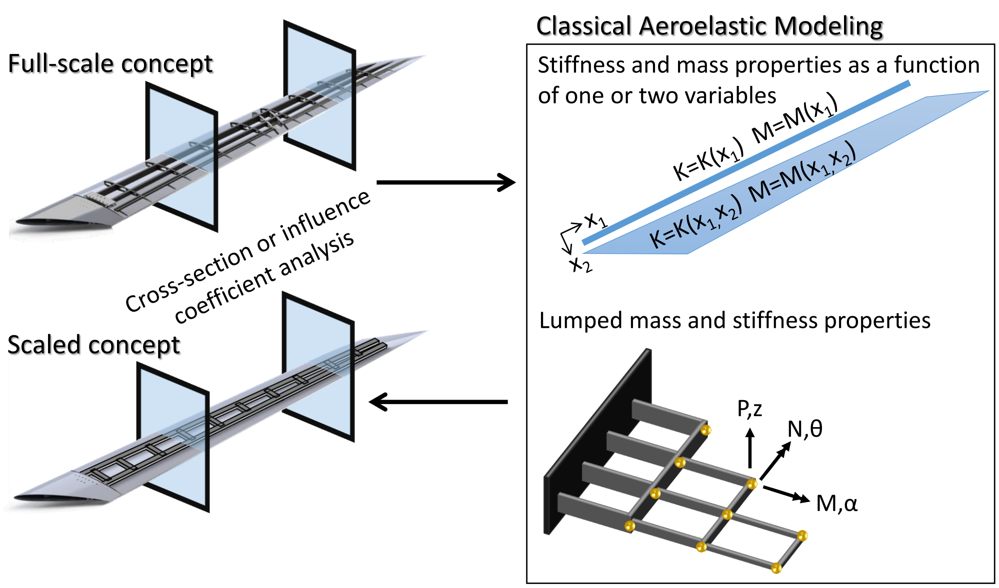

Figure 1.3: Classical aeroelastic modeling and scaling process.

Classical mathematical representation of aeroelastic systems uses strip theory aerodynamics and continuous or lumped structural models. Strip theory model properties are based on the OML geometry and flight conditions. Classical structural models are derived from cross-sectional or influence coefficient analysis of the physical concept. Aerodynamic scaling is achieved by geometrically scaling the OML and operating at an analytically scaled flight conditions. Classical structural scaling is achieved by designing the physical scaled model to reproduce the scaled mass and stiffness distributions derived from the cross-sectional analysis, or to reproduce a scaled subset of the lumped mass and stiffness properties of the full-scale vehicle.

Assumptions are made for classical aeroelastic modeling have scaled-model design implications. Axial and shear flexibilities are almost universally neglected in classical aeroelastic analysis. Wing-plane bending flexibility is also commonly neglected for low aspect ratio wings. As a result, scaling requirements derived from nondimensionalization of classical aeroelastic equations will reflect the assumptions made for deriving the equations. Flexibilities that are neglected will not be forced to match by the resulting scaling laws. Classical scaling methods have worked in practice for traditional applications, but the validity of the modeling assumptions needs verification for cases where geometric nonlinearities are important.

Modern practice in aeroelastic analysis has transitioned to higher fidelity computational models. Typically three-dimensional unsteady potential-flow codes are used for aerodynamics in aeroelasticity. Higher fidelity computational fluid dynamics (CFD) codes can also be used. Finite element models of variable fidelity are used for structural analysis. Figure 1.4a shows an example full-scale physical concept and an associated finite element mesh.

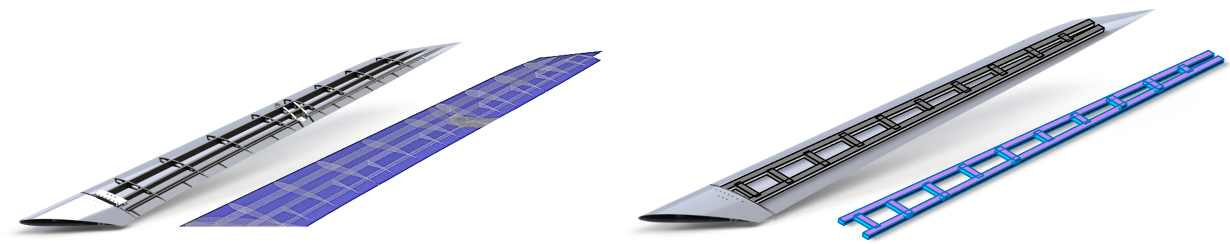

(a) Full-scale example. (b) Scaled example.

Figure 1.4: Concepts and modern computational models.

The particular mesh is made primarily of dense (enough that individual elements are not discernible in the figure) quadrilateral and triangular plate elements. A corresponding scaled physical model and finite element mesh are shown in Fig. 1.4b. Beam elements are used to model the ladder structure in this case. Mass from the non-load-bearing skins and other systems must be accounted for in the model. Because the structural meshes represent two models with physically different structural configurations, the discretized systems of equations are not directly compatible. Compatibility of the aerodynamic model, however, can be maintained because the OML is geometrically scaled.

Capability of the structural models is achieved by selection or interpolation of a compatible subset of nodes. The process is illustrated in Fig. 1.5. Analysis of the full-scale vehicle is used to produce modal degrees of freedom of the discrete subset with corresponding scaled modal masses, modal damping, and modal stiffnesses. The equation of motion can be written in modal coordinates

$$\left\langle \bar{\mathbf{M}} \right\rangle \{\ddot{\eta}\} + \left\langle \bar{\mathbf{C}} \right\rangle \{\dot{\eta}\} + \left\langle \bar{\mathbf{K}} \right\rangle \{\eta\} = \{\bar{\mathrm{F}}\}, \tag{1.1}$$

where $\langle \bar{\mathbf{M}} \rangle$ is a diagonal matrix of nondimensional modal masses, $\langle \bar{\mathbf{C}} \rangle$ is a diagonal matrix of nondimensional modal damping coefficients, $\langle \bar{\mathbf{K}} \rangle$ is a diagonal matrix of nondimensional modal stiffnesses, $\{\eta\}$ are modal degrees of freedom of the discrete subset, and $\{\bar{\mathrm{F}}\}$ is a vector of scaled modal forces. In the modern approach, structural scaling is achieved by selection of a discrete subset and modal degrees of freedom that capture the relevant global structural properties of the full system, and optimizing the scaled vehicle such that the nondimensional modal masses, damping coefficients, and stiffnesses match the full-scale vehicle.

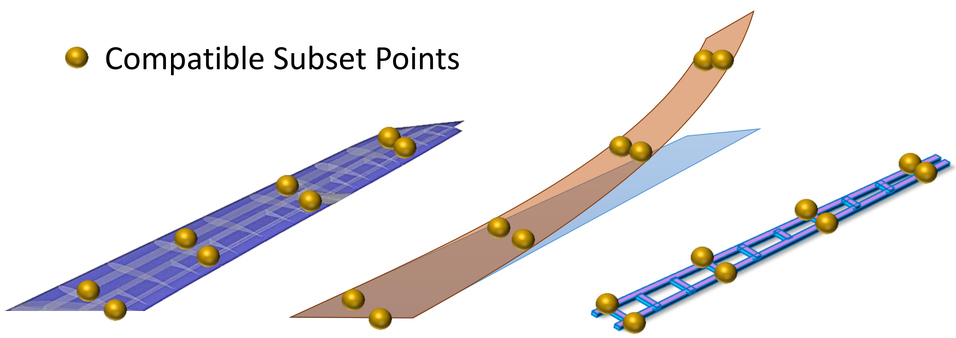

Figure 1.5: Compatible discrete subsets and example modal degree of freedom.

A primary benefit of using the modern scaling approach over the classical scaling approach is the ability to base the scaled vehicle optimization on current-practice higher-fidelity aeroelastic analysis. Development of these aeroelastic models is already part of the existing design process, so scaling analysis and optimization may be performed with the same tools used for design and certification. The modern scaling approach avoids detailed cross-sectional analysis, which is difficult for complicated structures with spanwise taper and twist, and modern structures with anisotropic composite layups. Figure 1.6 shows the exploded view of a modern composite wing section.

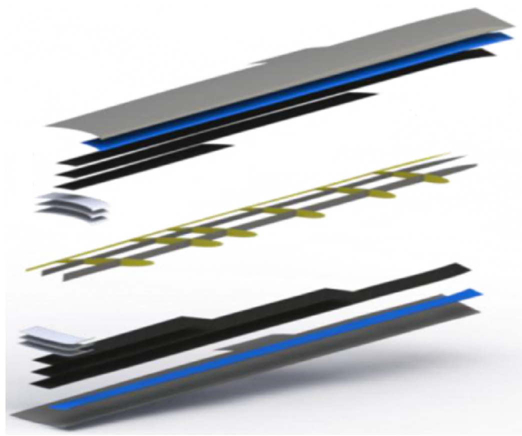

Figure 1.6: Modern composite wing construction concept.

Methods for calculating composite cross-sectional properties exist [77], but such calculations are not part of the design and certification analysis of all applications. The cross-sectional analysis may require development and training for processes that are otherwise not part of the existing design practice. Certain three-dimensional effects, such as warping restraint from ribs, are not captured with cross-sectional analysis; higher-fidelity three-dimensional analysis is required for cases where these effects are important.

The most common practice for modern aeroelastic scaling is to use a truncated number of the vibration mode shapes from the target full-scale model as the modal degrees of freedom for the scaled model optimization. An observed benefit of this approach is the automated selection of full-scale vehicle system-orthogonal modal degrees of freedom that are most likely to participate in lower frequency linear dynamics. A drawback is truncation may omit information that becomes important when geometric nonlinearity is significant. The truncation of higher frequency mode shapes in the modern aeroelastic scaling approach can be considered analogous to not modeling certain flexibilities (e.g., axial and shear) in the classical analysis and scaling approach.

The question of this dissertation: are the assumptions made for the classical and modern aeroelastic scaling methods valid for applications where geometric nonlinearity is important? If not, how do the methods need to be adjusted?

1.2 Geometric Nonlinearity

The geometric nonlinearity of interest is due to nonlinear strain-displacement kinematics and follower forces. Coupling between stiffnesses and internal loads is an important nonlinear kinematic effect. A prominent example of this is beam transverse stiffness and axial force coupling. Consider the joined beam case in Fig. 1.7.

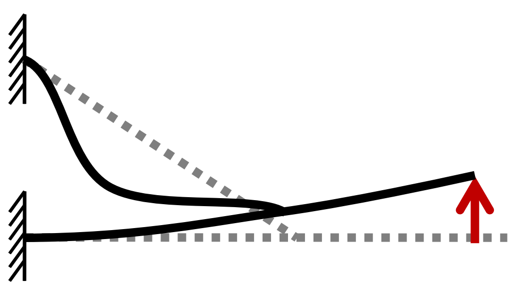

Figure 1.7: Indeterminate structure.

Axial force is dependent on the stiffnesses for statically indeterminate structures. An area of concern with existing scaled model design methodologies is inherit neglect of certain stiffnesses that are known to be insignificant in geometrically linear applications. In the case of classical aeroelastic scaling, assumptions made in the modeling formulation (e.g., ignoring axial flexibility) may result in scaled internal forces that do not match the target model for globally indeterminate structures. For modern aeroelastic scaling, truncation of high frequency mode shapes may have a similar affect.

Although geometric nonlinearities were not considered in their development, traditional scaled model design methodologies are sound with regard to geometric nonlinearities other than coupling between stiffnesses and internal loads. Large angle kinematics will scale automatically with a consistent global geometry, and follower forces will scale with scaled aerodynamics and a structure that matches the scaled response of the target model.

1.3 Joined-Wing Flight Test Motivation

Needs for a next generation intelligence, surveillance and reconnaissance (ISR) aircraft have inspired the joined-wing SensorCraft concept [46]. The joined-wing configuration provides an ideal platform for housing wing-embedded sensor apertures in an arrangement that provides 360° of radar coverage. The configuration also has potential for performance enhancing structural weight savings. Joining the forward and aft wings introduces an indeterminate load path and unique geometric nonlinearities.

A mission optimized SensorCraft concept is shown in Fig. 1.8. Blair *et al.* [13] optimized the model considering a wide range of mission requirements while modeling the inherent nonlinearities.

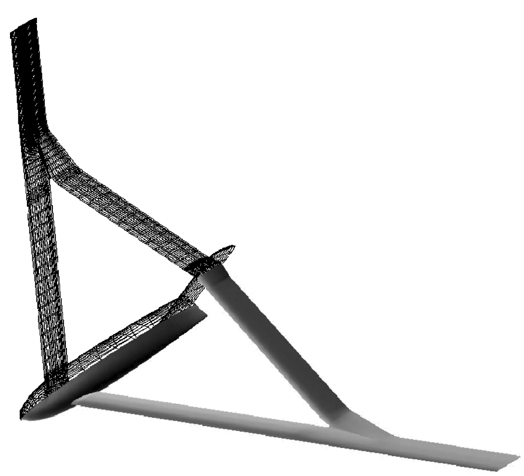

Figure 1.8: Mission optimized joined-wing concept [13].

The author of this work inherited the optimized finite element model and applied his custom nonlinear static aeroelastic trim analysis to study the response of the model. Results generated from the nonlinear trim analysis are shown in Fig. 1.9.

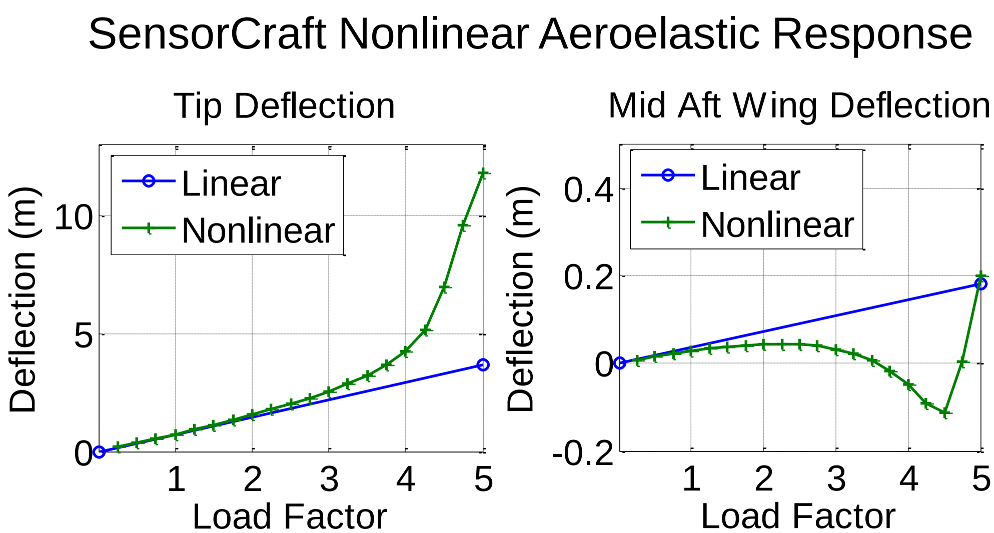

Figure 1.9: Nonlinear aeroelastic trim response of the mission optimized joined-wing concept.

Linear and nonlinear deflections of the wing tip and aft wing center are plotted. At $5g$, tip deflection is roughly three times what is predicted by linear analysis. The aft wing experiences a double reversal. The first nonlinear buckling mode presents as concave down behavior, followed by a rapid reversal as load carrying capacity is lost.

This unique joined-wing nonlinear aeroelastic behavior has never been demonstrated in flight. This work was performed in conjunction with a related flight test program [66, 22]. Flight demonstration and measurement of joined-wing nonlinear responses is a key goal of the collaborative research project. Richards *et al.* [64] successfully completed a flight demonstration program of a stiff $1/9^{\text{th}}$ scale model. The model was designed to have rigid flight dynamics representative of a full-scale AFRL/Boeing concept. Figure 1.10 shows the stiff scaled vehicle. The next phase of the project requires that the structure be modified such that the static aeroelastic response will show measurable nonlinearity in flight. Currently there is no requirement for the vehicle to be aeroelastically scaled based on a target design.

Nevertheless, nonlinear optimization techniques developed for this work are being adjusted to suit the specific nonlinear aeroelastic design needs of the flight test. Nonlinear aeroelastic trim analysis developed for scaling verification is also being used for analysis and design of the flight test vehicle.

Figure 1.10: Stiff SensorCraft geometrically scaled to 1/9$^{\text{th}}$ of a Boeing/AFRL concept [4].

Literature review during efforts leading up to the flight test program exposed a gap in the area of nonlinear aeroelastic scaling. Nonlinear scaling methodologies are needed for designing scaled wind tunnel or flight test models that require a nonlinear aeroelastic response that is representative of a full-scale design. Related applications include extremely high aspect ratio aircraft and aircraft with indeterminate load paths, such as joined-wing, strut-braced wing, and truss-braced wing configurations. All of these have been proposed as technologies that could revolutionize transport, cargo, and ISR aircraft [32, 11, 46].

1.4 Related Scaling Work

The foundations of dimensional analysis began with Fourier in the early nineteenth century. Revisions for successive releases of *Analytical Theory of Heat* [27] directly addressed previous ambiguity in units. A table of dimensions was used to list physical quantities in terms of fundamental or primary quantities. Interest faded until a resurgence towards the end of the nineteenth century. Rayleigh [39] developed the method of dimensions. He showed that the period of small amplitude vibrations was proportional to time$^{-\frac{1}{2}}$, mass$^{\frac{1}{2}}$, and length$^{\frac{1}{2}}$. He observed that proportionality held without regard to units.

Rayleigh initiated an intense development period for dimensional analysis [47]. Work continued by a number of scientists and engineers, most notably Carvallo [17] and Vaschy [72, 73]. Carvallo nondimensionalized a generator power equation. He specified that the general equation would hold for any similar system. Carvallo presented the theorem that any characteristic equation containing three or fewer primary quantities could be scaled. Vaschy provided a more general formulation for a similar theorem. Vaschy did not limit the number of primary quantities. The theorem was demonstrated on the classical pendulum equation and on a telegraphy equation with four primary quantities.

Buckingham's [16] 1914 paper presented the Π Theorem. The theorem is not substantively different from that of Vaschy, but a new proof was provided. Similarity examples demonstrated use of the theorem for scaling. The foundation of classical dimensional analysis and similitude was in place by the 1920's. A monograph by Bridgman [15] served to clarify and consolidate the developments. The work remains a classic in the area of dimensional analysis and similitude [47].

In 1955 Bisplinghoff *et al.* [12] published *Aeroelasticity*, which also remains a classic on the titled subject. The book documents classical structural and aerodynamic methods for fundamental aeroelastic analysis. No reference was made to the finite element method, which was not widely established in engineering at the time. Structural statics and dynamics were modeled using mostly analytical and assumed modes methods. Aerodynamics were modeled using potential flow aerodynamic theory, including options for unsteadiness, compressibility, and finite span effects. The final three chapters of the book provide essential guidance on classical aeroelastic model theory, model design and construction, and testing techniques. Fundamental dimensional analysis for similitude was reviewed and then applied. Dynamic beam equations were nondimensionalized in differential and integral form. Among others, nondimensional natural frequencies and mode shapes emerge as dimensionless parameters required to match for similarity. This will ultimately be a recurring trend that cascades to the current work. Beam examples were followed by static and dynamic aeroelastic models. The authors established the concept of geometric scaling of the aerodynamic shape for aerodynamic scaling. The chapter on model design and construction presents concepts for scaled model designs. It is made clear that typical experimental aeroelastic models do not use the same structural configuration as their full-scale counterparts. Several concepts were presented for models where elastic and inertial properties were assumed a function of one or two variables. The book ends with a chapter that details a range of testing techniques.

Expansion of aeroelastic scaling fundamentals is documented in the AGARD Manual on Aeroelasticity [75, 69]. Additional considerations such as compressibility and heat transfer effects are included. More on model construction and testing is provided.

French [28] used optimization combined with finite element modeling to design an aeroelastically scaled model. The stiffness of a low aspect ratio wind tunnel model was designed to match the stiffness of a target model. The optimization minimized the structural weight while satisfying displacement matching constraints (by constraining a common flexibility matrix). Physical static load tests validated the analysis and optimization. French and Eastep [29] modified the methodology presented in Ref. [28] to include scaling for dynamic aeroelasticity. A two-step optimization procedure was used. First, the wing structure was designed to minimize the differences in scaled static deflections between the design and target model. Then, assuming the stiffness design was complete and accurate, nonstructural masses were designed by constraining the reduced modal frequencies to match while minimizing the differences in mode shapes. Total nondimensional masses were also constrained to match. The technique was used to design a low aspect ratio wind tunnel model. Experimental results showed the wind tunnel model matched the target flutter speed and flutter mode.

Starting in the late 1990's, Friedmann, Presente, and others [60, 31, 59, 61, 58] published a series of papers on active flutter suppression of a two-dimensional wing section and associated scaling laws for incompressible and compressible flow. Freidmann and Peretz [30] extended the scaling work to modern aeroelastic computational models and showed that aeroservoelastic scaling laws for rotary aircraft can be obtained in a manner similar to fixed-wing aircraft.

Pototzky [56] developed a scaling procedure for a transonic wind tunnel model including aeroservoelastic effects. An experimental spring mounting system was directly incorporated in the aeroelastic equations. Scaling rules were applied to the aeroelastic equation formulated using modal coordinates. To verify the scaling process, the root locus from the full sized vehicle model was compared to the root locus from the scaled wind tunnel model. Agreement was satisfactory.

Pereira *et al.* [53] developed a scaling methodology for a joined-wing wind tunnel model. The scaled structure was designed by optimizing the scaled natural frequencies of the model to match the full-scale design. Normalized flutter speed of the scaled model matched the full-scale aircraft, but the aeroelastic frequencies did not match around or above flutter speed. Ground vibration tests substantiated the computational results.

Bond *et al.* [14] demonstrated that matching scaled natural frequencies alone is insufficient. This was accomplished by designing two cantilevered wing models to have matching natural frequencies, but radically different frequency domain aeroelastic responses. Separately, a nonlinear aeroelastic scaling methodology was developed for a joined-wing model. The structure was designed by simultaneously matching the first three natural frequencies, the first three mode shapes, and the first buckling eigenvalue. The aeroelastic frequencies and damping of the resulting scaled model matched well throughout the velocity profile. The nonlinear static response of the scaled model matched reasonably well up to 60% of the buckling load. Valuable recommendations were provided for future nonlinear aeroelastic scaling efforts with aims at more consistent nonlinear matching. A suggested direct matching of the nonlinear response is used for this work.

Richards *et al.* [67] evaluated two linear scaling methodologies for a joined-wing flight test program. The program is discussed in the next section. The first methodology used a single-step direct modal matching. Similar to Bond *et al.* [14], natural frequencies and mode shapes were matched in a simultaneous optimization analysis. Design variables included structural stiffnesses and nonstructural masses. The second method decoupled the stiffness and nonstructural mass design variables. Following the methodology of French and Eastep [29], the structure was designed by matching scaled linear static deflections in the first optimization analysis. A subsequent optimization analysis matched the natural frequencies and modes by designing nonstructural masses. Both methods were demonstrated with a prototype problem. The authors concluded that both methods converged to an acceptable result, but the single-step method had a greater computational cost.

Wan and Cesnik [74] derived scaling parameters for scaling a transient aeroelastic equation of motion that includes nonlinear stiffness due to large deformations and prestress. Two scaled designs of a highly flexible flying wing aircraft were derived and tested. One of the two was intentionally designed neglecting Froude number matching. Extensive verification including structural modes, nonlinear aeroelastic trim, linearized Phugoid stability at different payloads, and nonlinear transient gust response were presented. Results show that Froude number scaling should not be neglected. The model that included Froude number scaling showed responses that were in agreement with the full-scale model.

Wan and Cesnik's [74] structural models are defined by beam properties. Full control over all distributed properties of the model, including axial stiffness, was assumed. The computational aeroelastic models served to verify the analytical scaling work, which can be closely identified with classical aeroelastic scaling. Relation of the scaled distributed properties to a physical scaled model was not an aim of the paper.

This work addresses the application of a modern scaling approach to geometrically non-linear applications. Design of the physical scaled model is considered as part of the scaling methodology. Necessity of design control of the axial stiffness is evaluated for indeterminate structures and reviewed in the context of both modern and classical scaled model design requirements.

1.5 Related Nonlinear Aeroelastic Analysis Developments

Nonlinear static aeroelastic trim analysis of high-fidelity built-up structures is not supported by any commercial analysis or released research code. Several research codes have been developed that directly couple a nonlinear beam element structural model with a linear aerodynamic model. Patil and Hodges [52] published the baseline Nonlinear Aeroelastic Trim And Stability for HALE Aircraft (NATASHA) formulation in 2006. The code uses Hodges [36, 37] geometrically exact intrinsic beam structural model coupled with Peters [54, 55] airloads and inflow model. Nonlinear Aeroelastic Simulation Toolbox (NAST) was developed in a parallel effort. Cesnik and Brown [18, 19] introduced the strain-based structural modeling approach. NAST also incorporates the Peters [54, 55] aerodynamic formulation. Drela [20] developed ASWING, a licensed integrated analysis tool. The code uses unsteady lifting line aerodynamics and a structural model based on geometrically nonlinear isotropic beam analysis.

Outside of these released codes, in-house research codes have demonstrated nonlinear aeroelasticity. Bendiksen [6, 7, 8] directly coupled simple plate structures with Euler aerodynamics. Farhat *et al.* [25] loosely coupled an Euler/Navier-Stokes solver with a nonlinear finite element solver. Loose coupling can be assisted by code coupling interfaces such as MpCCI or OpenFSI. Nikbay *et al.* [51] used MpCCI to loosely couple Abaqus, a commercial finite element solver, with FLUENT, a commercial CFD code. Bhasin [10] coupled MSC Nastran with an unsteady vortex lattice aerodynamic code using the OpenFSI interface.

Verification of nonlinear aeroelastically designed or scaled models requires aeroelastic analysis with high fidelity structural models not limited to beam elements. Options other than beam based structure require in-house development of a tightly coupled aeroelastic code, or in-house development of or integration with a code coupling interface. This work developed a custom aeroelastic coupling interface that loosely couples a newly developed vortex lattice code with MSC Nastran, a commercial finite element solver. MSC Nastran has the flexibility of a large element library. It can efficiently handle nonlinear analysis of high fidelity structural models. MSC Nastran has built-in aeroelastic capabilities that include the doublet lattice panel method. Unfortunately, the aeroelastic functionality in MSC Nastran does not support nonlinear problems. The coupling interface allows the user to access MSC Nastran's powerful nonlinear static analysis for aeroelastic problems. Formulation of the vortex lattice analysis and coupling interface are detailed in the methodology chapter. Code verification is provided in the results section.

1.6 This Document

In this chapter, aeroelastic scaling was introduced and traditional methods for scaled-model design were discussed. Possible limitations of traditional methods for geometrically nonlinear applications were identified. The work was motivated by reviewing an associated joined-wing flight test program. Previous work in aeroelastic scaling and high-fidelity nonlinear aeroelastic analysis was reviewed.

Chapter 2 covers the methodologies used for aeroelastic analysis and scaling. The dynamic aeroelastic equation of motion is nondimensionalized and scaling parameters are identified. Optimization techniques used for scaled model design are detailed. Aeroelastic analysis and aeroelastic models are discussed.

Results are presented in Chapter 3. Verification of and validation of aerodynamic analysis, and verification of structural and aeroelastic analyses are provided. Optimization techniques are demonstrated on the Svanberg [71] beam problem and compared to the known optimum. Scaling results for a joined-wing demonstration problem are provided for a systematic optimization approach and an approach that includes optimization of the nonlinear static response. Nonlinear aeroelastic trim response and linearized dynamic aeroelastic response are compared to the target full-scale model and used to assess the quality of the scaled-model designs. Internal loads sensitivities are studied using a simple frame with an analytic solution (of the linear response), and a beam model of the three-dimensional joined-wing demonstration problem. An illustrative discussion of multiple optima is provided. The final chapter summarizes conclusions and proposes future work.

Chapter 2

Methodology

2.1 Scaling Theory

Scaling theory is developed based on the geometrically nonlinear dynamic aeroelastic equation of motion,

$$[\mathbf{M}]\{\ddot{\mathrm{x}}\} + [\mathbf{K_{NL}}(\mathrm{x})]\{\mathrm{x}\} = [\mathbf{A_k}]\{\mathrm{x}\} + [\mathbf{A_c}]\{\dot{\mathrm{x}}\} + [\mathbf{A_m}]\{\ddot{\mathrm{x}}\} + [\mathbf{M}]\{\mathrm{a_g}\}, \tag{2.1}$$

where $\{\mathrm{x}\}$ is a vector of elastic and rigid body degrees of freedom, $[\mathbf{M}]$ is the mass matrix, $[\mathbf{K_{NL}}]$ is the stiffness matrix (a function of $\{\mathrm{x}\}$ due to nonlinear kinematics), $[\mathbf{A_k}]$, $[\mathbf{A_c}]$, and $[\mathbf{A_m}]$ are aerodynamic matrices, and $\{\mathrm{a_g}\}$ is a vector containing gravitational accelerations for each degree of freedom. $\dot{()}$ indicates differentiation with respect to time. Nonlinear kinematics don't introduce different physical quantities than those needed for compatible linear kinematic formulations,[74] so the nondimensional parameters are the same for compatible linear and geometrically nonlinear formulations. There are, however, possible issues with existing scaled model design methodologies that were originally developed for applications with essentially linear kinematics. The derivation will help later discussion on that topic. For the purposes of nondimensionalization, we will consider the linearized dynamic aeroelastic equation of motion,

$$[\mathbf{M}]\{\ddot{\mathrm{x}}\} + [\mathbf{K}]\{\mathrm{x}\} = [\mathbf{A_k}]\{\mathrm{x}\} + [\mathbf{A_c}]\{\dot{\mathrm{x}}\} + [\mathbf{A_m}]\{\ddot{\mathrm{x}}\} + [\mathbf{M}]\{\mathrm{a_g}\}, \tag{2.2}$$

where $[\mathbf{K}]$ is the linearized stiffness matrix. For Eq. (2.2) to be nondimensionalized, the components of each coefficient matrix must have unified dimensions. Coefficient matrix dimensions are unified using a dimensional transformation matrix, $[\mathbf{T}]$, that is derived to nondimensionalize the physical coordinate vector. For example, if the physical coordinates are two displacement and two rotation degrees of freedom,

$$\{\mathrm{x}\} = \begin{Bmatrix} h_1 \\ \theta_1 \\ h_2 \\ \theta_2 \end{Bmatrix}, \tag{2.3}$$

then a nondimensional vector of physical coordinates $\{\bar{\mathrm{x}}\}$ is attained using

$$\{\mathrm{x}\} = [\mathbf{T}]\{\bar{\mathrm{x}}\} = \begin{bmatrix} b & 0 & 0 & 0 \\ 0 & 1 & 0 & 0 \\ 0 & 0 & b & 0 \\ 0 & 0 & 0 & 1 \end{bmatrix} \begin{Bmatrix} h_1/b \\ \theta_1 \\ h_2/b \\ \theta_2 \end{Bmatrix} = \begin{Bmatrix} h_1 \\ \theta_1 \\ h_2 \\ \theta_2 \end{Bmatrix}. \tag{2.4}$$

The coefficient matrices are uniformly dimensionalized by premultiplying by $[\mathbf{T}]^T$ and post-multiplying by $[\mathbf{T}]$. Take the mass matrix for example

$$[\breve{\mathbf{M}}] = [\mathbf{T}]^T[\mathbf{M}][\mathbf{T}], \tag{2.5}$$

where $\breve{()}$ denotes a matrix or vector with uniform dimensions. Gravitational acceleration is modified similarly,

$$\{\mathrm{a_g}\} = [\mathbf{T}]\{\breve{\mathrm{a}}_\mathrm{g}\}. \tag{2.6}$$

Equation (2.2) is uniformly dimensionalized by substituting for $\{\mathrm{x}\}$ and $\{\mathrm{a_g}\}$ with the general forms of Eqs. (2.4) and (2.6) and premultiplying by $[\mathbf{T}]^T$

$$[\breve{\mathbf{M}}]\{\ddot{\bar{\mathrm{x}}}\} + [\breve{\mathbf{K}}]\{\bar{\mathrm{x}}\} = [\breve{\mathbf{A}}_\mathbf{k}]\{\bar{\mathrm{x}}\} + [\breve{\mathbf{A}}_\mathbf{c}]\{\dot{\bar{\mathrm{x}}}\} + [\breve{\mathbf{A}}_\mathbf{m}]\{\ddot{\bar{\mathrm{x}}}\} + [\breve{\mathbf{M}}]\{\breve{\mathrm{a}}_\mathrm{g}\}. \tag{2.7}$$

Each term in Eq. (2.7) has units of work, or force×length. Nondimensional deformations in terms of the modal coordinates are

$$\{\bar{\mathrm{x}}\} = [\Phi]\{\eta\}, \tag{2.8}$$

where $\{\eta\}$ is the vector of modal coordinates and $[\Phi]$ is the matrix of nondimensional mode shapes. The first six mode shapes are rigid body displacements. Mass and stiffness matrices are diagonalized using the bi-orthogonality property,

$$\langle \mathbf{m} \rangle = [\Phi]^T[\breve{\mathbf{M}}][\Phi], \tag{2.9}$$

$$\langle \mathbf{k} \rangle = [\Phi]^T[\breve{\mathbf{K}}][\Phi] = \left\langle \mathbf{m}\omega^\mathbf{2} \right\rangle, \tag{2.10}$$

where $\langle \omega \rangle$ is the diagonal matrix of modal frequencies. Aerodynamic coefficient matrices are modified equivalently

$$[\mathbf{a_k}] = [\Phi]^T[\breve{\mathbf{A}}_\mathbf{k}][\Phi], \tag{2.11}$$

$$[\mathbf{a_c}] = [\Phi]^T[\breve{\mathbf{A}}_\mathbf{c}][\Phi], \tag{2.12}$$

$$[\mathbf{a_m}] = [\Phi]^T[\breve{\mathbf{A}}_\mathbf{m}][\Phi]. \tag{2.13}$$

Using modal coordinates, the equation of motion is

$$\begin{aligned}\langle \mathbf{m} \rangle \{\ddot{\eta}\} + \left\langle \mathbf{m}\omega^{\mathbf{2}} \right\rangle \{\eta\} = \\ [\mathbf{a_k}]\{\eta\} + [\mathbf{a_c}]\{\dot{\eta}\} + [\mathbf{a_m}]\{\ddot{\eta}\} \\ + \langle \mathbf{m} \rangle [\Phi]^{-1}\{\breve{\mathrm{a}}_{\mathrm{g}}\}.\end{aligned} \tag{2.14}$$

Dimensions of the aerodynamic matrices and gravitational acceleration vector are moved outside as scalar coefficients,

$$\begin{aligned}\langle \mathbf{m} \rangle \{\ddot{\eta}\} + \left\langle \mathbf{m}\omega^{\mathbf{2}} \right\rangle \{\eta\} = \\ \frac{1}{2}\rho V^2 Sb \left([\bar{\mathbf{a}}_{\mathbf{k}}]\{\eta\} + \frac{b}{V}[\bar{\mathbf{a}}_{\mathbf{c}}]\{\dot{\eta}\} + \frac{b^2}{V^2}[\bar{\mathbf{a}}_{\mathbf{m}}]\{\ddot{\eta}\} \right) \\ + \frac{g}{b} \langle \mathbf{m} \rangle [\Phi]^{-1}\{\bar{\mathrm{a}}_{\mathrm{g}}\},\end{aligned} \tag{2.15}$$

where barred quantities are nondimensional. Mass is nondimensionalized using m_1, modal mass (uniformly dimensionalized as inertia) of the first mode,

$$\begin{aligned}\langle \bar{\mathbf{m}} \rangle \{\ddot{\eta}\} + \left\langle \bar{\mathbf{m}}\boldsymbol{\omega}^{\mathbf{2}} \right\rangle \{\eta\} = \\ \frac{1}{2}\frac{\rho Sb}{\mathrm{m}_1} V^2 \left([\bar{\mathbf{a}}_{\mathbf{k}}]\{\eta\} + \frac{b}{V}[\bar{\mathbf{a}}_{\mathbf{c}}]\{\dot{\eta}\} + \frac{b^2}{V^2}[\bar{\mathbf{a}}_{\mathbf{m}}]\{\ddot{\eta}\} \right) \\ + \frac{g}{b} \langle \bar{\mathbf{m}} \rangle [\Phi]^{-1}\{\bar{\mathrm{a}}_{\mathrm{g}}\},\end{aligned} \tag{2.16}$$

where $\langle \bar{\mathbf{m}} \rangle$ is a diagonal matrix of nondimensional masses with $\bar{\mathrm{m}}_1 = 1$. Time is nondimensionalized using ω_1, the modal frequency of the first mode,

$$\begin{aligned} \langle \bar{\mathbf{m}} \rangle \{\overset{\star\star}{\eta}\} + \left\langle \bar{\mathbf{m}}\bar{\boldsymbol{\omega}}^{\mathbf{2}} \right\rangle \{\eta\} = & \\ & \frac{1}{2}\frac{\rho S b}{\mathrm{m}_1}\frac{V^2}{\omega_1^2}\left([\bar{\mathbf{a}}_{\mathbf{k}}]\{\eta\} + \frac{\omega_1 b}{V}[\bar{\mathbf{a}}_{\mathbf{c}}]\{\overset{\star}{\eta}\} + \frac{\omega_1^2 b^2}{V^2}[\bar{\mathbf{a}}_{\mathbf{m}}]\{\overset{\star\star}{\eta}\} \right) \\ & + \frac{g}{\omega_1^2 b}\langle \bar{\mathbf{m}} \rangle [\Phi]^{-1}\{\bar{\mathrm{a}}_{\mathrm{g}}\}, \end{aligned} \tag{2.17}$$

where $\langle \bar{\omega} \rangle$ is a diagonal matrix of nondimensional modal frequencies, and $\overset{\star}{()}$ indicates differentiation with respect to nondimensional time $\tau = t\omega_1$. Rearranging the right hand side,

$$\begin{aligned} \langle \bar{\mathbf{m}} \rangle \{\overset{\star\star}{\eta}\} + \left\langle \bar{\mathbf{m}}\bar{\boldsymbol{\omega}}^{\mathbf{2}} \right\rangle \{\eta\} = & \\ & \frac{1}{2}\underbrace{\frac{\rho S b(b^2)}{\mathrm{m}_1}}_{\mu_1}\underbrace{\frac{V^2}{\omega_1^2 b^2}}_{1/\kappa_1^2}\left([\bar{\mathbf{a}}_{\mathbf{k}}]\{\eta\} + \underbrace{\frac{\omega_1 b}{V}}_{\kappa_1}[\bar{\mathbf{a}}_{\mathbf{c}}]\{\overset{\star}{\eta}\} + \underbrace{\frac{\omega_1^2 b^2}{V^2}}_{\kappa^2}[\bar{\mathbf{a}}_{\mathbf{m}}]\{\overset{\star\star}{\eta}\} \right) \\ & + \underbrace{\frac{gb}{V^2}}_{1/Fr^2}\underbrace{\frac{V^2}{\omega_1^2 b^2}}_{1/\kappa_1^2}\langle \bar{\mathbf{m}} \rangle [\Phi]^{-1}\{\bar{\mathrm{a}}_{\mathrm{g}}\}, \end{aligned} \tag{2.18}$$

three nondimensional parameters emerge: reduced frequency of the first elastic mode $\kappa_1 = \frac{\omega_1 b}{V}$, inertia ratio $\mu_1 = \frac{\rho S b(b^2)}{\mathrm{m}_1}$, and Froude number $Fr = \frac{V}{\sqrt{bg}}$. The final form of the nondimensional linear dynamic aeroelastic equation is

$$\begin{aligned} \langle \bar{\mathbf{m}} \rangle \{\overset{\star\star}{\eta}\} + \left\langle \bar{\mathbf{m}}\bar{\boldsymbol{\omega}}^{\mathbf{2}} \right\rangle \{\eta\} = & \\ & \frac{1}{2}\frac{\mu_1}{\kappa_1^2}\left([\bar{\mathbf{a}}_{\mathbf{k}}]\{\eta\} + \kappa_1[\bar{\mathbf{a}}_{\mathbf{c}}]\{\overset{\star}{\eta}\} + \kappa_1^2[\bar{\mathbf{a}}_{\mathbf{m}}]\{\overset{\star\star}{\eta}\} \right) \\ & + \frac{1}{Fr^2\kappa_1^2}\langle \bar{\mathbf{m}} \rangle [\Phi]^{-1}\{\bar{\mathrm{a}}_{\mathrm{g}}\}. \end{aligned} \tag{2.19}$$

For the scaled model to have a scaled linearized dynamic aeroelastic response, as governed by Eq. (2.19), the following derived nondimensional parameters are required to match the full scale model:

1. reduced frequency of the 1st mode κ_1,
2. inertia ratio μ_1,
3. Froude number Fr,
4. nondimensional modal masses $\langle \bar{\mathbf{m}} \rangle$,
5. nondimensional modal frequencies $\langle \bar{\omega} \rangle$
6. nondimensional mode shapes $[\Phi]$,
7. aerodynamic shape,
8. Mach number if compressibility effects are important, and
9. Reynolds number if viscous effects are important.

Items 7–9 are required for matching the aerodynamic matrices. Scaling of compressibility and viscous effects can be neglected for cases where it is reasonable to assume they will have a small influence. Length scale is specified based on experimental or manufacturing requirements. Item 7, the outer mold line, is scaled directly. Airspeed is selected to match the Froude number. The total mass of the vehicle must be constrained to provide a matching inertia ratio. Items 1 and 4–6 are matched by optimizing the modal response of the scaled model. It is the structural optimization that introduces the greatest complications for physically realizing the scaling requirements when designing the scaled model.

The first complication comes from likely structural configuration inconsistency. For example, a full-scale model that is designed using skins, spars, and ribs might have a scaled model that uses a ladder structure and skin fairings. When discretized, the finite element models will have different relative node locations and a different number of degrees of freedom. Thus, the discretized aeroelastic equations can never be matched exactly. A globally representative subset of nodes must be selected or interpolated, as shown in Fig. 1.5.

Once a representative subset is selected, a number of modal masses, modal frequencies, and mode shapes can be matched in the optimization. The number that is matched can only be a truncated number of the total number of vibration eigenpairs. The truncation is necessary for optimization feasibility and an unavoidable difference in the total number of degrees of freedom. The lower frequency vibration eigenpairs will typically dominate the low frequency linear dynamics, so it's easy to justify truncation for geometrically linear applications.

Eigenpair truncation is a potential problem for geometrically nonlinear applications. Higher frequency eigenpairs will likely contain flexibility information (i.e., axial flexibility) that may be more important for geometrically nonlinear applications [38], especially if there are globally indeterminate load paths. This work provides recommendations for alternative modal coordinates that can be added to the scaled model optimization problem to capture important distributed mass and stiffness information that is not captured in the lower frequency vibration eigenpairs.

2.2 Scaling Optimization

2.2.1 Eigenvector Normalization

The free vibration eigenpair solution provides a matrix of nondimensional mode shapes $[\mathbf{\Phi}] = [\{\phi_1\}, \{\phi_2\}, ..., \{\phi_\mathrm{n}\}]$. Diagonalization of the nondimensional mass matrix provides a set of modal masses for the system in modal coordinates

$$\langle \bar{\mathbf{m}} \rangle = [\mathbf{\Phi}]^T [\bar{\mathbf{M}}][\mathbf{\Phi}]. \tag{2.20}$$

The magnitude of $\{\phi_\mathrm{j}\}$ can be selected for an identity modal mass matrix using

$$\{\check{\phi}_\mathrm{j}\} = \frac{\{\phi_\mathrm{j}\}}{\sqrt{\{\phi_\mathrm{j}\}^T \bar{\mathrm{m}}_\mathrm{j} \{\phi_\mathrm{j}\}}}, \tag{2.21}$$

where $\{\check{\phi}_\mathrm{j}\}$ are mass normalized eigenvectors. Modal coordinates based on $\{\check{\phi}_\mathrm{j}\}$ produce an identity modal mass matrix

$$\langle \mathbf{1} \rangle = \langle \check{\mathbf{m}} \rangle = [\check{\mathbf{\Phi}}]^T [\bar{\mathbf{M}}][\check{\mathbf{\Phi}}]. \tag{2.22}$$

Note that buckling eigenvectors can be system normalized consistently using the elastic or differential stiffness matrices. For optimization, it is important that system normalized eigenvectors are sign consistent (opposite sign eigenvectors will still be system normalized). The following correction ensures sign consistency with target eigenvectors,

$$\{\hat{\phi}^\mathrm{s}_\mathrm{j}\} = \frac{\check{\phi}^t_{j_{k_j}} \check{\phi}^s_{j_{k_j}}}{|\check{\phi}^t_{j_{k_j}} \check{\phi}^s_{j_{k_j}}|} \{\check{\phi}^\mathrm{s}_\mathrm{j}\}, \tag{2.23}$$

where k_j is the component of $\check{\phi}^t_j$ with the largest absolute value.

2.2.2 Format of Objective Functions

The scaled vehicle is designed by minimizing normalized differences between the target response $\{\varphi^{\mathrm{t}}\}$ and scaled model response $\{\varphi^{\mathrm{s}}\}$. The system responses are static deformation modes or system matrix normalized eigenvector modes. $\{\varphi\}$ includes nondimensional displacements and rotations

$$\{\varphi\} = \left\{ \begin{array}{c} \frac{1}{b}\{\mathrm{h}\} \\ \{\theta\} \end{array} \right\} = \left\{ \begin{array}{c} \{\bar{\mathrm{h}}\} \\ \{\theta\} \end{array} \right\}. \tag{2.24}$$

Options for normalizing the sum of the differences between the responses are covered in the following subsections.

SSR with Full Normalization

Sum of the squares of the residuals (SSR) with full normalization is the most basic scheme for quantifying differences in the responses,

$$\mathcal{S}_F\left(\varphi^t, \varphi^s\right) = \left(\frac{\varphi_i^t - \varphi_i^s}{\varphi_i^t}\right)^2, \tag{2.25}$$

where repeated indices are summed. The format requires $\{\varphi^{\mathrm{t}}\}$ and $\{\varphi^{\mathrm{s}}\}$ to be provided with consistent scaled magnitudes (i.e., nondimensional static deformations or nondimensional system matrix normalized eigenvectors). Each term in the response is normalized by its target value, and thus each response term is given equal weight in the objective function. The major drawback of this scheme is the likelihood of near singularities. If target values approach zero, the corresponding objective terms approach infinity.

SSR with Target Maximum Normalization

Sum of the squares of the residuals with target maximum normalization avoids singularities,

$$\mathcal{S}_T\left(\varphi^t,\varphi^s\right)=\left(\frac{\bar{\mathrm{h}}_i^t-\bar{\mathrm{h}}_i^s}{\|\{\bar{\mathrm{h}}^t\}\|_\infty}\right)^2+\left(\frac{\theta_i^t-\theta_i^s}{\|\{\theta^t\}\|_\infty}\right)^2, \tag{2.26}$$

where repeated indices are summed. Although the response terms are nondimensional, displacements and rotations remain physically different quantities. Independent normalization ensures equal weight between displacement and rotations, and equal weight between other eigenvector or static deformation modes. The objective value from $\mathcal{S}_T$ is independent of the parameter selection for b (i.e., if chord or span is used to nondimensionalize displacement). These normalization qualities are shared with $\mathcal{S}_F$, but singularities are avoided. A drawback of $\mathcal{S}_T$ is a reduction in the weight of terms with responses smaller than the maximum respective displacement or rotation. Like $\mathcal{S}_F$, $\mathcal{S}_T$ requires $\{\varphi^{\mathrm{t}}\}$ and $\{\varphi^{\mathrm{s}}\}$ to be provided with consistent scaled magnitudes.

2.2.3 Vibration Eigenpair Optimization

For both the target and design models, the vibration eigenpair problem is solved from

$$[\bar{\mathbf{K}}-\bar{\omega}^2\bar{\mathbf{M}}]\{\bar{\phi}\}=\{0\}, \tag{2.27}$$

where $\bar{\omega}^2$ are eigenvalues and $\{\bar{\phi}\}$ are eigenvectors. The objective function contributions are

$$\sum_{i=1}^{N_v}\mathcal{S}_T\left(\check{\phi}_i^t,\hat{\phi}_i^s\right), \tag{2.28}$$

where N_v is the number of vibration eigenpairs used for the optimization. Modal masses are matched as a result of matching the magnitudes of the scaled mass normalized eigenvectors. Vibration frequencies are constrained directly

$$\bar{\omega}_i^t = \bar{\omega}_i^s, \quad i = 0, 1, 2, ..., N_v. \tag{2.29}$$

Vibration eigenpair matching is the typical approach for modern aeroelastic scaled model design. This is the first scaling work to explicitly call for modal mass matching through matching magnitudes of the mass normalized eigenvectors.

Truncation of higher frequency eigenpairs is rational for geometrically linear applications, but certain higher frequency stiffnesses (e.g., axial stiffness) may be important for geometrically nonlinear applications, especially if the problem is globally indeterminate. The following two sections propose complementary techniques intended to help capture the internal force-stiffness coupling effects.

2.2.4 Buckling Eigenpair Optimization

A buckling eigenpair matching approach was first proposed by Bond *et al.* [14] The classical buckling problem is included in the optimization analysis,

$$[\bar{\mathbf{K}} + p\bar{\mathbf{K}}_{\mathbf{D}}]\{\bar{\psi}\} = \{0\}, \tag{2.30}$$

where the nondimensional differential stiffness matrix $\bar{\mathbf{K}}_{\mathbf{D}}$ is a linear function of a reference load case. The differential stiffness can be physically interpreted as a linear approximation of the internal load-stiffness coupling effects due to the higher-order terms of the strain-displacement relationship. The generalized eigenpair problem is solved for buckling eigenvalues p and eigenvectors $\{\bar{\psi}\}$. The first positive buckling eigenvalue can be used as an estimation of the structural stability for the reference load case.

The eigenpair analysis can be applied to design the stiffness such that dominant internal load-stiffness coupling effects match the target response. Target aeroelastic loads are used as the reference load case. The objective function contributions are

$$\sum_{j=1}^{N_b} \mathcal{S}_T\left(\check{\psi}_j^t, \hat{\psi}_j^s\right), \tag{2.31}$$

where N_b is the number of buckling eigenpairs used for the optimization. The buckling eigenvalues are optimized to match using equality constraints

$$p_j^t = p_j^s, \quad j = 0, 1, 2, ..., N_b. \tag{2.32}$$

Due to software issues, Bond *et al.* [14] were unable to include buckling eigenvector matching simultaneously with Eqs. 2.28 and 2.29 from the vibration analysis, which are required for scaling. Bond *et al.* [14] were, however, able to simultaneously include one buckling eigenvalue constraint with Eqs. 2.28 and 2.29 for a joined-wing scaling demonstration problem. Results had room for improvement in the agreement of the nonlinear static response. Software issues were resolved for this work, so that the proposed method can include an arbitrary number of buckling eigenpairs in the optimization analysis while simultaneously optimizing an arbitrary number of vibration eigenpairs . Additional eigenvalues and eigenvectors should help improve the matching of the nonlinear response when compared to results from Bond *et al.* [14]. Added incentive to revisit the method is provided by evidence of a subtle global geometric inconsistency (joint location) between the target and full scale demonstration models used by Bond *et al.* [14]. Though the inconsistency is not conclusively verified, it would have negatively impacted the quality of the results.

2.2.5 Static Deformation Mode Optimization

Another option is optimization of the static response to a design significant reference load. Evaluating the nonlinear static equation of equilibrium,

$$[\bar{\mathbf{K}}_{\mathbf{NL}}(\mathrm{x})]\{\bar{\mathrm{x}}\} = \frac{1}{2}\frac{\mu_1}{\kappa_1^2}\{\bar{\mathrm{F}}\}, \tag{2.33}$$

the static response $\{\bar{\mathrm{x}}\}$ can be designed to match the target. Multiple load cases or reference load magnitudes can be considered. An equivalent static loads approach, described in detail in the following section, is used for the nonlinear static response optimization. Optimization of the nonlinear static response should directly require the global internal force-stiffness coupling effects to be consistent between the target and scaled models for the reference case.

Static response optimization that ignores geometric nonlinearity is included by considering the linear elastic equation of equilibrium

$$[\bar{\mathbf{K}}(\mathrm{x})]\{\bar{\mathrm{x}}\} = \frac{1}{2}\frac{\mu_1}{\kappa_1^2}\{\bar{\mathrm{F}}\}. \tag{2.34}$$

The linear response can be used hone the flexibility properties of the scaled model at specific design points (e.g., trim). The optimization does not directly capture internal force-stiffness coupling. For static deformation mode optimization, the objective function contributions are

$$\sum_{lc=1}^{N_{lc}} \mathcal{S}_T\left(\bar{x}_{lc}^t, \bar{x}_{lc}^s\right), \tag{2.35}$$

where N_{lc} is the number of load cases.

2.2.6 Equivalent Static Loads

Direct optimization of the nonlinear static response is a computationally intensive task. Efficiency can be gained by transformation to an equivalent linear system using the equivalent static loads (ESL) approach [43]. The current or initial design $\{\mathrm{d}\}$ and loading conditions $\{\mathrm{F}\}$ are specified. Nonlinear analysis provides the nonlinear static deformations $\{\mathrm{x}_{\mathrm{NL}}\}$ by solving the nonlinear equation of equilibrium

$$[\mathbf{K_{NL}}](\mathrm{d}, \mathrm{x}_{\mathrm{NL}})\{\mathrm{x}_{\mathrm{NL}}\} = \{\mathrm{F}\}. \tag{2.36}$$

The load set that will result in equivalent linear static displacements and rotations $\{\mathrm{F}_{\mathrm{Eq}}\}$ is determined by multiplying the nonlinear deformations by the linear stiffness matrix $[\mathbf{K}_{\mathrm{Lin}}]$

$$\{\mathrm{F}_{\mathrm{Eq}}\} = [\mathbf{K}_{\mathrm{Lin}}(\mathrm{d})]\{\mathrm{x}_{\mathrm{NL}}\}. \tag{2.37}$$

Efficient gradient-based optimization can be performed on the equivalent linearized system

$$[\mathbf{K}_{\mathrm{Lin}}(\mathrm{d})]\{\mathrm{x}_{\mathrm{Lin}}\} = \{\mathrm{F}_{\mathrm{Eq}}\}. \tag{2.38}$$

The ESL approach requires an iterative procedure that updates the linearized system as the design changes. The optimization converges when the linearized optimum response matches the response of the nonlinear system. The ESL methodology was originally developed and applied to the joined-wing application by Lee *et al.* [43]. Kim *et al.* [40] showed that ESL optimization produced a better design than a fully stressed design methodology for a detailed joined-wing case. Kim *et al.* [41] later showed that the ESL methodology produced the same joined-wing design as a conventional gradient-based optimization, but at a much lower cost. Green *et al.* [33] optimized a joined-wing structure modeled with geometrically exact beam theory. The ESL approach was compared to direct gradient-based optimization for the nonlinear problem. The authors found that the ESL approach reduced computational expenses by three orders of magnitude.

Previous work in ESL optimization has not considered modal frequency constraints. Modal frequency constraints are required for the proposed scaling method. The implemented procedure is shown in Fig. (2.1).

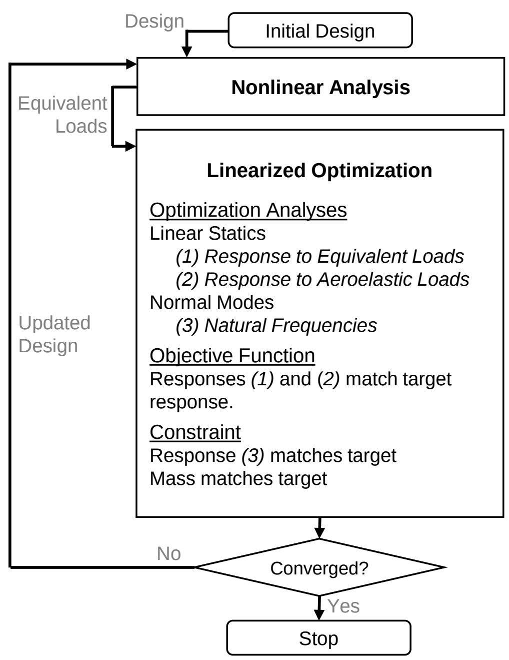

Figure 2.1: ESL optimization procedure.

MSC Nastran supports ESL optimization as a prerelease feature, but simultaneous linear static and normal modes analysis is not directly supported [3]. The procedure was realized by wrapping MSC Nastran's nonlinear static analysis and optimization analysis using MATLAB. Parameters were specified to request printed equivalent static loads after each nonlinear analysis. The equivalent loads are used in the optimization. Exchange of the updated design and updated loads is managed by the custom wrapper.

2.2.7 Systematic Optimization Approach

A systematic approach to investigating incremental extensions of the proposed methods will be tested by combining weighted objective functions

$$\sum_{i=1}^{N_v} \mathcal{S}_T\left(\check{\phi}_i^t, \hat{\phi}_i^s\right) + \sum_{j=1}^{N_b} \mathcal{S}_T\left(\check{\psi}_j^t, \hat{\psi}_j^s\right) + \sum_{lc=1}^{N_{lc}} \mathcal{S}_T\left(\bar{x}_{lc}^t, \bar{x}_{lc}^s\right) \tag{2.39}$$

and constraints

$$\bar{\omega}_i^t = \bar{\omega}_i^s, \quad i = 0, 1, 2, ..., N_v, \tag{2.40}$$

$$p_j^t = p_j^s, \quad j = 0, 1, 2, ..., N_b, \tag{2.41}$$

from the proposed scaling techniques, by which the utility of extending existing methods is quantified. The approach is tested for incremental values of N_v, N_b, and N_{lc}.

2.2.8 Optimization Algorithm

Constrained optimization

The basic optimization problem considered for this work is minimization of a function subject to equality and inequality constraints

$$\begin{aligned} \textbf{minimize} \quad & f(\mathrm{d}) \\ \textbf{such that} \quad & h_i(\mathrm{d}) = 0, \quad i = 1, ..., n_h, \\ & g_j(\mathrm{d}) \leq 0, \quad j = 1, ..., n_g, \end{aligned} \tag{2.42}$$

where f is the objective function, d is a vector of design variables, n_h is the number of equality constraints, the h_i are the equality constraint functions, n_g is the number of inequality constraints, and the g_j are the inequality constraint functions. For this work, (2.42) is optimized with the sequential quadratic programming (SQP) method [68] using an implementation by by Spillman and Canfield [70]. Selected convergence settings for SQP ensure that converged solutions satisfy the Karush-Kuhn-Tucker [42] conditions within a tight tolerance. One issue is the possibility of several local minima. For this work, a search for the global minimum is conducted. First, multiple SQP optimizations are executed using random initial designs. Information from the database of designs is used to inform a global search optimization using the DIRECT algorithm. DIRECT requires transformation of (2.42) to a bound problem with constraint penalty functions. The transformation and global search optimization is explained in the next section.

Unconstrained global optimization

A valuable property of descent functions is that an unconstrained local optimum point must be a local optimum point of the original constrained problem [5]. The descent function

$$\mathcal{D}_{\mathcal{F}} = f(\mathrm{d}) + \sum_{e=1}^{n_h} r_e|h_e| + \sum_{i=1}^{n_g} \mu_i \max\{0, g_i\} \tag{2.43}$$

proposed by Han [34] and Powell [57] is used for this work, where the $r_e > 0$ are the penalty parameters for equality constraints and the $\mu_i > 0$ are the penalty parameters for inequality constraints. The descent function requires that the penalty parameters for the constraints must be greater than or equal to the respective Lagrange multipliers from the optimum of the original constrained problem. For this work, informed values for the penalty parameters are taken as five times the largest Lagrange multiplier from the best of the database of SQP solutions. Then (2.43) is minimized with the DIRECT algorithm using an implementation by Finkel [26]. The best solution from the database of SQP solutions is set as the center of the design space for the global search. This ensures that DIRECT starts with a feasible design. If the best design from DIRECT outperforms the initial design, or DIRECT finds feasible designs sufficiently far from designs in the existing SQP database, those designs are explored as initial designs with SQP.

2.3 Aerodynamic Trim Analysis

The flow field of a steady, inviscid, incompressible, and irrotational fluid is governed by Laplace's equation

$$\nabla^2 \phi = 0. \tag{2.44}$$

The linear equation (2.44) can be satisfied by superposition of any number of solutions. These can include elementary solutions such as points sources and sinks, doublets, and vortex filaments. The vortex lattice method uses an arbitrary number, say N, vortex filaments and enforces particular boundary conditions at N control points. Consider the vortex filament shown in Fig. 2.2.

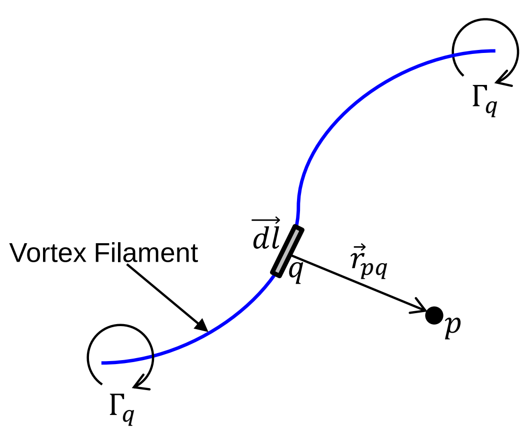

Figure 2.2: Three-dimensional vortex filament.

The flow induced by a vortex filament is given by the Biot-Savart law [48]

$$d\overrightarrow{V}_p = \frac{\Gamma_q}{4\pi}\frac{\overrightarrow{dl} \times \overrightarrow{r}_{pq}}{|\overrightarrow{r}_{pq}|^3}, \tag{2.45}$$

where $\overrightarrow{V}_p$ is induced velocity at point p, Γ_q is the vortex strength, which is constant across any filament, $\overrightarrow{dl}$ is an infinitesimal element taken along the vortex filament curve, $\overrightarrow{r}_{pq}$ is a vector from $\overrightarrow{dl}$ to an arbitrary point p. Equation (2.45) can be integrated over the length of the filament to obtain the velocity the filament induces at point p

$$\overrightarrow{V}_p = \frac{\Gamma_q}{4\pi}\int \frac{\overrightarrow{dl} \times \overrightarrow{r}_{pq}}{|\overrightarrow{r}_{pq}|^3}. \tag{2.46}$$

An arrangement of vortex filaments and control points are used to approximate the aircraft lifting surfaces. The mean camber surface is discretized into a lattice of quadrilateral panels with a horseshoe vortex filament placed on each panel. See Fig. 2.3 for an illustration. Each horseshoe vortex filament is made up of bound and trailing vortices. The bound vortices are located at the quarter panel location of each panel. Trailing vortices extend aft of each bound vortex and follow the camber surface until they reach the trailing edge. Aft of the trailing edge, the trailing vortices extend to infinity in the aircraft x direction. Boundary control points are placed on the 3/4 panel point of each panel. Force control points are placed on the 1/4 panel point of each panel.

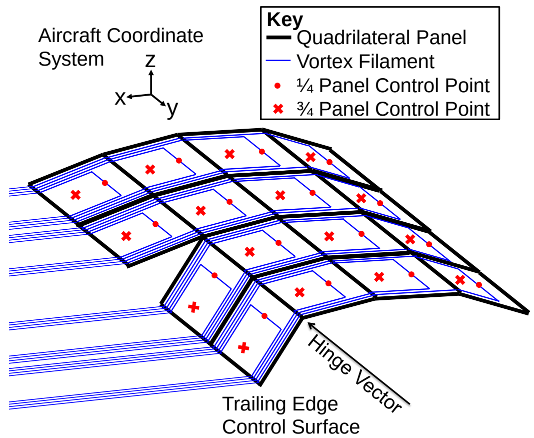

Figure 2.3: Example discretized camber surface with trailing edge control surface.

The highest computational expense of the vortex lattice analysis is the calculation of induced velocity and induced influence coefficients. The induced velocity coefficient array, $[[\overrightarrow{V}_{pq}]]$,is an $N \times N \times 3$ array that is calculated to give the vortex strength normalized induced velocity at each *force* control point from each horseshoe vortex filament,

$$\overrightarrow{V}_{pq} = \frac{\overrightarrow{V}_p}{\Gamma_q} = \frac{1}{4\pi} \int \frac{\overrightarrow{dl} \times \overrightarrow{r}_{pq}}{|\overrightarrow{r}_{pq}|^3} \qquad p, q = 1, 2, ..., N. \tag{2.47}$$

The induced influence coefficient matrix, $[w_{pq}]$, is an $N \times N$ matrix that is calculated to give the vortex strength normalized induced velocity through each panel's *boundary* control point from each horseshoe vortex filament,

$$w_{pq} = \hat{n}_p \cdot \left(\frac{1}{4\pi} \int \frac{\overrightarrow{dl} \times \overrightarrow{r}_{pq}}{|\overrightarrow{r}_{pq}|^3} \right) \qquad p, q = 1, 2, ..., N, \tag{2.48}$$

where $\hat{n}_p$ is a unit vector normal to panel p.

The freestream flow normal to each panel depends on the aircraft geometry and orientation relative to the freestream velocity vector,

$$b_p = \overrightarrow{V}_\infty \cdot \hat{n}_p \qquad p = 1, 2, ..., N \quad , \tag{2.49}$$

where b_p is the magnitude of the freestream flow through each panel and $\overrightarrow{V}_\infty$ is the freestream velocity vector. This information is used to solve for the combination of vortex strengths that exactly satisfy the no penetration boundary condition at the boundary control points. The vortex induced velocity through each panel must cancel the freestream velocity through each panel

$$[w_{pq}]\{\Gamma_q\} = \{b_p\}. \tag{2.50}$$

Solving for Γ_q,

$$\{\Gamma_q\} = [w_{pq}]^{-1}\{b_p\}. \tag{2.51}$$

The vortex strengths are then used to solve for the force at each force control point $\overrightarrow{F}_p$ using the Kutta–Joukowski theorem,

$$\overrightarrow{F}_p = \sum_{q=1}^{N} \rho(\overrightarrow{V}_{pq} \times \Gamma_p) l_{\Gamma_p} \qquad p = 1, 2, ..., N \quad , \tag{2.52}$$

where l_{Γ_p} is the length of the bound vortex on panel p. The forces are then post-processed as needed.

Two vortex lattice codes are freely and publicly available. Both were considered for use in the aeroelastic coupling scheme. Athena Vortex Lattice (AVL) was developed by Drela and Youngren [21]. AVL is a Fortran executable with text based input and output. AVL is computationally efficient, and it uses geometric inputs that are conducive to aeroelastic coupling. However, it does not provide aerodynamic force outputs in vector form. The force output that is provided could not easily be resolved to a form that is usable for aeroelastic problems. Tornado is a vortex lattice code developed by Melin [49]. Tornado provides the essential vector force output. Because the program is Matlab based, it is easy to wrap in a Matlab based aeroelastic coupling interface. Unfortunately, the geometry inputs are based on aircraft design parameters. Defining deformed paneling that is geometrically consistent with the deformed structure, which is essential for an aeroelastic coupling scheme, is not achievable without extensive modification of the code. Other downsides are the code is computationally inefficient, and lacks a trim solver.

While it is possible to modify these publicly available codes to better suit the needs of an aeroelastic coupling scheme, it was decided that an independent vortex lattice code would offer the best solution. A new vortex lattice code for aeroelasticity (VoLAre) was developed based on the formulation presented in this section. The code is designed to take an arbitrary number camber line pairs as geometric input. The lattice is generated automatically from the camber line pairs. The camber lines can be parameterized by a control surface deflection variable. The trim routine determines the required aircraft angle of attack and control surface deflection to achieve a user defined lift coefficient while canceling any pitching moment.

VoLAre is verified against an example in Bertin [9], and AVL trim results. The code is validated against experimental results by Weber and Brebner [76]. Verification and validation results are provided in the Results chapter.

2.4 Nonlinear Aeroelastic Trim Solution

Nonlinear static aeroelastic trim analysis for high fidelity built-up structures is a capability that is unavailable in any commercial software or released research code. Such a capability was developed by the authors in Ref. [63]. A custom developed vortex lattice code was loosely coupled with MSC Nastran's nonlinear structural analysis. This capability has been improved since the previous publication by implementing an infinite plate spline (IPS) module for load and displacement transfer. The IPS method was originally developed by Harder and Desmarais [35]. Ref. [2] provides a valuable implementation description. The new analysis configuration considerably reduces the user input requirements compared to the analysis as presented in Ref. [63]. The user creates an MSC Nastran finite element model and an aerodynamic panel model in the in-house format. Spline sets are defined by providing sets of spline nodes/panels and spline coordinate systems.

The trim routine is outlined in Fig. 2.4. The vortex lattice code solves for the angle of attack and control surface deflection needed for longitudinal equilibrium of the initial or deformed aerodynamic panel model. Aerodynamic loads are passed to the spline module. The spline module interpolates strain energy equivalent loads for the structural analysis. The gravity vector, which includes appropriate inertial relief, is rotated so that it is consistent with the aircraft rotation at trim. MSC Nastran solves for the nonlinear static structural response. Displacements are passed to the spline module, which provides a deformed aerodynamic panel model to the vortex lattice analysis. The sequence is iterated until convergence. Convergence is checked by tracking the relative changes of structural node positions, aerodynamic panel corner positions, and aerodynamic loads. Convergence is reached when relative changes are less than specified tolerances. The aeroelastic analysis was verified by selecting options for linear structural analysis and comparing to linear trim results from MSC Nastran. For geometrically nonlinear aeroelastic trim analysis, options for nonlinear structural analysis are specified in the structural solver inputs. The coupling interface functions identically.

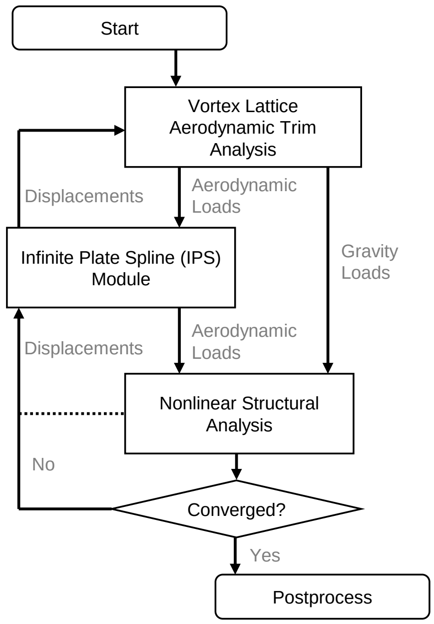

Figure 2.4: Nonlinear static aeroelastic trim routine.

2.5 Linearized Dynamic Aeroelastic Analysis

For additional scaled model verification, the dynamic aeroelastic response of the optimized scaled model was compared to the target model. The models were linearized about a converged $1g$ nonlinear aeroelastic trim state. Aeroelastic frequency and damping responses were calculated using a ZONA6 solution in ZAERO. The solution uses g-method with doublet lattice aerodynamics [1]. Sea level density and zero Mach number were assumed. Aerodynamic paneling was similar to paneling in Fig. 2.9. Infinite plate splines were used for information transfer.

2.6 Structural Analysis and Sensitivities

All structural analyses for the target aircraft (see Fig. 2.7) and nonlinear structural analyses for the designed scaled aircraft (see Fig. 2.8) were performed using MSC Nastran. MSC Nastran is a general purpose finite element program with built in optimization tools [50]. The author found it was prohibitively difficult to get MSC Nastran working correctly for cases in the proposed systematic optimization approach described in the Scaling Optimization section. A NASTRAN compatible frame finite element (CoFFe) analysis code was written to circumvent the limitations of the commercial analysis. The program is structured as shown in Fig. 2.5. The mesh, properties, loads, and constraints are defined using the text-based NASTRAN free field bulk data format.

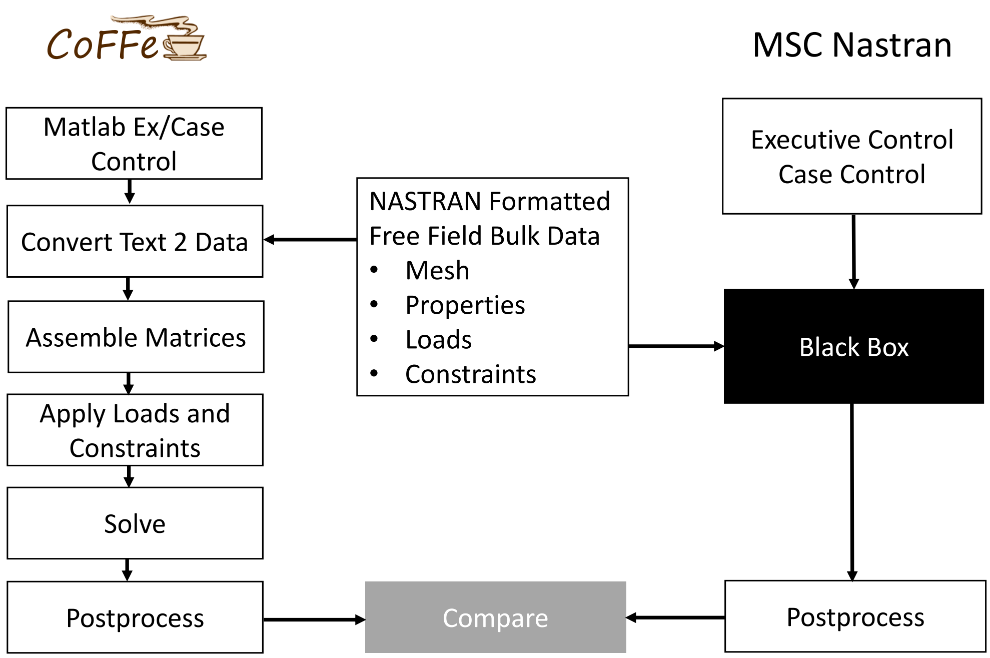

Figure 2.5: Program structure and verification with MSC Nastran.

The model format allows for seamless verification with MSC Nastran, which can process the same input file. Table 2.1 lists supported entries. Not all of the MSC Nastran options

Table 2.1: Supported NASTRAN compatible bulk data entries.

Mesh	**Properties**	**Loads**	**Constraints**
GRID	PBEAM	FORCE	SPC1
CBEAM	PBEAML	MOMENT	RBE2
CELAS2	PMASS	GRAV	RBE3
CMASS1	MAT1		
CORD2R	PROD		
CROD			

for the tabulated entries are supported in CoFFe. An appended user manual has details for each entry. CoFFe was used for analysis and semi-analytic design sensitivities for linear statics, vibration eigenpair, and buckling eigenpair problems. Methods developed by Lee and Jung are used for calculating system matrix normalized eigenvector sensitivities for problems with distinct [45] and repeated [44] eigenvalues. In addition to circumventing the functional limitations of commercial analysis, CoFFe runs considerably faster than MSC Nastran for the specific problems of interest. CoFFe also made parallelization possible on supercomputers that don't have MSC Nastran license access.

2.7 Parallel Cluster Computing

Advanced Research Computing (ARC) at Virginia Tech[1] provides the university computing resources to advance computational research. ARC maintains the Athena cluster system, which was accessed for this work. Athena runs CentOS Linux 5 with 42 quad-socket, AMD 2.3GHz Magny Cour octa-core nodes (1,344 cores) with 64 GB RAM each (12.4 TFLOP peak). A single user can access 128 to 256 cores at time.

For this work, a custom framework was developed for coarsely parallel cluster computing. The process is illustrated in Fig. 2.6. The user logs into Athena using an SSH client,

[1] http://www.arc.vt.edu/

necessary files are transferred, then the user submits a tasking job to the queue. The tasking job submits as many autonomous optimization wrappers as possible to the queue. The autonomous wrappers access a list of optimization cases that are needed. A file containing the active case number is incremented as the cases are completed. Optimization output files are stored on Athena drives and transferred once all cases are complete.

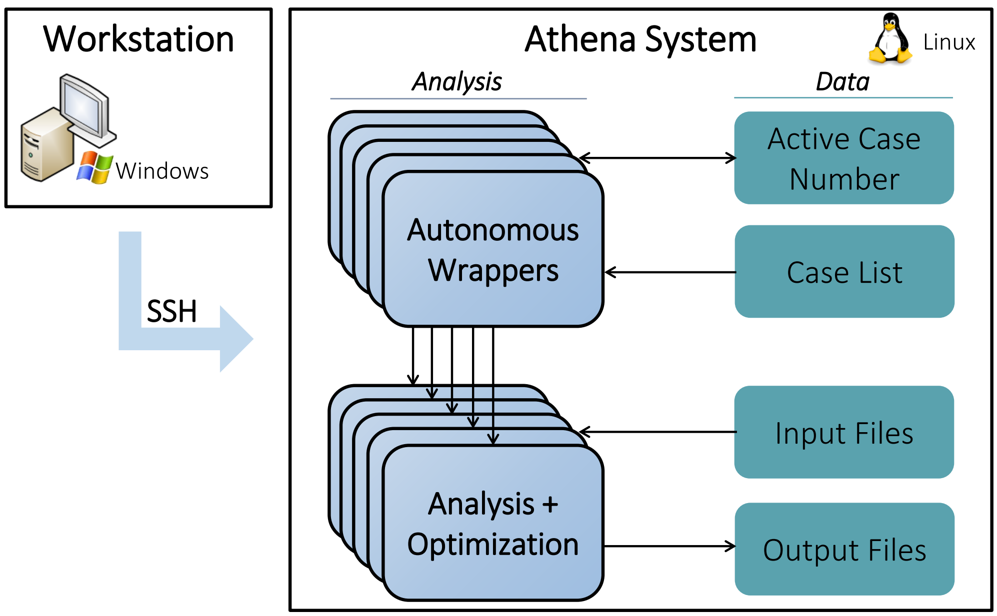

Figure 2.6: Parallel cluster computing framework.

2.8 Models

A target full-scale model, inspired by the Blair *et al.* [13] model presented in Chapter 1, is shown in Fig. 2.7. The model has a 75 ft wing span. The forward and aft wings are swept 36° and have dihedral of 7° and -14°, respectively. The forward and aft wing aerodynamic chords are 11.46 ft and 2.91 ft, respectively. The structure is modeled as aluminum wingboxes with constant cross-sectional dimensions. An example wing section is illustrated in Fig. 2.10. Section dimensions are provided in Table A.4. The wing joint is modeled by connecting the adjacent forward and aft wing ribs with rigid elements. Results consider the model operating at 100,000 lb and flying 400 ft/s at sea level. Weight breakdown is provided in the results section.

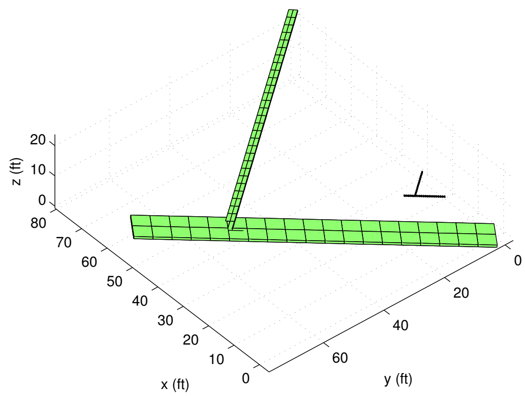

Figure 2.7: Target full-scale finite element model with scaled model.

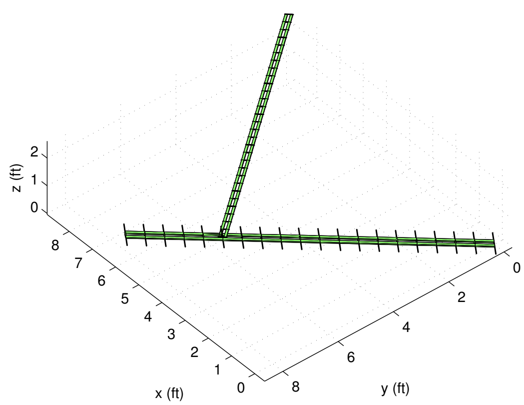

Figure 2.8: Scaled model ladder structure.

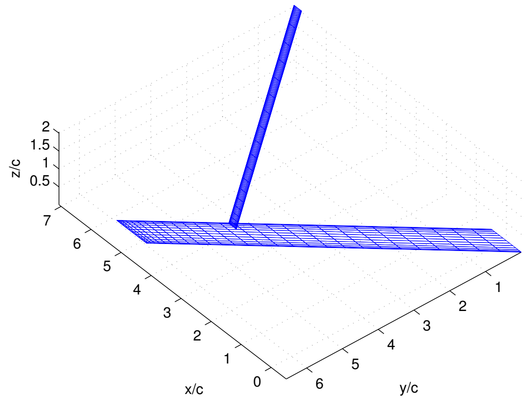

Figure 2.9: Chord normalized aerodynamic paneling.

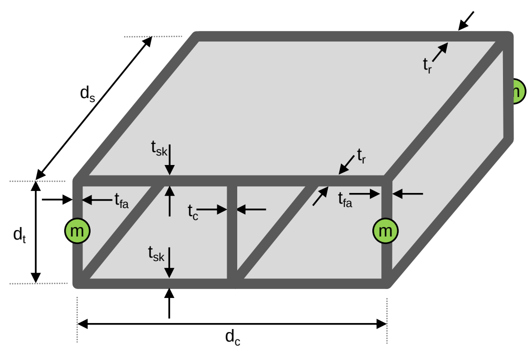

Figure 2.10: Full-scale target model wingbox section. Dimensions provided in Table A.4.

For size comparison, the 1/9$^{\text{th}}$ scaled model is shown alongside the full-scale aircraft in Fig. 2.7. Due to material and manufacturing constraints, the scaled model cannot be manufactured with the same box beam structural layout. Bisplinghoff *et al.* [12] recommend a ladder structure, among other options, as an alternative configuration for aeroelastically scaled models. The rectangular spars and cylindrical rungs can be tailored to match the required stiffness. Modern foam materials allow the construction technique illustrated in Fig. 2.11. Aerodynamic shape is maintained by polyethylene foam, commonly used to make swimming pool noodles. The rough outer surface would be smoothed by applying spackling paste. Balsa ribs and leading and trailing edge strips would provide local support, but overall the polyethylene and balsa would provide negligible global stiffness. Designable lead masses allow inertia matching. The assembled ladder structure is shown if Fig. 2.8. Only the aluminum stiffness is modeled; nonstructural mass accounts for the remaining materials. Beam elements are most appropriate to model the ladder structure. Nonstructural mass is modeled as discrete masses at the leading edge, center, and trailing edge of each rib section. Rigid elements are used to interpolate loads and displacements at the leading and trailing edges. This allows for accurate spline data transfer.

The scaled and full-scale models share the aerodynamic paneling shown in Fig. 2.9. The wings have no camber and are untwisted in their undeformed state. Pitch trim control is provided by elevator control surfaces on the four most inboard panel sections of the aft wing. The elevator hinge line is at 81% chord.

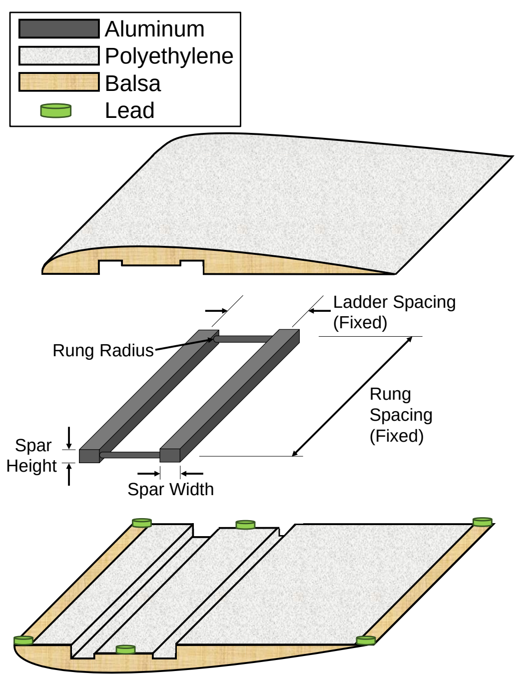

Figure 2.11: Scaled model wing section concept.

The following ten items are design variables:

1. width of forward wing spars,

2. height of forward wing spars,
3. radius of forward wing rungs,
4. discrete mass at leading and trailing edge of each forward wing rib,
5. discrete mass at midsection of each forward wing rib,
6. width of aft wing spars,
7. height of aft wing spars,
8. radius of aft wing rungs,
9. discrete mass at leading and trailing edge of each aft wing rib,
10. discrete mass at midsection of each aft wing rib.

This chapter introduced methods for analysis and optimization of aeroelastically-scaled vehicles. Verification of the methods and results for the joined-wing demonstration problem are presented in the next chapter.

Chapter 3

Results

3.1 Analysis Verification

3.1.1 Vortex Lattice Aerodynamic Analysis

Weber and Brebner Planform

Weber and Brebner [76] published low-speed pressure measurements for the tailless configuration of the planforms shown in Fig. 3.1. Bertin [9] published vortex lattice results for the coarse mesh. Various results from three similar meshes where generated with Athena Vortex Lattice (AVL) [21]. These results are used to verify and validate VoLAre.

Results from an angle of attack sweep are shown in Figs. 3.2 and 3.3. Lift coefficient results all agree closely at small angles of attack. The experimental results have a slightly shallower lift curve slope slope and concave down curvature due to nonlinear viscous effects at high angles of attack. Mesh differences could account for some of the slope disagreement between the AVL and VoLAre fine mesh results. Lift induced drag results agree closely between AVL and VoLAre. Weber and Brebner measured total drag, which does not allow for direct comparison, but does allow an order of magnitude check.

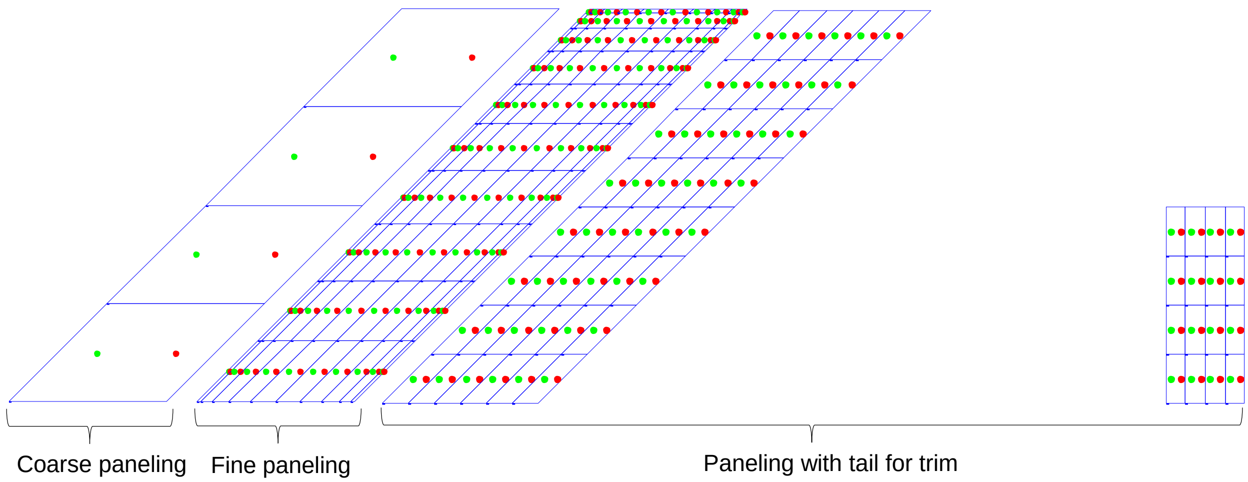

Figure 3.1: Discretized variations of Weber & Brebner planform.

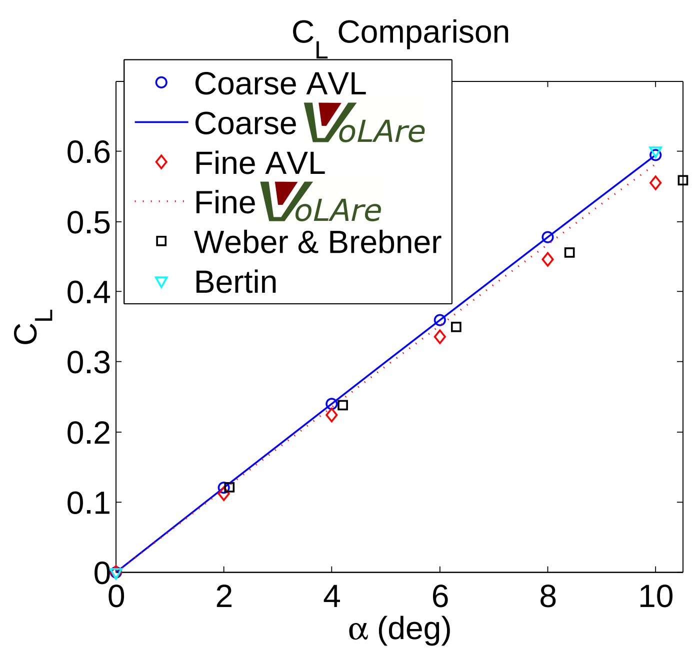

Figure 3.2: C_L results comparison.

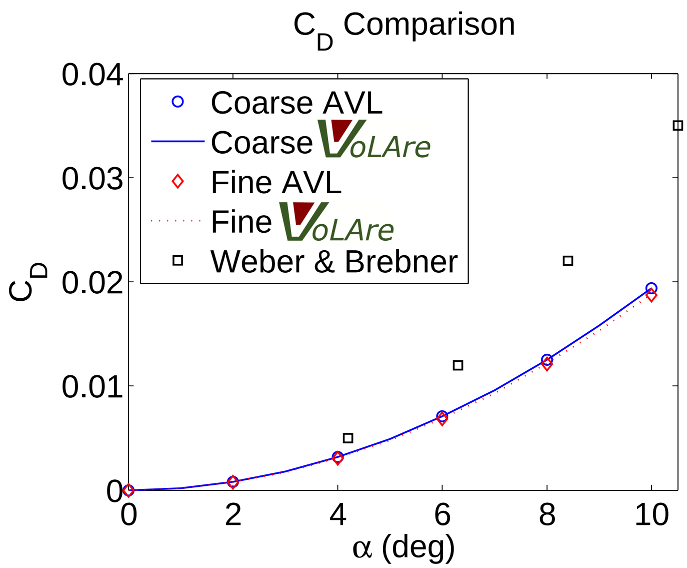

Figure 3.3: C_D results comparison.

The planform with a tail in Fig. 3.1 was trimmed in AVL and VoLAre over a range of lift coefficients. Results for trim angle of attack, α, and trim elevator deflection, δ, are shown in Fig. 3.4. The elevator hinge line is at the tail midchord. The trimmed induced drag polars are compared in Fig. 3.5; the induced drag coefficients are in close agreement.

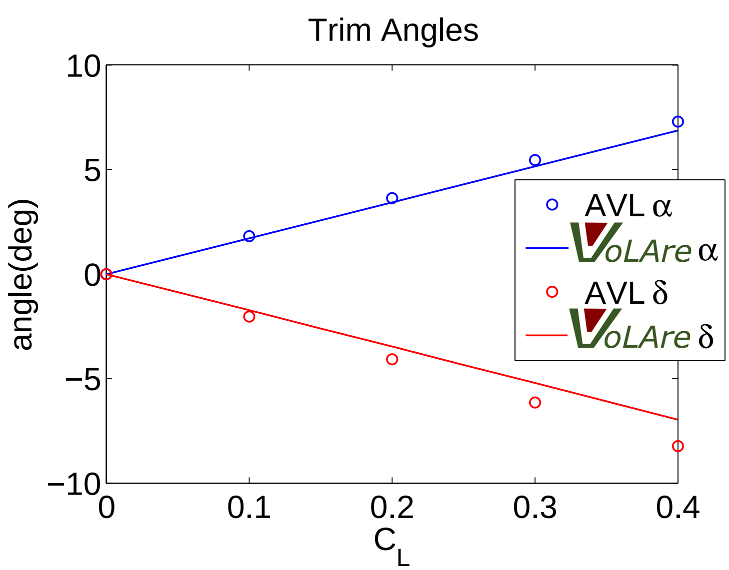

Figure 3.4: Trim angle results comparison.

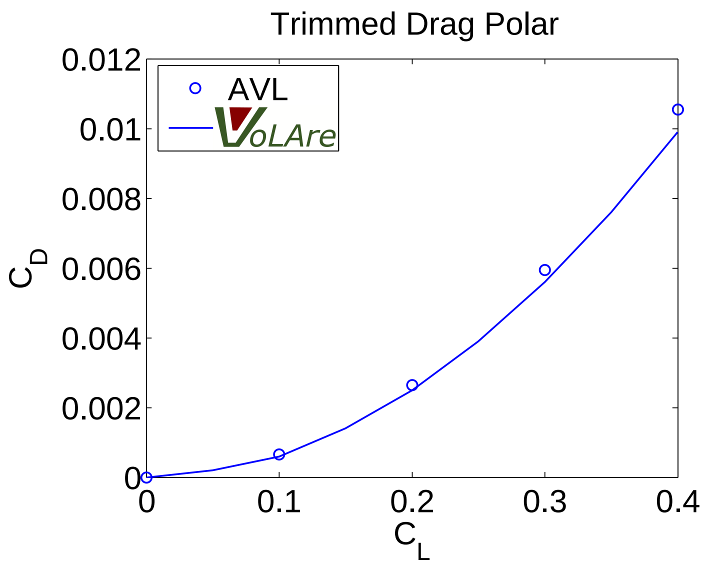

Figure 3.5: Trimmed drag polar results comparison.

The Weber and Brebner planform results compared to AVL verify that VoLAre lift, drag, and trim solutions are working as intended. Comparison to the experimental results validates that the vortex lattice lift solution is accurate at small angles of attack. The vortex lattice method only approximates the lift induced component of the total drag. Accurate total drag calculations are important for assessing the vehicle performance and sizing the propulsion system, but, in most cases, the aeroelastic response of the vehicle is dominated by distributed lift forces. Non-lift-induced drag is neglected in this work.

Complex SensorCraft Configuration

The robustness of VoLAre is verified by studying results from a more complicated configuration with variable camber, taper, and twist. Figure 3.6 shows the VoLAre discretized mean camber surface of the joined-wing concept. Results are compared to results from a similar AVL model that was developed from discretizing the same mean camber surface, and NASA Ames wind tunnel results preformed by Boeing and presented by Ref. [65]. Lift coefficient results from an angle of attack sweep are shown in Fig. 3.7. Lift curve slopes are in close agreement. There is a slight difference in zero slope angles attack; the difference may be partially due to small differences in the reference coordinate systems.

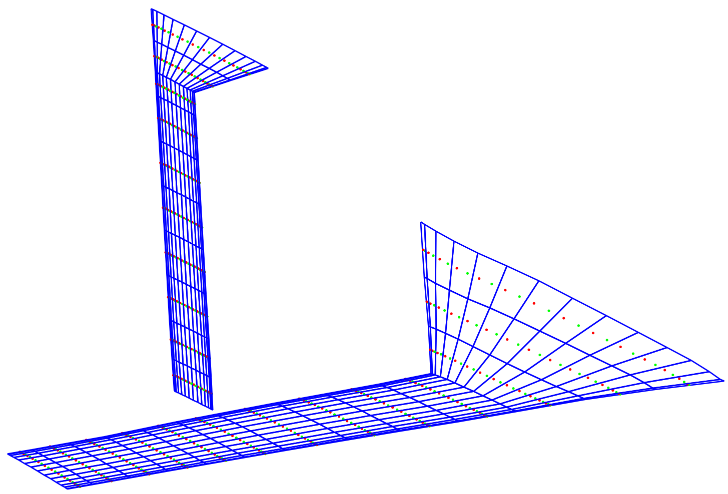

Figure 3.6: Scaled SensorCraft detailed aerodynamic paneling.

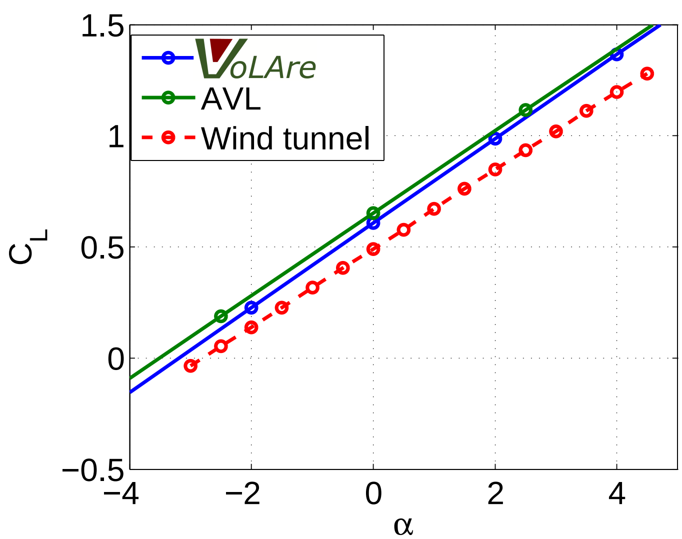

Figure 3.7: C_L results comparison.

Drag coefficients from the angle of attack sweep are shown in Fig. 3.8. The results have similar concave up behavior from induced drag. Wind tunnel results include non-lift-induced drag that is not captured with the vortex lattice method. Results from the SensorCraft configuration show that VoLAre works as intended, even for models with complex geometry.

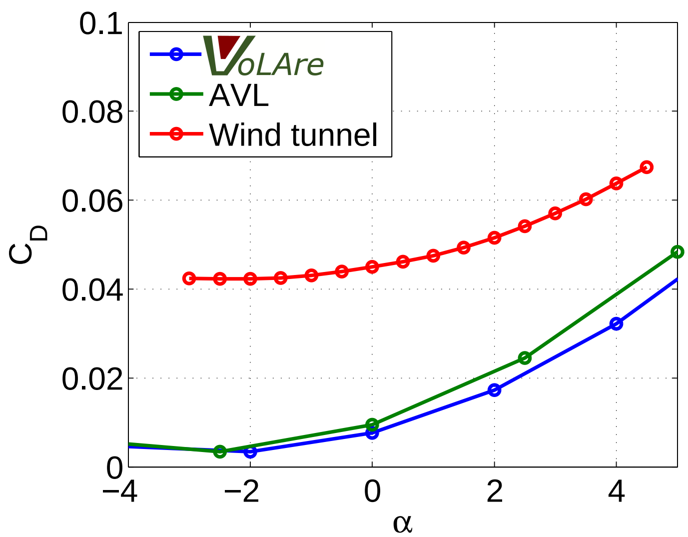

Figure 3.8: C_D results comparison.

3.1.2 NASTRAN Compatible Frame Finite Element Structural Analysis

The NASTRAN compatible frame finite element structural analysis (CoFFe) was verified by directly comparing output to results from MSC Nastran. The process was seamless because both codes use compatible text input to define the model. Structural models for two joined-wing concepts were used in the verification. The first was the scaled joined-wing concept described in the methodology chapter. The second is a flexible mini SensorCraft concept developed for a flight test program. Linear static response to applied aeroelastic-type loads are shown Fig. 3.9. MSC Nastran and CoFFe agree closely.

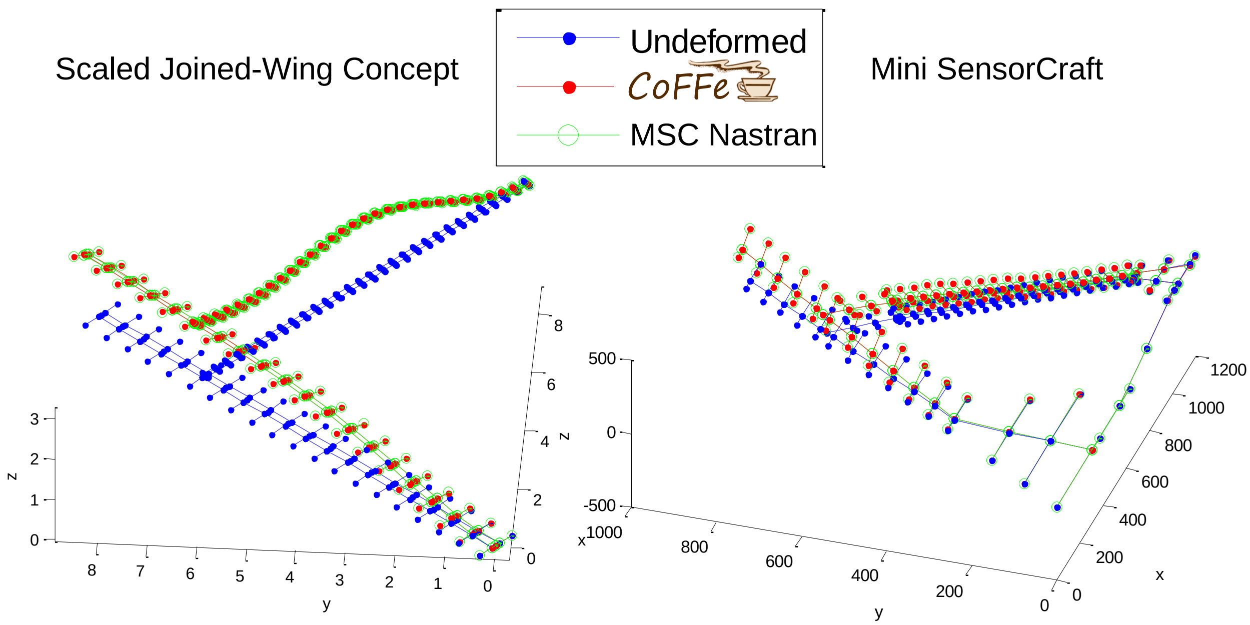

Figure 3.9: Linear static verification results.

Vibration mode shapes also agree; one vibration eigenvector mode shape is shown for both models in Fig. 3.10. Vibration frequencies are compared in Tables 3.1 and 3.2. Tabulated scaled joined-wing concept and mini SensorCraft vibration frequencies match MSC Nastran within 0.3% and 1.5%, respectively.

Table 3.1: Vibration frequency comparison for scaled joined-wing concept.

Mode	CoFFe	MSC Nastran	%Difference
1	1.2128	1.2128	0.0014
2	1.2697	1.2688	0.0688
3	1.7388	1.7367	0.1213
4	2.5453	2.5380	0.2875
5	3.3369	3.3345	0.0726

Table 3.2: Natural frequency comparison for mini SensorCraft.

Mode	CoFFe	MSC Nastran	%Difference
1	5.0275	5.0204	0.1418
2	9.0357	9.0215	0.1572
3	18.4180	18.3182	0.5447
4	24.6440	24.2891	1.4609
5	34.7365	34.3597	1.0966

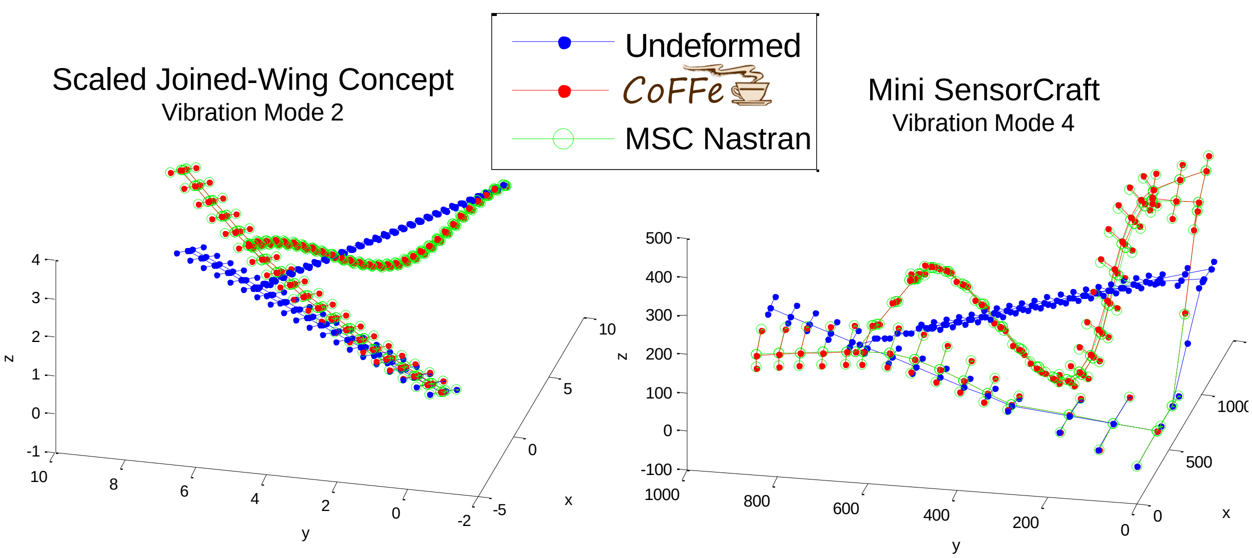

Figure 3.10: Free vibration verification results.

First buckling mode shapes for both models, shown in Fig. 3.11, were in agreement. Buckling eigenvalues are compared in Tables 3.3 and 3.4. Tabulated scaled joined-wing concept and mini SensorCraft buckling eigenvalues match MSC Nastran within 0.0719% and 0.1648%, respectively.

Table 3.3: Buckling eigenvalue comparison for scaled joined-wing concept.

Mode	CoFFe	MSC Nastran	%Difference
1	0.6775	0.6777	-0.0413
2	1.2145	1.2152	-0.0594
3	1.9872	1.9886	-0.0712
4	2.5763	2.5782	-0.0719
5	3.2693	3.2716	-0.0687

Table 3.4: Buckling eigenvalue comparison for mini SensorCraft.

Mode	CoFFe	MSC Nastran	%Difference
1	1.5547	1.5569	-0.1466
2	2.5055	2.5092	-0.1487
3	4.3544	4.3614	-0.1586
4	-4.6282	-4.6358	-0.1648
5	5.3368	5.3452	-0.1562

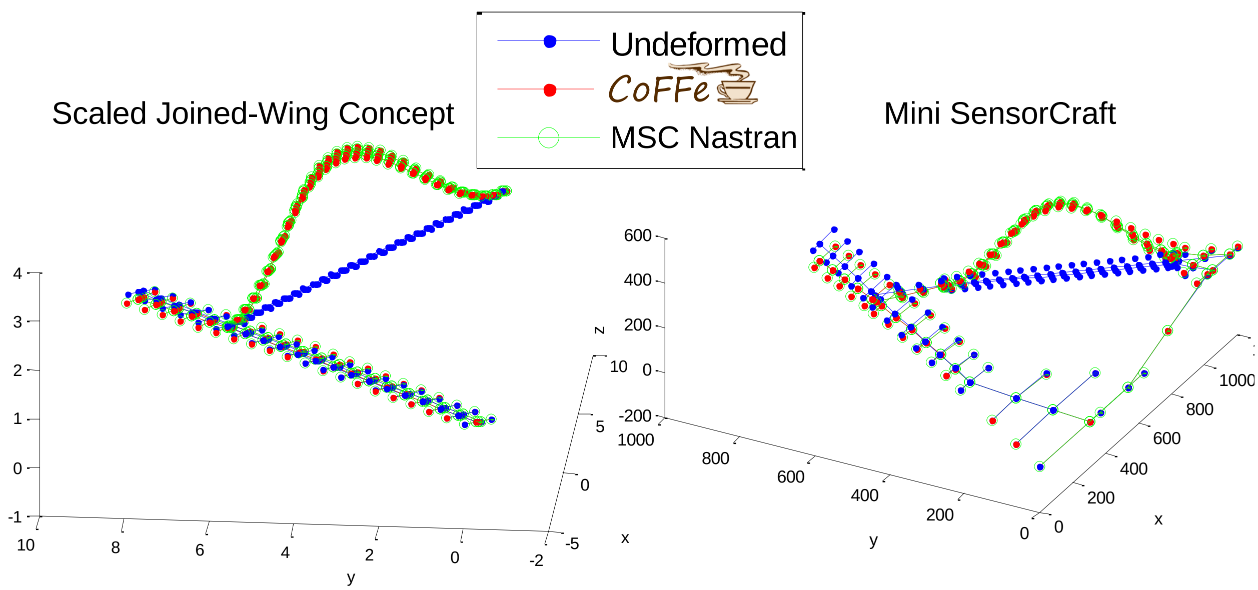

Figure 3.11: Buckling verification results.

Comparison of CoFFe results to results from MSC Nastran verified that CoFFe is working as intended for linear statics, vibration eigenpair, and buckling eigenpair analyses. CoFFe results were also compared to analytic results for a simple cantilever model. Results converged to the analytic solutions. Semi-analytic design sensitivities for were verified by comparison to finite difference and complex step.

3.1.3 Aeroelastic Analysis

The custom code coupling interface for aeroelastic trim analysis was verified by comparing to results from MSC Nastran. MSC Nastran is limited to linear structural analysis for aeroelastic trim. The custom code coupling interface does not have that limitation, but specifying options for linear structural analysis allows for a direct comparison to MSC Nastran. Aeroelastic models of a flexible HALE vehicle, shown if Figs. 3.12 and 3.13, were used for the verification.

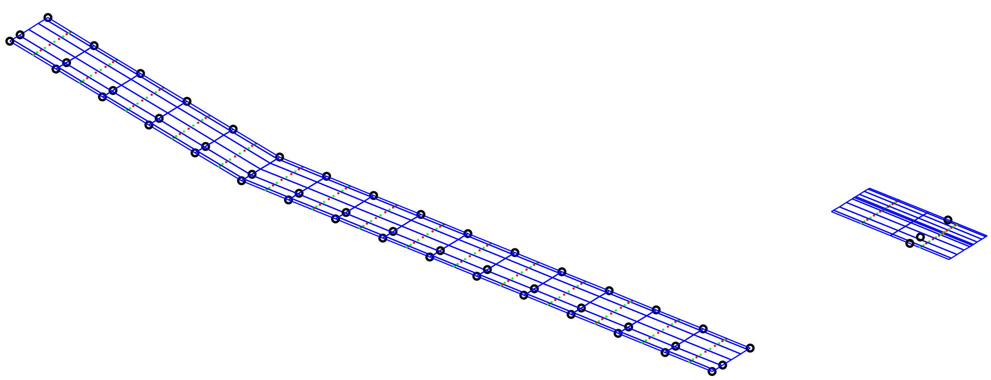

Figure 3.12: Aeroelastic model for coupled MSC Nastran with custom vortex lattice.

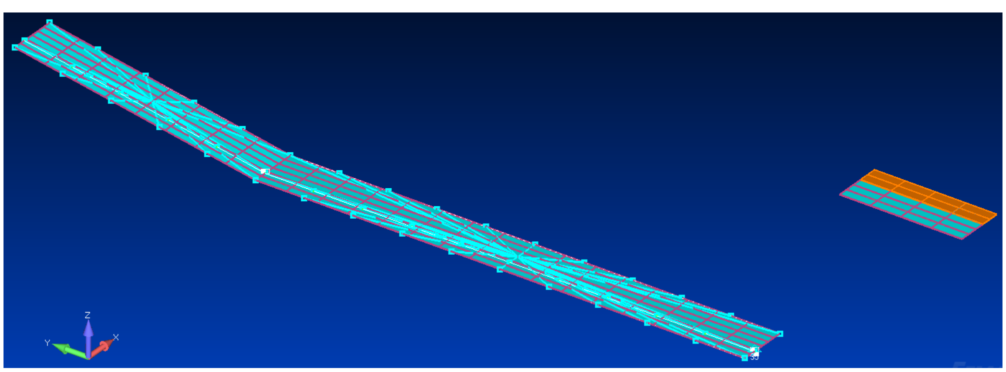

Figure 3.13: MSC Nastran aeroelastic model.

Trim wing deflection and rotation are shown in Figs. 3.14 and 3.15, respectively. The responses are in excellent agreement. Trim angle of attack and elevator deflection are listed in Table 3.5. Slight differences in elevator area, aerodynamic paneling, and aerodynamic solvers may account for the 15% difference in elevator deflection and 4% difference in angle of attack. There should be no difference in mass, inertia, and mass centers because both methods use an identical structural model.

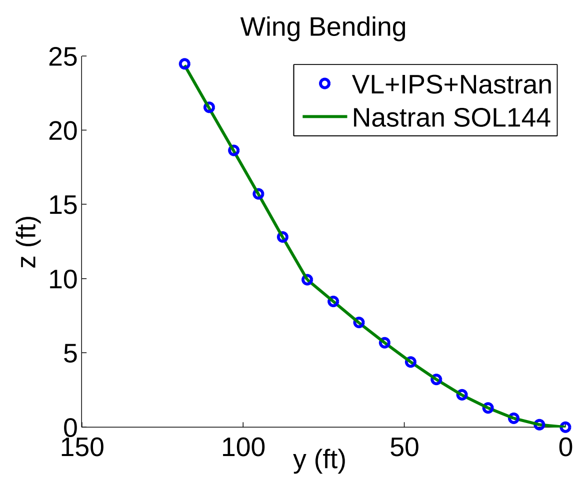

Figure 3.14: Wing bending aeroelastic results for verification.

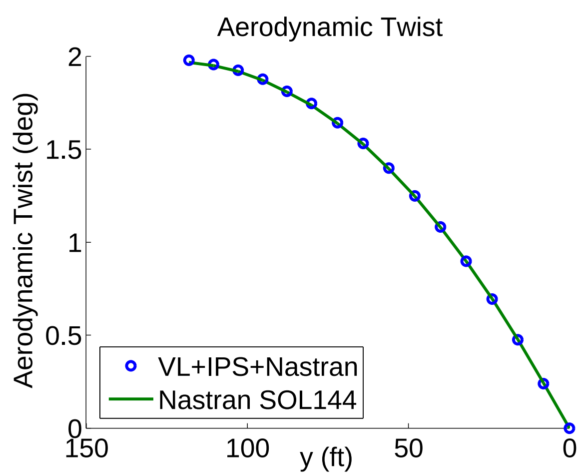

Figure 3.15: Aerodynamic twist aeroelastic results for verification.

The results verify that the aeroelastic code coupling interface is working as intended. For

Table 3.5: Aeroelastic trim results for verification.

	VL+IPS+MSC Nastran	MSC Nastran SOL144
Angle of Attack (deg)	4.4354	4.2568
Elevator Deflection (deg)	-5.6944	-4.9202

geometrically nonlinear aeroelastic trim analysis, options for nonlinear structural analysis are specified in the structural solver inputs. The coupling interface works identically. Nonlinear trim analysis at $1g$ showed a result with 10% more tip deflection than predicted by linear analysis.

3.1.4 Optimization

Optimization methods were verified by testing them on a simple optimization problem with a known solution. Figure 3.16 shows a five design variable cantilever beam problem developed by Svanberg [71].

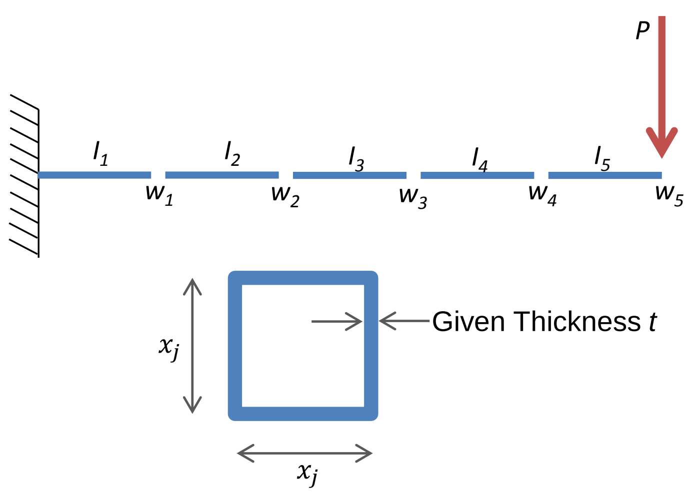

Figure 3.16: Svanberg [71] beam example.

Assuming $t << x_j$

$$I_j = \frac{2}{3}tx_j^3 \tag{3.1}$$

Table 3.6: Traditional SQP design.

	SQP+CoFFe	Svanberg
x_1	6.0160	6.016
x_2	5.3092	5.309
x_3	4.4943	4.494
x_4	3.5015	3.502
x_5	2.1527	2.153
Obj.	0.2479	0.2479
Con.	0.0000	0

for each beam section. The objective of the optimization is to minimize the volume of the structure while constraining the tip deflection. The structure was modeled in CoFFe and optimized using three formulations.

Traditional Sequential Quadratic Programming

The traditional implementation of sequential quadratic programming (SQP) enforces the tip deflection constraint directly. The algorithm uses semi-analytic design sensitivities provided by CoFFe. The resulting design is compared to Svanberg's design in Table 3.6. The design variables agree to three decimal places, the precision reported by Svanberg.

Minimize Descent Function with SQP

The descent function formulation in Eq. (2.43) was first tested as an unconstrained optimization in SQP. Five times the Lagrange multiplier from traditional SQP was used as penalty coefficient for Han and Powell's descent function. The results, shown in Table 3.7. The results are the same as the traditional SQP result to four decimal places, except x_2 which shows a difference of 0.0001, likely due to optimizer tolerance. The design variables agree with Svanberg's to three decimal places. The minimum of the unconstrained descent function was the same as the feasible minimum of the original objective function.

Table 3.7: Descent function SQP design.

	Descent Function SQP+*CoFFe*	Svanberg
x_1	6.0160	6.016
x_2	5.3091	5.309
x_3	4.4943	4.494
x_4	3.5015	3.502
x_5	2.1527	2.153
Obj.	0.2479	0.2479
Con.	0.0000	0

Table 3.8: Descent function DIRECT design.

	Descent Function DIRECT+*CoFFe*	Svanberg
x_1	5.9851	6.016
x_2	5.3531	5.309
x_3	4.4982	4.494
x_4	3.5081	3.502
x_5	2.1308	2.153
Obj.	0.2479	0.2479
Con.	-0.0004	0

Minimize Descent Function with DIRECT

The descent function formulation is intended to be used with the DIRECT optimizer to search for global optima. That approach was tested on the Svanberg beam problem. The DIRECT optimizer produced the design in Table 3.8 given 20,000 function evaluations. For demonstration purposes, DIRECT was not given the solution from SQP as the center of the design bounds. The exercise shows that using a DIRECT optimizer with Han and Powell's descent function is a viable method to search for global optima.

3.2 Systematic Optimization Results

3.2.1 Static Response Quality

Figures 3.17 – 3.19 show the static response quality of the best designs from from the systematic optimization described by Eqs.(2.39) and (2.41). The plots show the sum of the squares of the residuals, $\mathcal{SSR}_{TMN}$, between the target and scaled models for both linear and nonlinear response to 2.5g target aeroelastic trim loads. This is only a partial quality metric, as it does not indicate the quality of the design when considering dynamics or other static loading conditions.

Figure 3.17 shows the results for models optimized using only vibration eigenpair matching. There is no discernible trend in the results. The linear static response quality for $N_v = 1$ and $N_v = 3$ is noticeably lower than the others. Reduction in quality from $N_v = 2$ to $N_v = 3$ is attributed to a worsening of the matching of all modes other than mode 3 when adding mode 3 to the optimization problem. This is apparent by referencing Table A.2. Notice that all modes other than mode 3 decrease in quality when mode 3 is added to the objective function. Subsequent addition of mode 4 results in improved quality of modes 5, 6, and 7 over the design for $N_v = 3$.

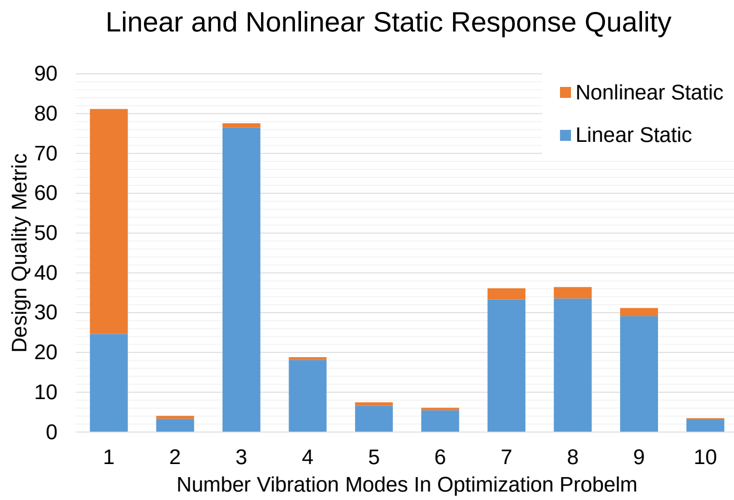

Figure 3.17: Static response quality with only vibration eigenpair matching.

Figure 3.18 shows results for scaled designs that included matching the linear static response in the optimization problem. It should first be noted that both the linear and nonlinear static response qualities outperformed the previous results. Because the linear static response was directly included in the optimization, the blue bar is lowest when nothing else is optimized, and tends to be lower when fewer other things were included in the weighted objective function. The nonlinear static response did benefit from including the first mode shape. This was assumed to mostly be due to better mass distribution from the mode shape matching and a more determined (farther from underdetermined) optimization problem. Applied aeroelastic loads include gravitational acceleration, so mass distribution affects the static response. Figure 3.19 shows the same result for scaled designs that included both linear static response matching and matching of the first buckling eigenpair in the optimization. The results are qualitatively and quantitatively similar to the results without the buckling eigenpair matching, but the nonlinear response quality is slightly better with buckling eigenpair matching.

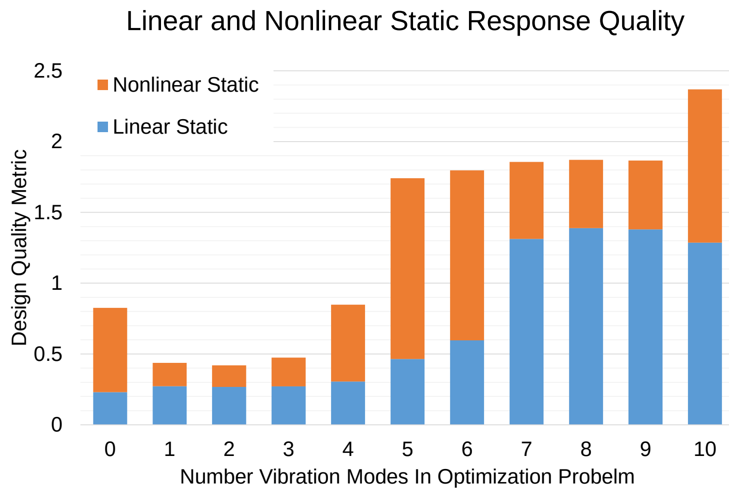

Figure 3.18: Static response quality with linear statics matching and vibration eigenpair matching.

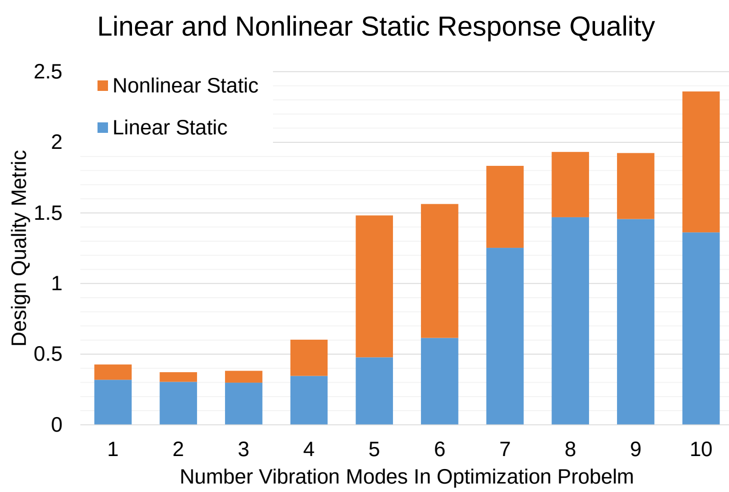

Figure 3.19: Static response quality with linear statics, one buckling eigenpair, and vibration eigenpair matching.

3.2.2 Vibration Response Quality

Figures 3.20 – 3.22 show the vibration response quality of the best designs from from the systematic optimization. The plots show the sum of the squares of the residuals, $\mathcal{SSR}_{TMN}$, between the target and scaled models for the first ten vibration mode shapes, and the absolute fractional deviation of the first ten natural frequencies from the target values.

Figure 3.20 shows the results for only vibration eigenpair matching. Mode swapping and mixing tend to corrupt the $\mathcal{SSR}_{TMN}$ for low N_v. As modes were added to the optimization the swapping and mixing drastically reduced. For these results, swapping and mixing did not occur for optimal eigenpairs that were included in the optimization. As expected, Fig. 3.20b indicates that the vibration frequency differences tend to reduce as they were constrained. Vibration eigenpair quality for designs that included linear statics matching are shown in Fig. 3.21. The trends are similar to Fig. 3.20, but mode swapping is reduced for small N_v Vibration eigenpair quality results for designs that included linear statics and one vibration eigenpair matching, shown in Fig. 3.22, are very similar to Fig. 3.21, but mode shape quality and frequency deviation are slightly worse for most N_v.

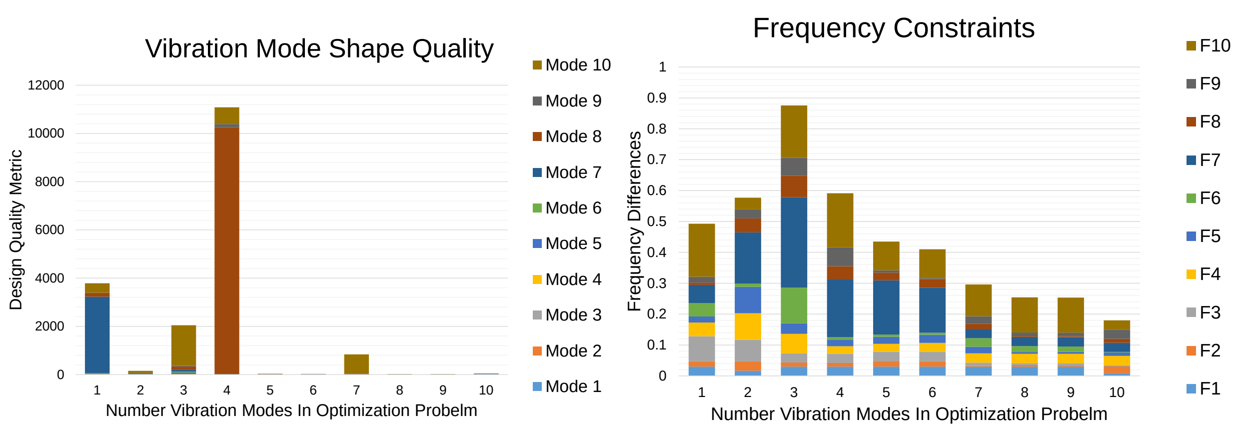

(a) Mode shape quality.

(b) Frequency constraint.

Figure 3.20: Vibration eigenpair quality with only vibration eigenpair matching.

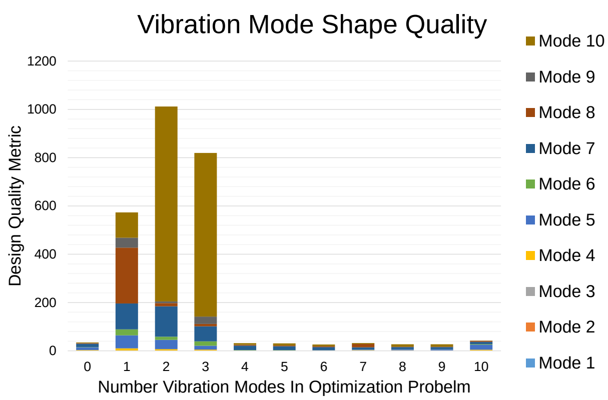

(a) Mode shape quality.

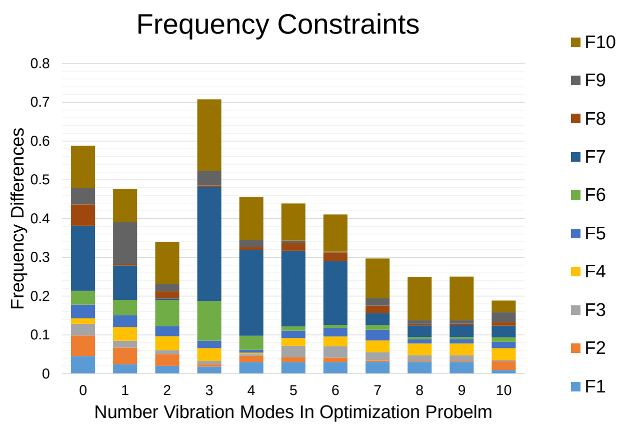

(b) Frequency constraint.

Figure 3.21: Vibration eigenpair quality with linear statics and vibration eigenpair matching.

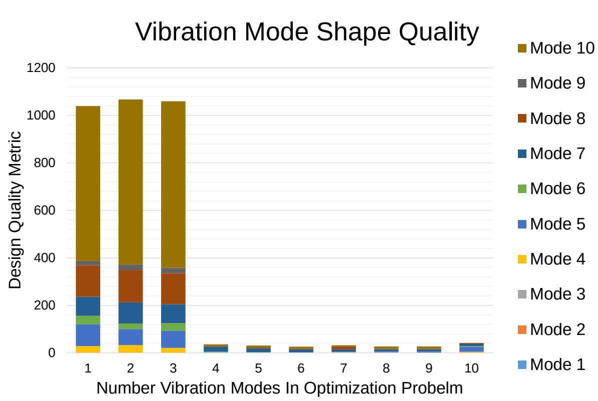

(a) Mode shape quality.

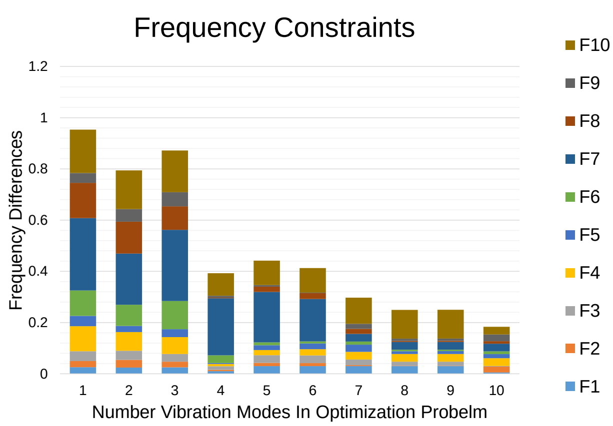

(b) Frequency constraint.

Figure 3.22: Vibration eigenpair quality with linear statics, one buckling eigenpair, and vibration eigenpair matching.

3.2.3 Optimizer Performance Review

Results from the multistart optimization with SQP are shown in Table 3.9. The first three columns identify the number of eigenpairs and the linear statics option for the optimization case. The fourth column shows the number of random initial conditions that were investigated. The fifth column shows the number of cases that ultimately converged to a design that satisfied the convergence criteria. The sixth and seventh columns show the number of unique designs and unique objective function values, respectively. For this table, a unique design has at least one design variable that is at least 2.5% different than any other design, and a unique objective function value is at least 2.5% different than any other objective function value. The seventh and eighth columns show the mean number of function and gradient evaluations used for each optimization attempt (even attempts that did not converge).

For small N_v, formulations that omit linear statics matching are close to underdetermined, and they result in a greater number of unique design and objective function values than formulations that include linear statics matching. The multistart optimization was fairly exhaustive. At least 100 random initial conditions were attempted for each case. For each case, the result with the lowest objective function was used as the center of the design space for a DIRECT optimization.

DIRECT was allowed 150,000 function evaluations. The Jones factor [26] was set to 0.01. No feasible designs (satisfying Eqs. (2.40–2.41) within tolerance) from DIRECT had a better objective function (Eq. (2.39)) than the best from multistart with SQP. An increase in the number of function evaluations could result in designs from DIRECT that outperform the multistart optimization. Also, starting with a less exhaustive database of multistart solutions might mean that DIRECT will produce designs that outperform the multistart designs.

Table 3.9: Multistart optimization results.

N_v	N_b	Linear Statics	Multistarts	Converged Cases	Unique Designs	Unique Objective Values	Mean Fun. Evals.	Mean Grad. Evals.
1	0	No	500	447	73	26	133.752	86.458
2	0	No	500	391	42	11	148.596	104.5
3	0	No	500	401	38	23	132.852	85.32
4	0	No	500	320	28	14	90.726	53.676
5	0	No	500	294	26	12	69.972	44.896
6	0	No	500	173	25	9	43.14	24.758
7	0	No	500	109	8	7	33.416	17.886
8	0	No	500	66	6	3	21.154	11.436
9	0	No	500	55	17	2	19.71	10.434
10	0	No	500	24	3	1	9.488	4.888
1	0	Yes	100	99	2	2	81.14	47.46
2	0	Yes	100	96	3	3	79.63	44.34
3	0	Yes	100	93	6	6	87.16	52.31
4	0	Yes	100	81	3	3	80.87	44.8
5	0	Yes	100	84	3	3	64.48	39.71
6	0	Yes	100	61	5	3	54.97	31.25
7	0	Yes	100	45	4	4	39.92	24.7
8	0	Yes	100	38	7	3	40.46	22.94
9	0	Yes	100	22	3	2	35	18.88
10	0	Yes	100	5	2	1	13.33	5.73
1	1	Yes	100	96	2	2	91.43	41.28
2	1	Yes	100	93	3	3	91.52	47.7
3	1	Yes	100	90	2	2	81.16	45.55
4	1	Yes	100	86	2	2	58.22	32.85
5	1	Yes	100	84	2	2	52.43	29.86
6	1	Yes	100	62	2	2	49.38	26.82
7	1	Yes	100	48	2	2	39.8	19.73
8	1	Yes	100	39	3	3	31.39	16.42
9	1	Yes	100	30	3	2	36.2	17.56
10	1	Yes	100	13	1	1	25.63	9.84

3.2.4 Select Results

The scaled model design from optimizing the first three vibration eigenpairs and the linear static response of the scaled model is compared to the target aeroelastic response in this section. The structural load steps to a converged $2.5g$ nonlinear aeroelastic trim response are shown in Fig. 3.23. Tip and mid aft-wing deflection and twist are shown on separate subplots. The buckling load is shown at around load factor 2, so the plotted nonlinear response proceeds beyond the buckling load.

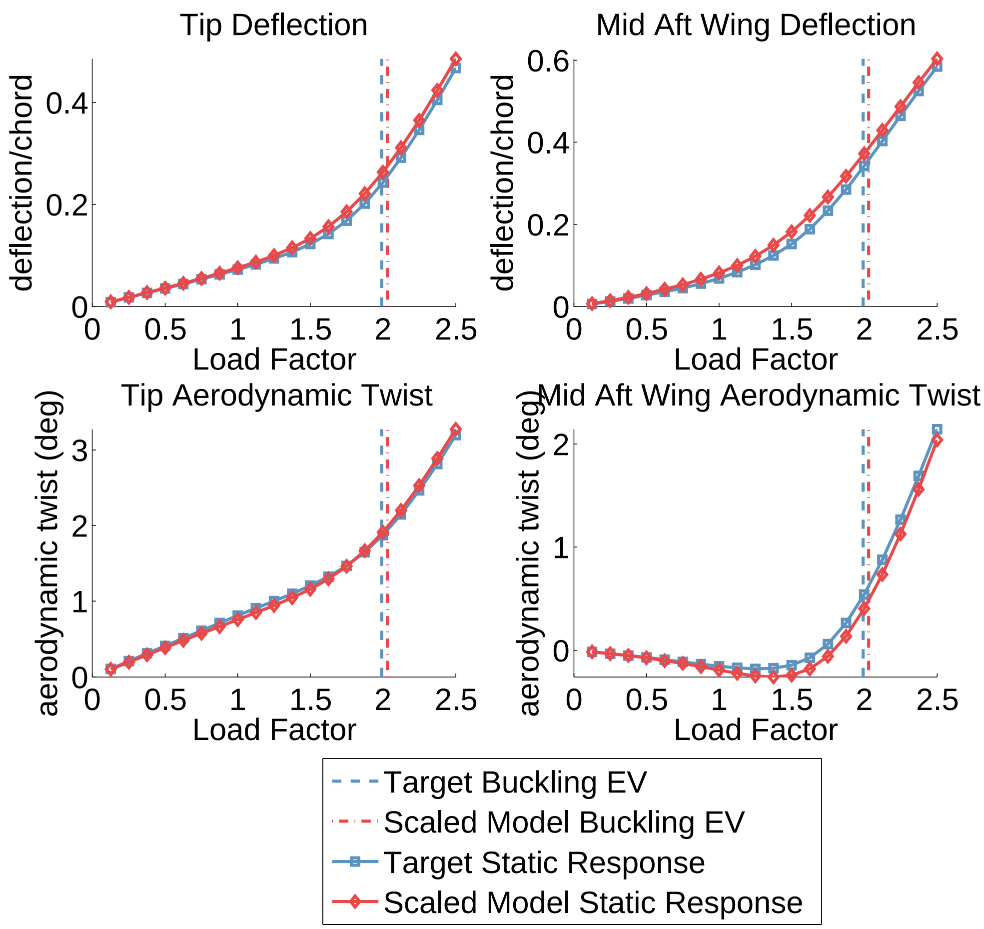

Figure 3.23: Response to 2.5 nonlinear aeroelastic trim loads.

The converged $2.5g$ nonlinear aeroelastic trim response of the deformed spline points of the target and scaled models is shown in Fig. 3.24. These are actual (×1) chord normalized displacements. The response is significantly large to require consideration of geometric nonlinearities. The target and scaled models agree quite well.

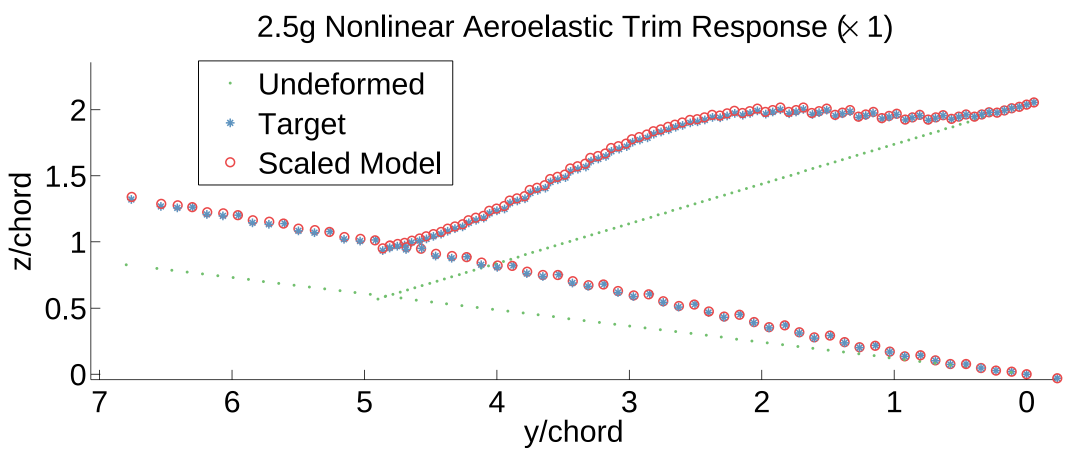

Figure 3.24: Response to 2.5g nonlinear aeroelastic trim loads.

Agreement is also good for rotations, shown in Fig. 3.25. Rotations $R1$, $R2$, and $R3$ are defined as rotations about the aircraft x, y, and z axes, respectively. The aircraft coordinate system is labeled in Fig. 2.9. Aerodynamic twist rotation, $R2$, exceeds 10 degrees in part of the aft wing. Results from potential flow aerodynamics are suspect in regions where section angle of attack becomes large.

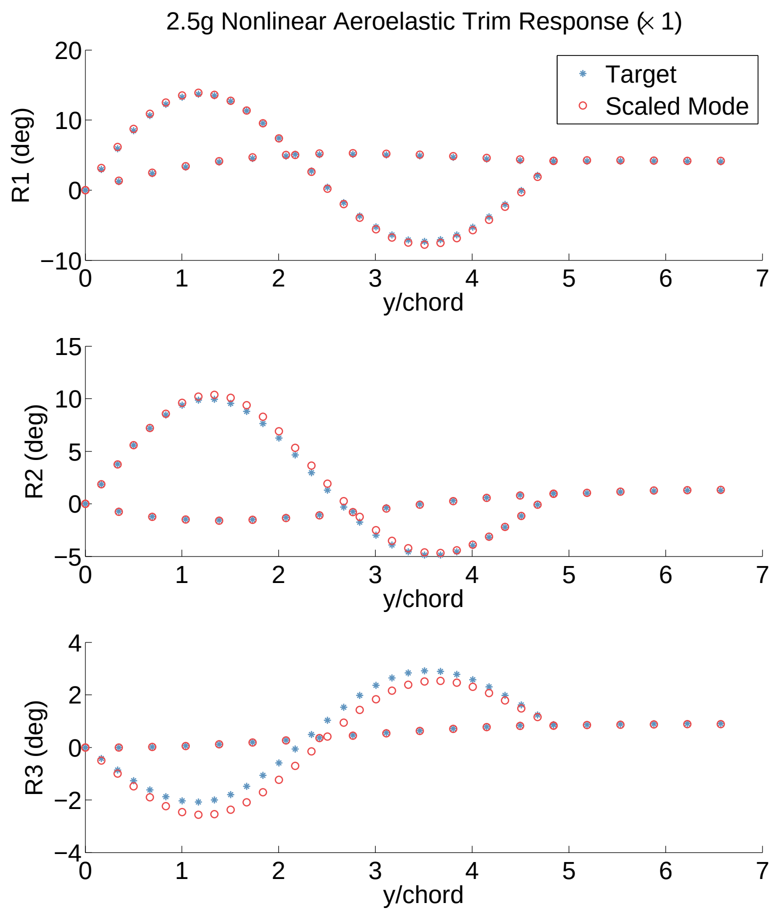

Figure 3.25: Response to 2.5g nonlinear aeroelastic trim loads.

To asses the dynamics, the first four aeroelastic reduced frequencies and damping are compared to the target model in Fig. 3.26. Results in Fig. 3.26aare obtained by linearizing the stiffnesses about the 1g nonlinear aeroelastic trim state. Results in Fig. 3.26b are obtained using the undeformed (linear) stiffnesses.

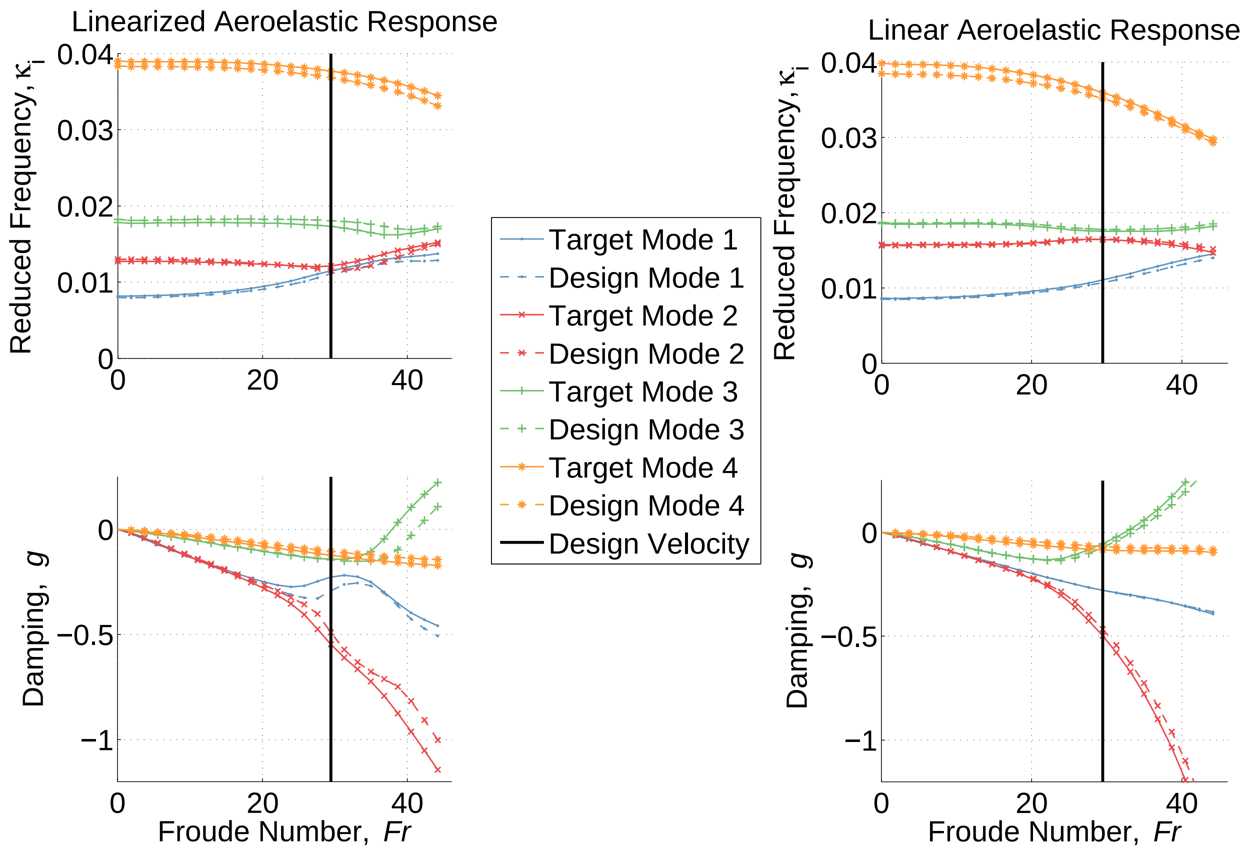

(a) Stiffness linearized about $1g$ nonlinear trim.

(b) Undeformed stiffness.

Figure 3.26: Dynamic aeroelastic response.

The design Froude number, where the aircraft is trimmed, is indicated by the vertical black line. The target and scaled model dynamic aeroelastic responses agree well throughout the velocity profile for both the linear and linearized stiffnesses. Negative aeroelastic damping is an indication of aeroelastic stability. A flutter instability is predicted when mode 3 crosses zero. Target and scaled design flutter speeds agree very well for the linear stiffness results and reasonably well for the linearized stiffness results. Changes in stiffness from the undeformed state to the deformed state cause a slight delay in flutter speed. The linearized flutter mode shapes agree closely; the modes shapes are plotted in Fig. 3.27. Primary participants in the flutter mode shapes are

- mode 1 – forwarding wing 1^{st} bending,
- mode 3 – forwarding wing 2^{nd} bending and aft wing 1^{st} bending, and
- mode 6 – forwarding wing 1^{st} twist and aft wing 2^{nd} bending.

Bending implies out-of-plane bending.

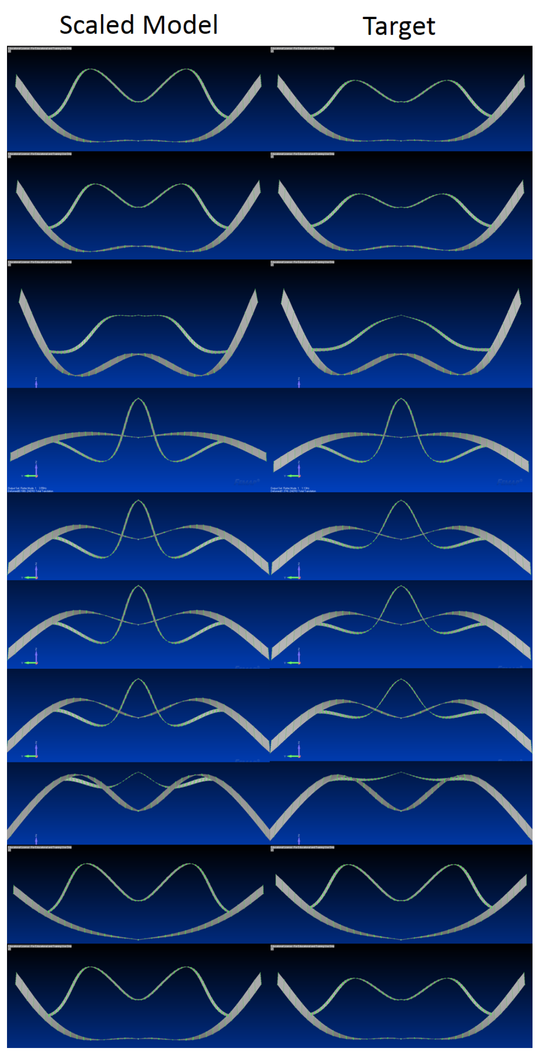

Figure 3.27: Linearized flutter mode comparison.

The scaled model presented in this section was designed using the modern scaling approach described in Chapter 2. A sufficiently high quality design, even for a case with significant geometric nonlinearity, was attained using the method.

3.2.5 Other Aeroelastic Results

Figures A.1 – A.16 show additional aeroelastic results for other optimal designs with different terms included in the optimization. The design from optimizing linear statics, one buckling eigenpair, and three vibration eigenpairs is very similar to the previously presented select results; linearized flutter speed was slightly closer to the target value, but aeroelastic mode 4 was not as close. Other cases did not match the target aeroelastic response as well as the previously presented select results. Flutter speed was particularly difficult to match precisely. Increasing the number of vibration eigenpairs from three to six did not improve the flutter agreement, nor did reducing the number of vibration eigenpairs from three to two. Including the linear static response matching greatly improved the matching of the aeroelastic responses. Including the first buckling eigenpair with linear statics in the optimization did not substantively improve aeroelastic response when compared to cases where linear statics was matched while omitting the first buckling eigenpair.

3.2.6 Select Modern Scaling Results Verses Classical Scaling

Cross-sectional analysis on the target model and on the scaled model design presented in Section 3.2.4 provides the cross-sectional properties in Tables 3.10 and 3.11. The tables are color coded so that green indicates the quantities are matching, orange indicates the quantities presumed to be matching coincidentally, and red indicates the quantities are not matching.

The magnitude of nondimensional parameters $\frac{I_1}{AL^2}$ and $\frac{I_2}{AL^2}$ are indications of the impor-

Table 3.10: Forward wing cross-section properties.

	$\frac{I_1}{AL^2}$	$\frac{I_2}{AL^2}$	$\frac{EA}{L^3}$	$\frac{EI_1}{L^5}$	$\frac{EI_2}{L^5}$	$\frac{GJ_{eff}}{L^5}$
Target FW	1.1654e-05	0.0010616	1153.8914	0.013448	1.2249	0.0176
Scaled Model FW	1.1693e-06	0.00011009	11620.292	0.013587	1.2792	0.0173

Table 3.11: Aft wing cross-section properties.

	$\frac{I_1}{AL^2}$	$\frac{I_2}{AL^2}$	$\frac{EA}{L^3}$	$\frac{EI_1}{L^5}$	$\frac{EI_2}{L^5}$	$\frac{GJ_{eff}}{L^5}$
Target AW	5.4132e-06	0.00010936	589.613	0.0031917	0.064481	0.0039
Scaled Model AW	1.9346e-06	9.995e-05	1715.8183	0.0033194	0.1715	0.0036

tance of matching the axial stiffnesses. These will be discussed in more detail and referenced in the next section. The tables show clearly that the scaled model does not reproduce the axial stiffnesses or the aft wing in-plane-bending stiffness of the target model. A high-quality matching of the nonlinear aeroelastic response was achieved without matching those scaled parameters. From these results, it is asserted that a classical scaling approach that matched only out-of-plane bending stiffnesses, twist stiffness, in-plane bending stiffness of the forward wing, and the distributed generalized masses could produce a high quality scaled design.

3.2.7 Full-Scale Joined-Wing Buckling Mode

The first buckling mode of the joined-wing configuration of Blair *et al.* [13], shown in Fig. 3.28b, shows lateral-torsional type buckling of the aft wing. The target joined-wing demonstration model (Fig. 3.28a) shows much less aft-wing torsional response in the fist buckling mode; the aft-wing response is better classified as Euler buckling. Converged aeroelastic loads were used at the reference load case for both models.

Euler buckling is an instability that results in weak-axis bending and is due to bending-stiffness axial-force coupling. Lateral-torsional buckling is an instability that results in torsion and lateral displacement and is due to torsional-stiffness and weak-axis bending stiffness coupling with strong-axis moment. The buckling eigenvector mode differences between the Blair *et al.* [13] model and the joined-wing demonstration model are due to geometry and stiffness differences that lead to difference internal force-stiffness coupling. It is unnecessary for the buckling modes to be qualitatively similar for this work.

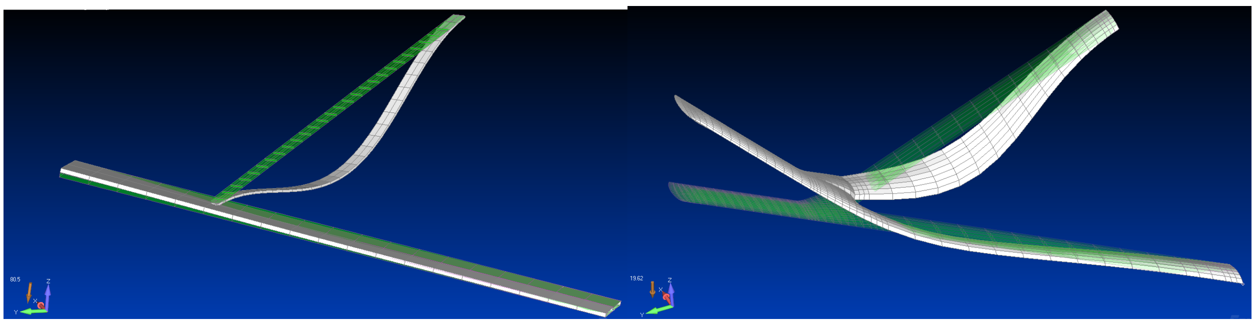

(a) Full-scale target buckling mode. (b) Blair *et al.* [13] model buckling mode.

Figure 3.28: Dynamic aeroelastic response.

3.3 Internal Loads

Coupling between stiffnesses and internal loads is a key nonlinear kinematic effect. The most prominent coupling is between beam transverse stiffness and axial force. Select results show that high-quality scaled designs can be achieved without matching the axial stiffness. This section is an effort to explain how the global internal forces can be matching without matching all stiffnesses. A simple example is used used to show that internal loads can be insensitive to stiffness changes in certain "regions" of a nondimensional stiffness parameter. Quantifying the importance of matching axial stiffness in the scaling optimization is possible by relating a specific application to the derived stiffness parameter. For additional insight, internal load sensitivities for the joined-wing demonstration problem are presented.

3.3.1 Two Beam Plane Frame

The parameterized two beam plane frame shown in Fig. 3.29 is clamped at the left boundary and joined on the right. A vertical force is applied at the joint. The structure is statically indeterminate. For this loading condition, the analytic solution to the linear structural response can be exactly reproduced with two frame finite elements. The finite element method was solved symbolically for the parameterized structure.

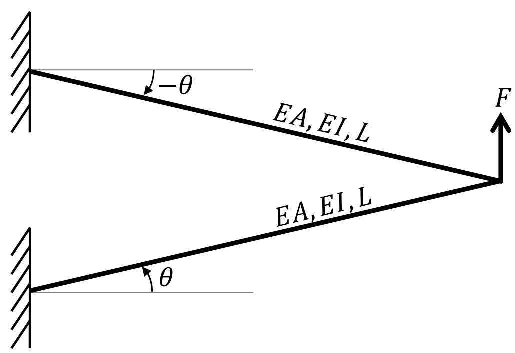

Figure 3.29: Parameterized two-beam frame.

The load normalized internal axial force, P, of the top beam is

$$\frac{P}{F} = \frac{-1}{2\sin(\theta) + 6\cos(\theta)\cot(\theta)\frac{EI}{EAL^2}}. \tag{3.2}$$

The equation is in terms of nondimensional parameters $\frac{P}{F}$, θ, and $\frac{EI}{EAL^2}$. $\frac{P}{F}$ is plotted for a wide range of θ and $\frac{EI}{EAL^2}$ in Fig. 3.30. The surface plot is clipped (the shaded region at the bottom right corner) at $\frac{P}{F} = -1.0$ because there is an asymptotic region where $-2\sin(\theta) \rightarrow 6\cos(\theta)\cot(\theta)\frac{EI}{EAL^2}$.

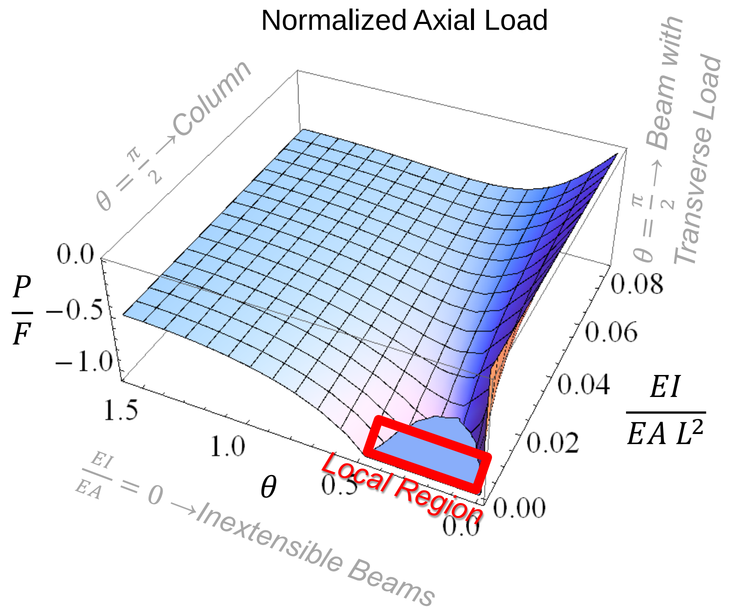

Figure 3.30: Parameterized two-beam frame.

Equation (3.2) and Fig. 3.30 show how the internal force depends on the stiffness parameter and the shape of this indeterminate structure. The relationship can be used to inform the joined-wing scaling demonstration problem. The geometry and stiffness of the target aeroelastic model were used to select the parameters for Eq. (3.2). The global geometry is fixed for scaling problems, so target aft-wing anhedral of 14° was selected for θ in Eq. (3.2). The stiffness of the scaled model structure must be optimized suitably during the design process. Target model results show significant transverse displacement, so it is essential that EI is scaled. Target model results do not show significant axial displacement, but axial stiffness could be important, if the internal loads are sensitive to EA. Equation (3.2) offers insight to this relationship. The cross-sectional geometry will change from a skin-spar-rib construction for the full-scale model to a ladder-skin fairing construction in the scaled model. With this configuration, the scaled axial stiffness will need to increase in order to reproduce the scaled bending stiffness. Thus, the parameter $\frac{EI}{AL^2}$ was bound at $\frac{EI_2}{AL^2}$ from the target model. The comparable local region is shown by the red box in Fig. 3.30 and is expanded in Fig. 3.31.

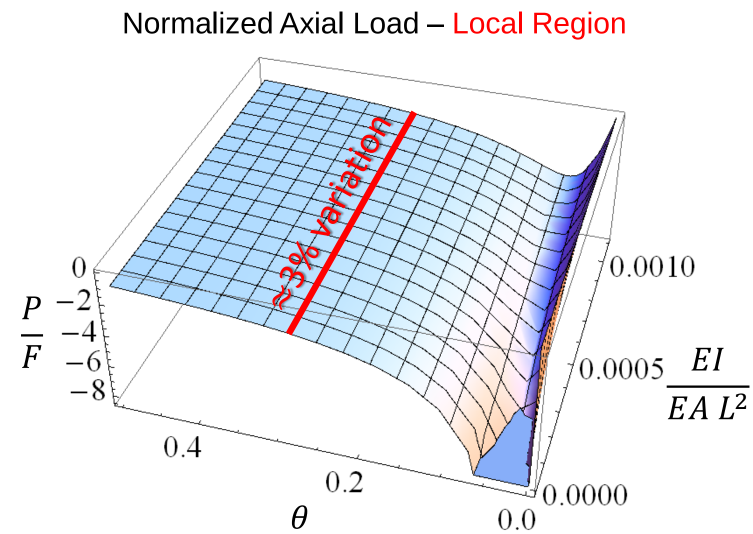

Figure 3.31: Parameterized two-beam frame related to joined-wing problem.

The result shows that as $\frac{EI}{EAL^2} \to 0$ or $EA \to \infty$ there is only roughly a 3% deviation in internal axial force from the target stiffness. The response may be sufficiently insensitive to neglect axial stiffness in the scaled model optimization. Sensitivity of the actual joined-wing demonstration configuration is presented in more detail in the next section. Future joined-wing scaling efforts can used Eq. (3.2) as demonstrated to gauge the necessity of axial stiffness matching.

3.3.2 Three-Dimensional Joined-Wing Configuration

A beam model was created based on the cross-sectional parameters in Tables 3.10 and 3.11. Generalized internal forces of the linear response to 2.5g aeroelastic loads are shown in Fig. 3.32. Figure 3.32a shows an aft wing axial compression that exceeds 70 lbs for a scaled model that weighs 137 lbs. Semi-analytic sensitivities of the generalized internal loads, P_{gen}, with respect to the generalized beam stiffnesses, K_{gen}, were calculated using

Those results are shown in Figs. 3.33 – 3.40. The sensitivities are multiplied by the ratio of generalized stiffness to the maximum generalized internal forces in order to provide a normalized differential sensitivity

$$\frac{\partial P_{gen}}{\partial K_{gen}} \frac{K_{gen}}{\max(|P_{gen}|)}. \tag{3.3}$$

The results shows a fractional change in generalized internal load per unit change in generalized stiffness.

Figures 3.33 and 3.34 show that none of the generalized internal forces are sensitive to the forward or aft wing axial stiffness for this problem. The remaining generalized stiffnesses, with the exception of aft wing twist, show much more internal force influence.

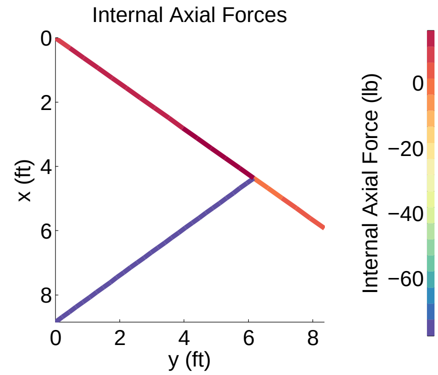

(a) Internal axial force.

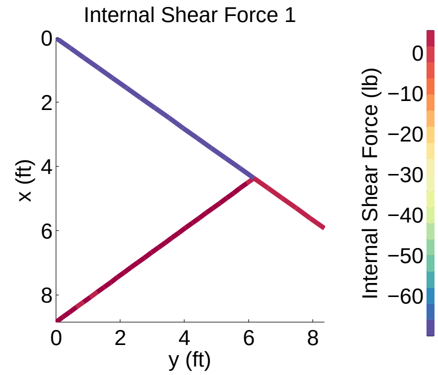

(b) Internal shear.

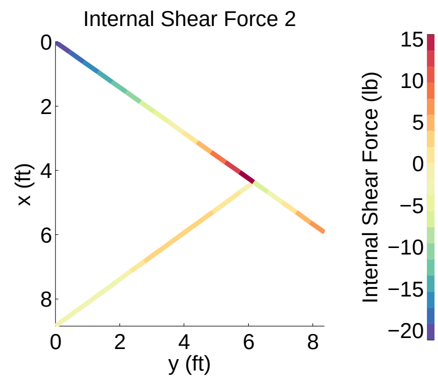

(c) Internal shear.

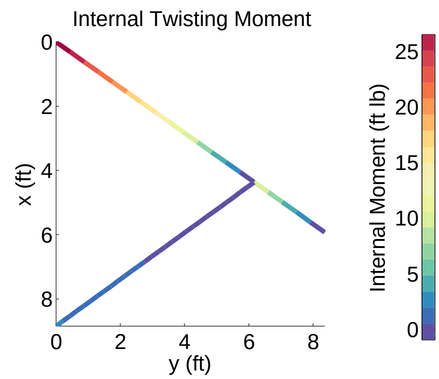

(d) Internal moment.

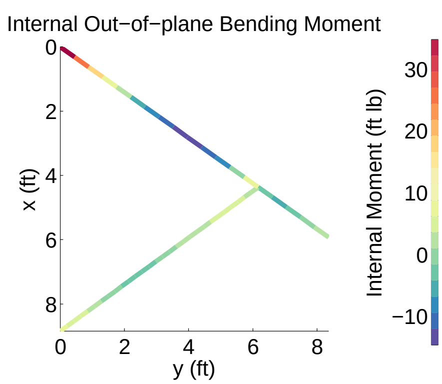

(e) Internal moment.

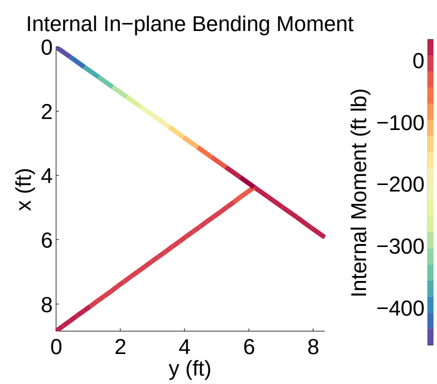

(f) Internal moment.

Figure 3.32: Internal generalized forces

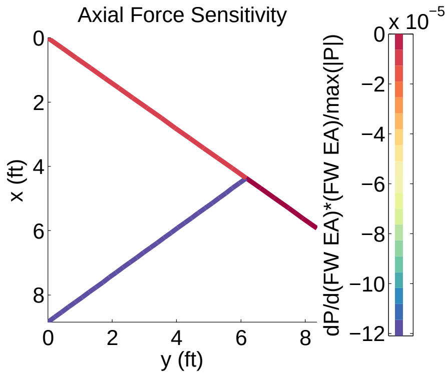

(a) Internal axial force sensitivity.

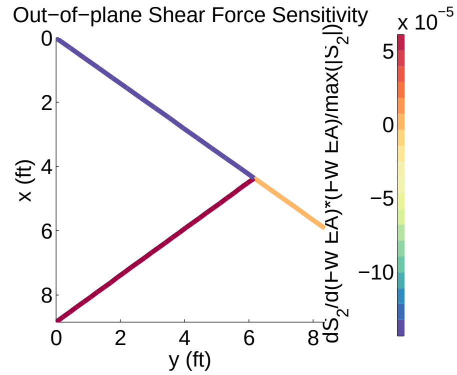

(b) Internal shear sensitivity.

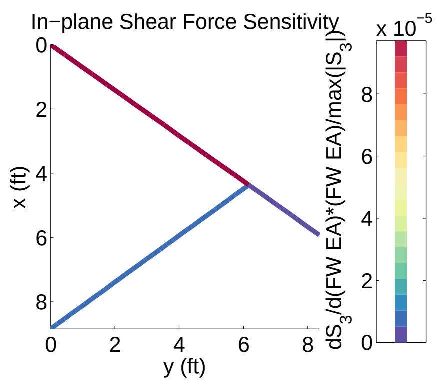

(c) Internal shear sensitivity.

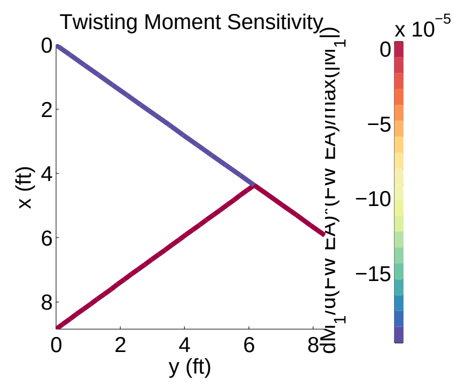

(d) Internal moment sensitivity.

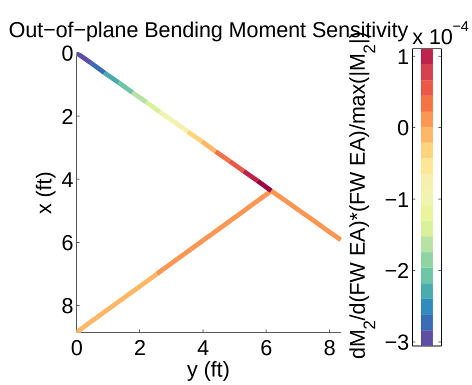

(e) Internal moment sensitivity.

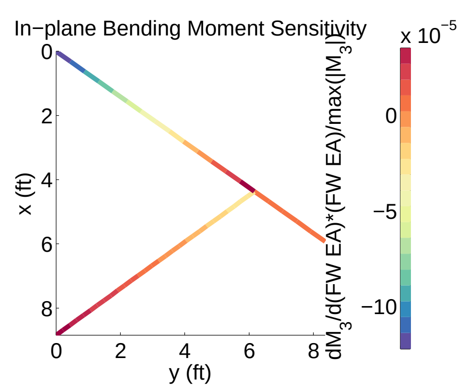

(f) Internal moment sensitivity.

Figure 3.33: Internal generalized force sensitivities to forward wing axial stiffness.

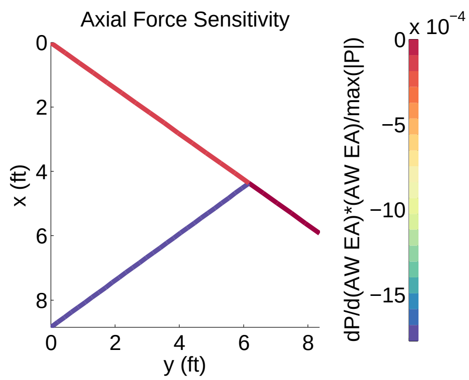

(a) Internal axial force sensitivity.

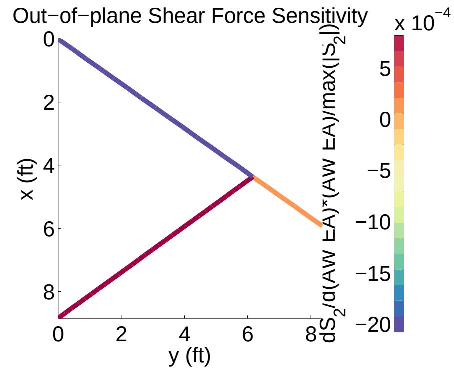

(b) Internal shear sensitivity.

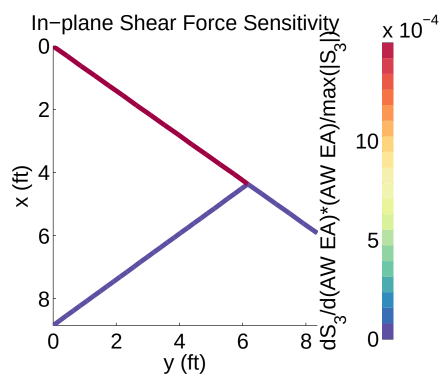

(c) Internal shear sensitivity.

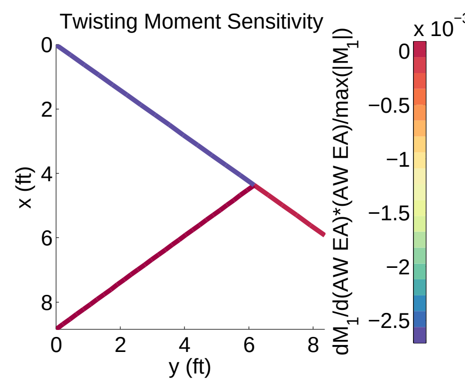

(d) Internal moment sensitivity.

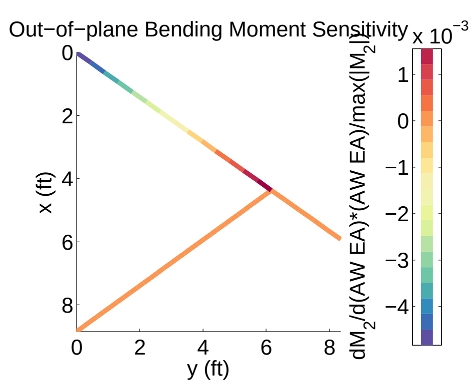

(e) Internal moment sensitivity.

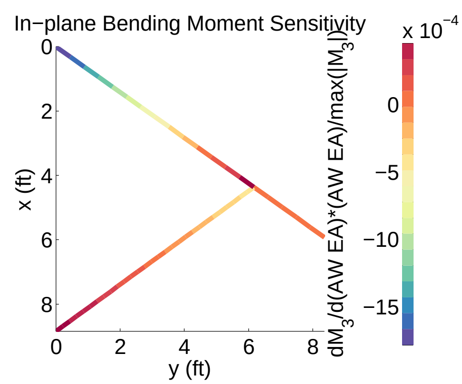

(f) Internal moment sensitivity.

Figure 3.34: Internal generalized force sensitivities to aft wing axial stiffness.

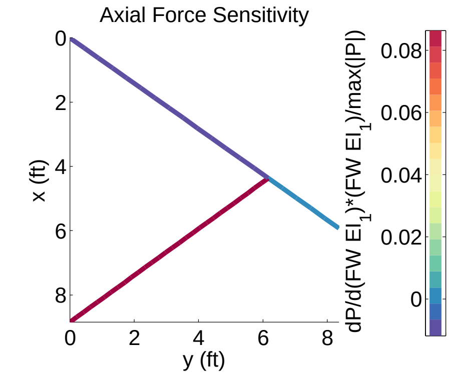

(a) Internal axial force sensitivity.

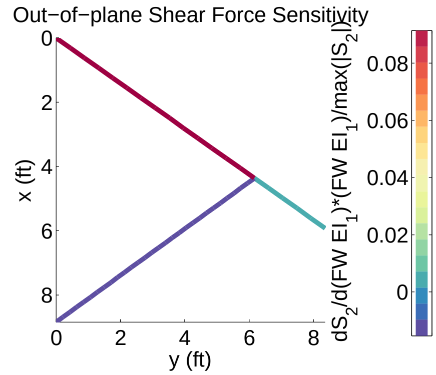

(b) Internal shear sensitivity.

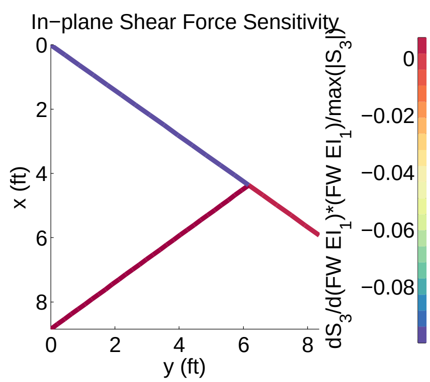

(c) Internal shear sensitivity.

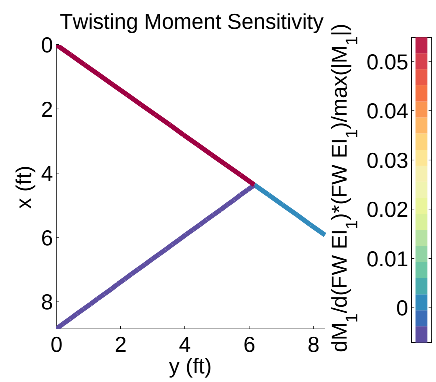

(d) Internal moment sensitivity.

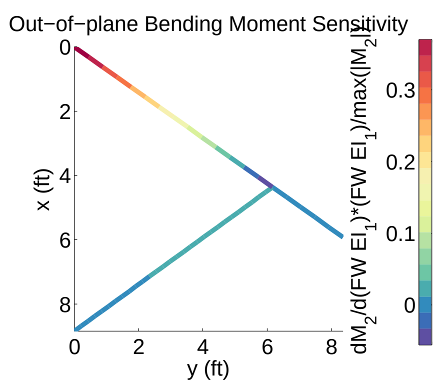

(e) Internal moment sensitivity.

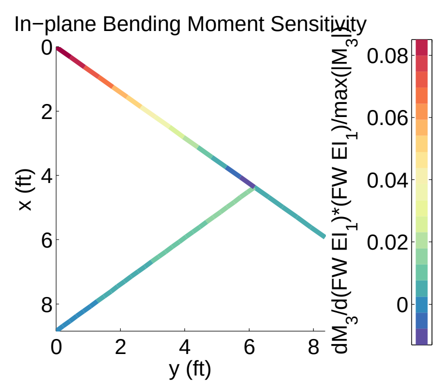

(f) Internal moment sensitivity.

Figure 3.35: Internal generalized force sensitivities to forward wing out-of-plane bending stiffness.

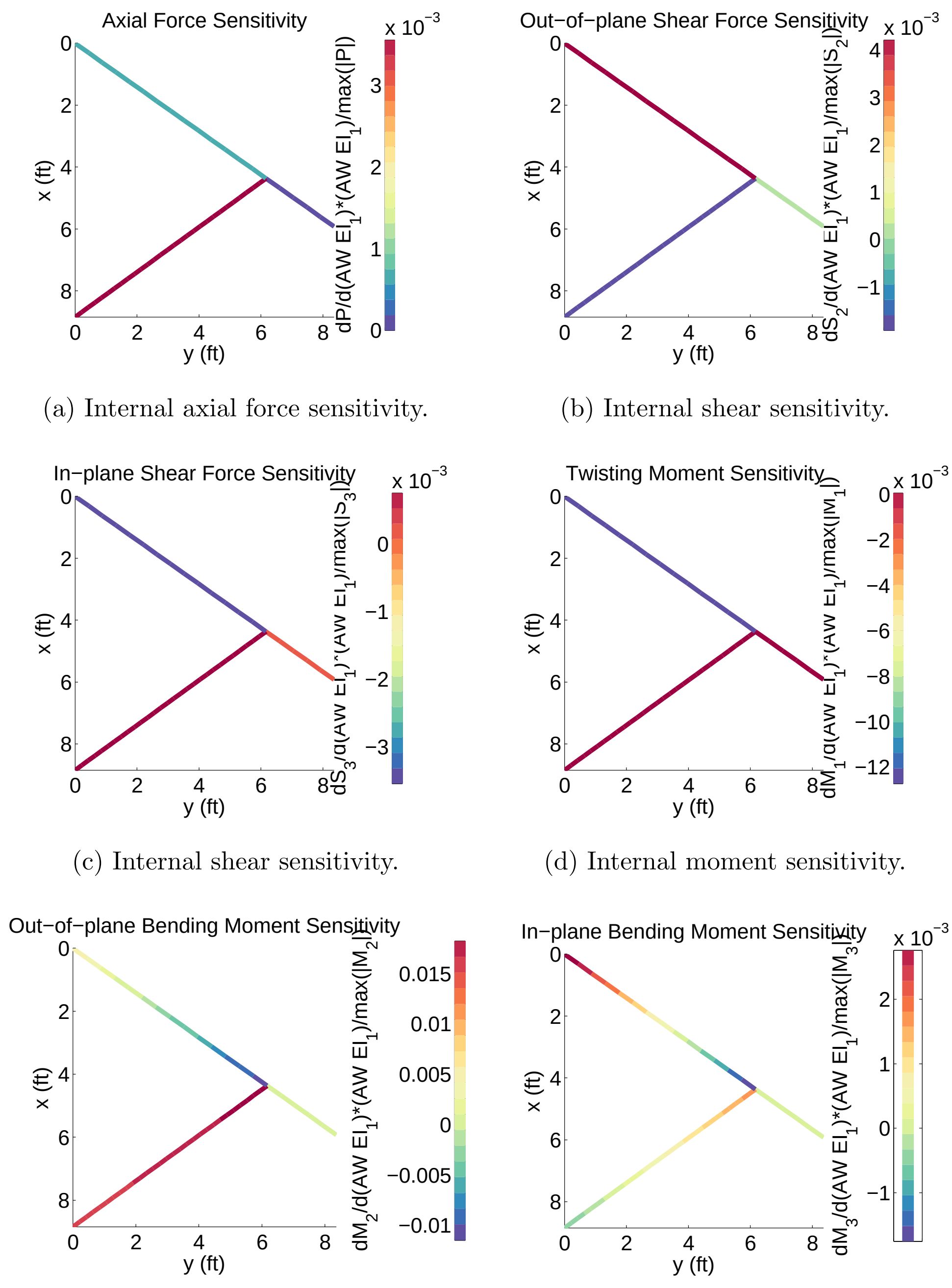

(a) Internal axial force sensitivity.

(b) Internal shear sensitivity.

(c) Internal shear sensitivity.

(d) Internal moment sensitivity.

(e) Internal moment sensitivity.

(f) Internal moment sensitivity.

Figure 3.36: Internal generalized force sensitivities to aft wing out-of-plane bending stiffness.

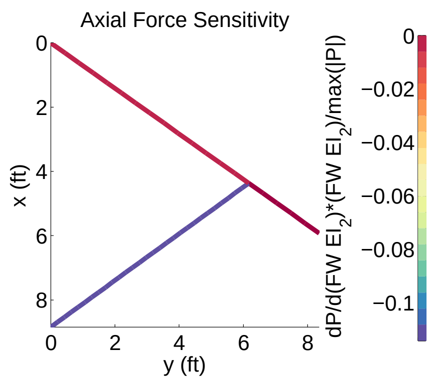

(a) Internal axial force sensitivity.

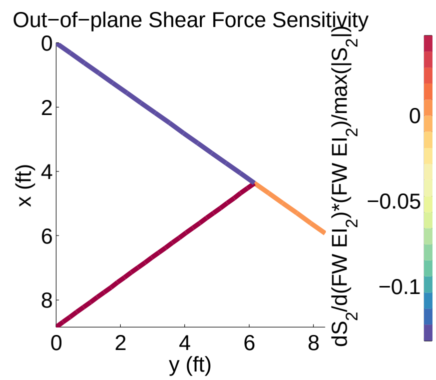

(b) Internal shear sensitivity.

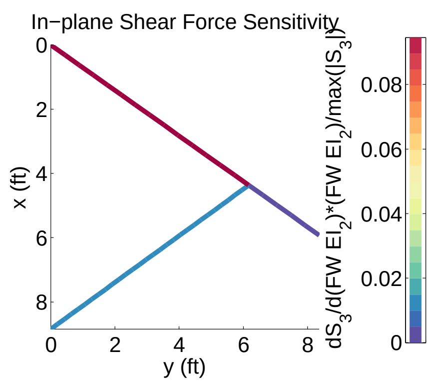

(c) Internal shear sensitivity.

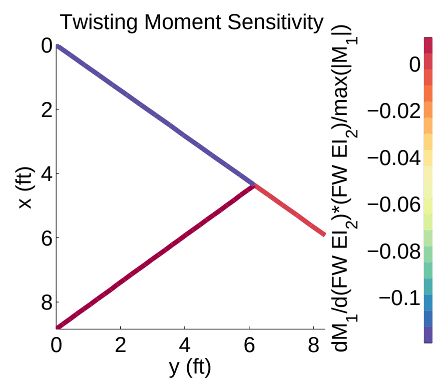

(d) Internal moment sensitivity.

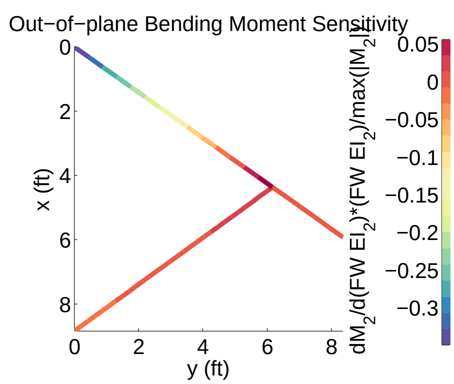

(e) Internal moment sensitivity.

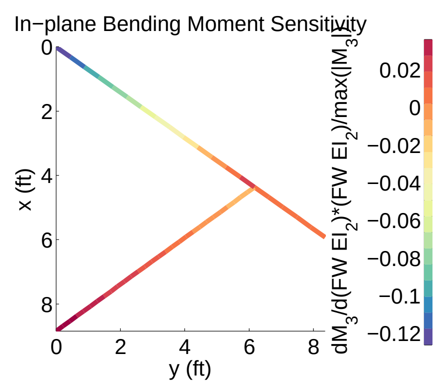

(f) Internal moment sensitivity.

Figure 3.37: Internal generalized force sensitivities to forward wing in-plane bending stiffness.

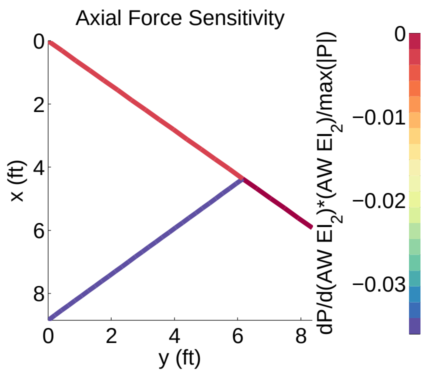

(a) Internal axial force sensitivity.

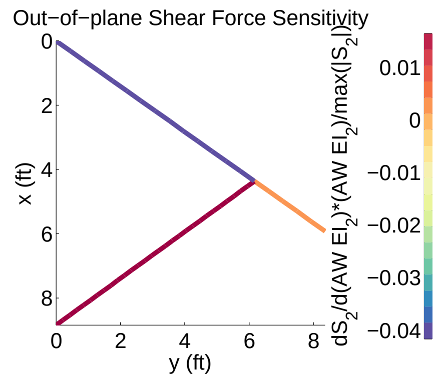

(b) Internal shear sensitivity.

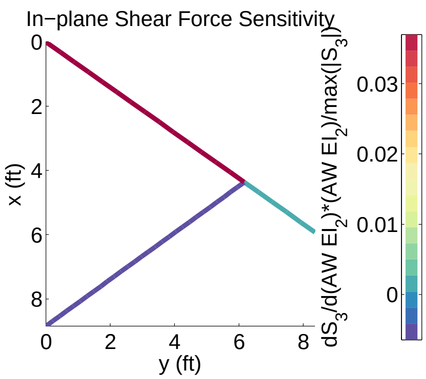

(c) Internal shear sensitivity.

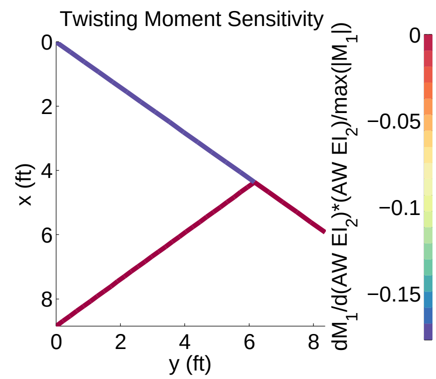

(d) Internal moment sensitivity.

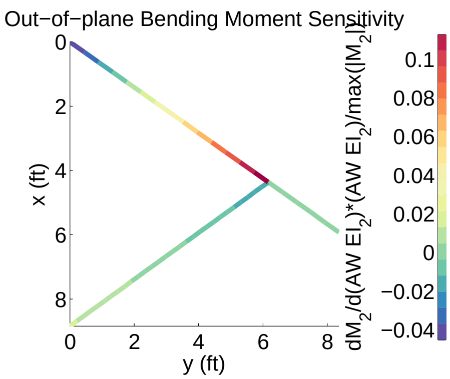

(e) Internal moment sensitivity.

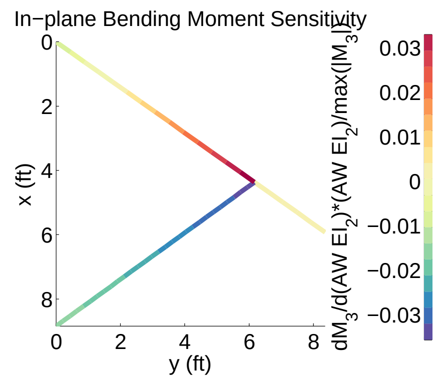

(f) Internal moment sensitivity.

Figure 3.38: Internal generalized force sensitivities to aft wing in-plane bending stiffness.

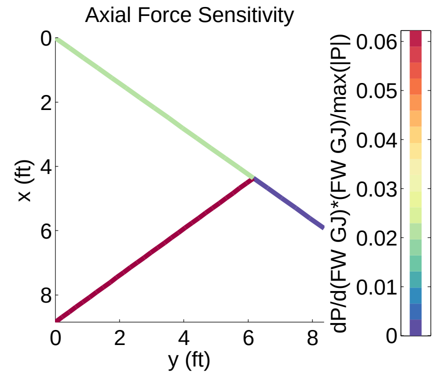

(a) Internal axial force sensitivity.

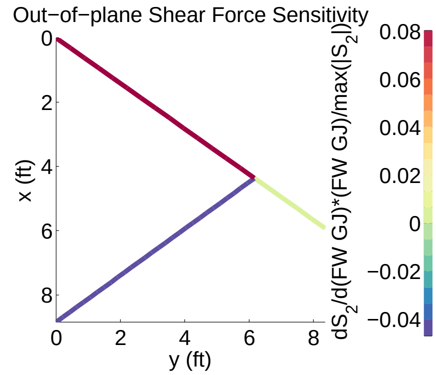

(b) Internal shear sensitivity.

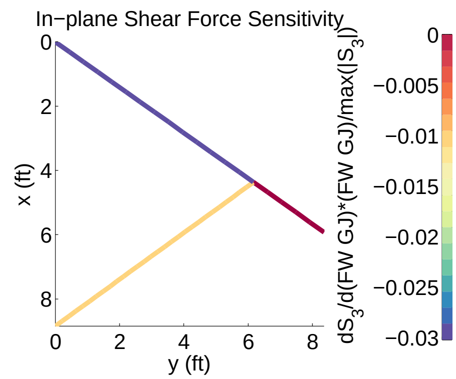

(c) Internal shear sensitivity.

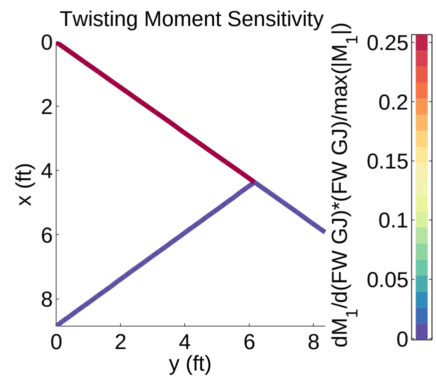

(d) Internal moment sensitivity.

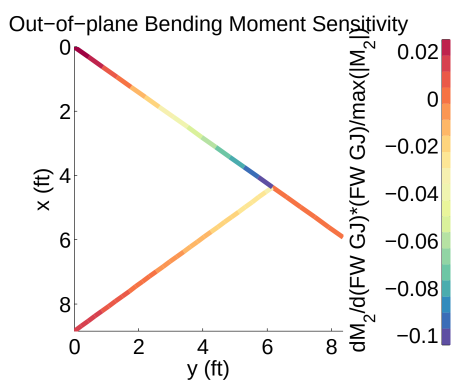

(e) Internal moment sensitivity.

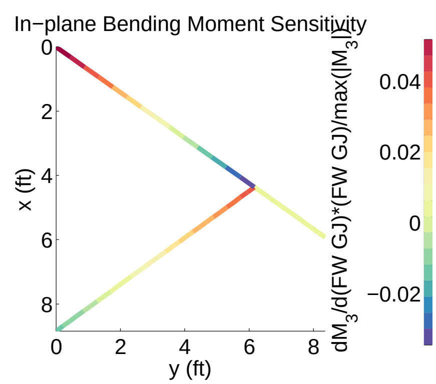

(f) Internal moment sensitivity.

Figure 3.39: Internal generalized force sensitivities to forward wing twist stiffness.

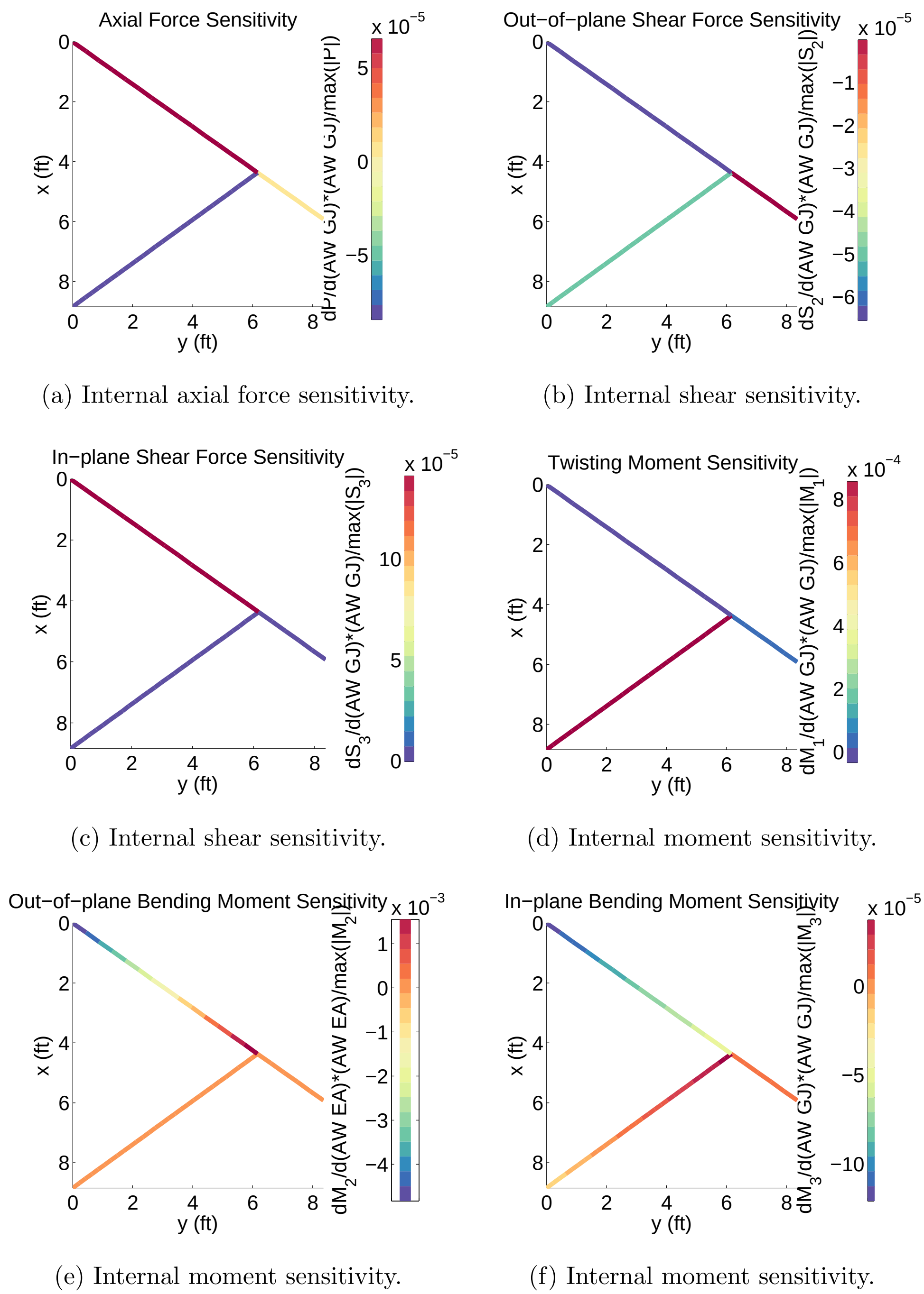

(a) Internal axial force sensitivity.

(b) Internal shear sensitivity.

(c) Internal shear sensitivity.

(d) Internal moment sensitivity.

(e) Internal moment sensitivity.

(f) Internal moment sensitivity.

Figure 3.40: Internal generalized force sensitivities to aft wing twist stiffness.

3.4 Equivalent Static Loads (ESL) Optimization

This section is based on work that is accepted for publication in *Journal of Aircraft* and was awarded best in session at conference [62]. The scaled model is an earlier version of the model described in the Methodology chapter. Direct comparison to other results is omitted due to model differences.

As a first step, a baseline scaled model was designed using a modern approach intended for linear aeroelastic scaling. The design provides a favorable initial design and a control for evaluating the modified method. The scaled model was designed such that the first seven scaled natural frequencies and mode shapes match the target model [14]. The objective function of the optimization was to minimize the difference of the mode shapes. The reduced frequencies were constrained to match within 3%. The scaled wing mass was constrained to match the target value within 2%.

A second scaled model was designed using a modern approach for that was modified for nonlinear aeroelastic scaling. The optimization matched

1. nonlinear static response to scaled target $2.5g$ aeroelastic trim loads,
2. linear static response to scaled target $2.5g$ aeroelastic trim loads,
3. first four reduced frequencies within 3% of the target reduced frequencies, and
4. scaled wing mass within 2% of the target wing mass.

The optimization for this section used modal identification and mode tracking, but did not include a global search. Better local optima could exist. Future work should fortify the results with a global search.

3.4.1 Baseline Modern Approach for Linear Aeroelastic Scaling

Optimized design variables of the baseline vehicle are listed in Table A.5. Weight breakdown of the design is compared to the weights of the full-scale vehicle in Table A.6. The total vehicle weight and total wing weight match the scaled target values within the prescribed 2%. The ratio of structural to nonstructural weight is higher in the scaled vehicle than the full-scale design. This indicates that the ladder structure is a less efficient structural layout than the target wingbox configuration. Lower structural efficiency is not an issue in this case. However, full-scale vehicles with little or no nonstructural mass would require an aeroelastically scaled vehicle to have a structure with equal or greater efficiency.

Nondimensional modal frequencies of the design are compared to the target nondimensional modal frequencies in Table A.7. Scaling optimization was constrained such that the first seven nondimensional modal frequencies matched within 3%. This was satisfied except for a slight violation of mode 2 due to variation on error normalization and optimizer tolerances.

Nonlinear static aeroelastic trim results for a $2.5g$ maneuver are compared to the scaled target response in Fig. 3.41. The figure shows structural analysis load steps from zero load to the converged aeroelastic displacements for the forward wing tip and aft wing center. Tip and aft wing displacements are 41% and 33% greater than their target values, respectively. The design using the new method is discussed in the next section.

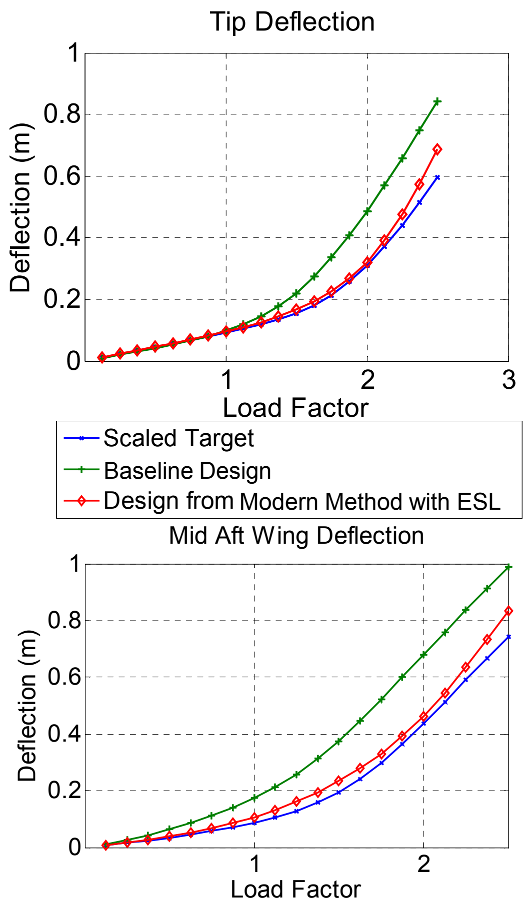

Figure 3.41: Nonlinear aeroelastic trim response in 2.5g maneuver.

Dynamic aeroelastic response of the baseline design linearized about 1g nonlinear aeroelastic trim is shown in Fig. 3.42. A traditional dynamic analysis, with stiffness based on the undeformed shape, would show reduced aeroelastic frequencies at zero velocity that matched as well as the normalized structural frequencies. Greater than 3% reduced frequency disagreement at zero velocity (nondimensionalized as Froude number) in Fig. 3.42 is due to considering the stiffness of the structure in the deformed state.

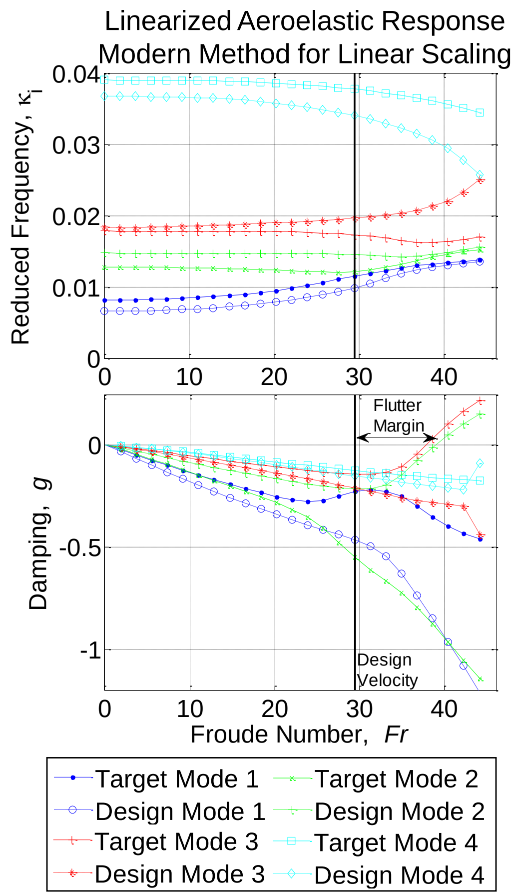

Figure 3.42: Dynamic aeroelastic response linearized about a 1g nonlinear aeroelastic trim. Baseline scaled model compared to the target model.

The design Froude number is indicated by the vertical black line. One measure of design quality is agreement in the value of the most dominant aeroelastic frequencies at the design point. The design has room for improvement. Aeroelastic damping results provide a range of aeroelastic stability. The scaled model's nondimensional flutter speed agrees with the target model. Stability is ensured by a 25% flutter margin. The flutter mode shape, however, is not consistent with the target flutter mode shape. Figure 3.43 shows the flutter mode shape comparison; multiple frames are needed because participation of the modal degrees of freedom are out of phase.

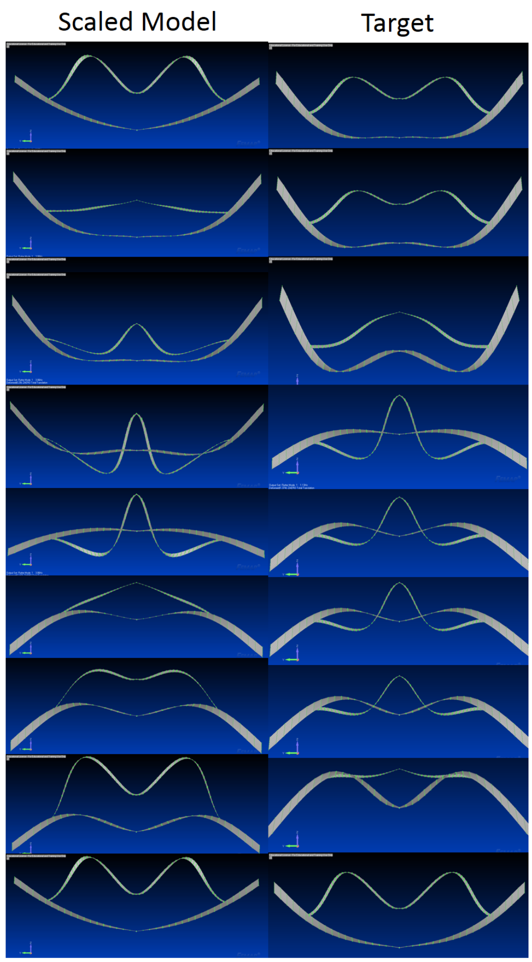

Figure 3.43: Flutter mode shape comparison.

3.4.2 Modified Modern Approach for Nonlinear Aeroelastic Scaling

Design cycle history of the objective function during optimization is shown in Fig. 3.44. Objective values achieved with the linearized approximate model at the end of each design cycle are indicated by blue ◦ symbols, while objective values from the nonlinear analysis are indicated by green × symbols. Convergence is achieved when the optimum equivalent linear response matches the nonlinear response. The design converges in 13 nonlinear iterations.

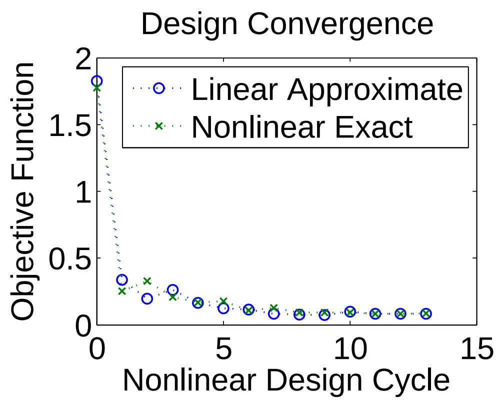

Figure 3.44: Optimization design history.

Optimized design variables are listed in Table A.5. Weight breakdown of the design is compared to the weights of the full-scale vehicle and baseline vehicle in Table A.6. The total vehicle weight and total wing weight match the scaled target values within the prescribed 2%. Scaled structural weight is higher than both the target model and baseline model.

Normalized modal frequencies are compared to the target and baseline scaled model normalized modal frequencies in Table A.7. Scaling optimization was constrained such that the first four reduced modal frequencies matched within 3%. The constraints are satisfied. The remaining tabulated frequencies have reasonably low error, except for mode 7 which is 20% lower than the target value.

Nonlinear static aeroelastic trim results for a $2.5g$ maneuver are compared to the target and baseline scaled model in Fig. 3.41. The response is considerably more agreeable throughout the load step range than the scaled model designed without static displacement matching. Tip and mid aft wing displacement errors are reduced to 15% and 12%, respectively at $2.5g$.

Dynamic aeroelastic response linearized about $1g$ nonlinear aeroelastic trim is shown in Fig. 3.45. Agreement in the aeroelastic frequencies at and below the design velocity is noticeably better than the results for the scaled model designed without static displacement matching, in Fig. 3.42. Flutter onset occurs at a higher nondimensional velocity than the target model, and the flutter mode shapes do not match (the flutter mode shape plot is omitted).

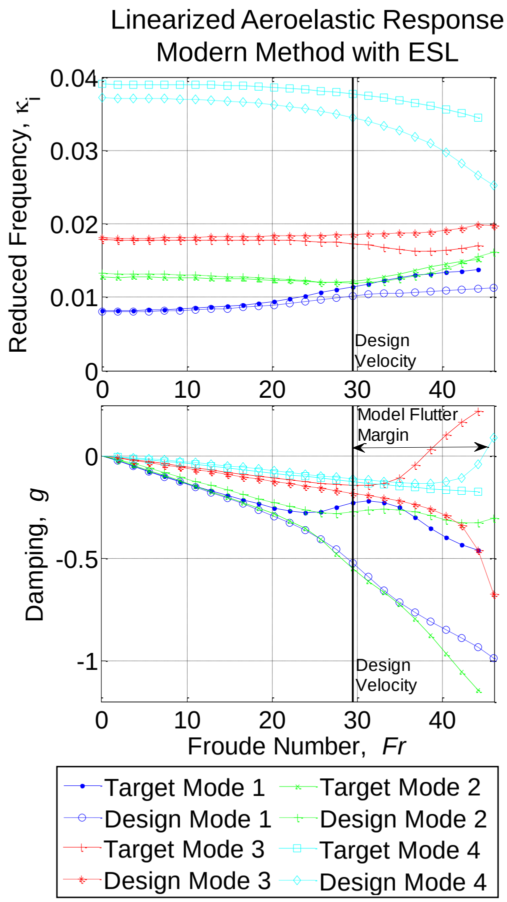

Figure 3.45: Dynamic aeroelastic response linearized about a 1g nonlinear aeroelastic trim. Model designed using the new nonlinear method compared to the target model.

3.4.3 ESL Optimization Discussion

Results presented in the Section 3.2 indicate that aircraft with typical transverse to axial stiffness ratios will not require nonlinear static response matching for stiffness design. Results in the Section 3.2 also showed that the stiffness matching performance of the modified design process presented in Section 3.4 can be preserved by retaining the linear static response matching while neglecting matching of the nonlinear static response. Failure constraints, however, may require the scaled model optimization to consider nonlinear static response. Aircraft with unconventionally low transverse to axial stiffness ratios may benefit more from nonlinear static response matching for stiffness design. If used, the methodology of Section 3.4 should be modified to include global search optimization.

3.5 Multiple Optima

Previous work on aeroelastic scaled model optimization has not addressed certain local optima that may be encountered. Three design nonlinearities that can lead to design complications and local optima are discussed is this section.

3.5.1 Mode Swapping and Mixing

Mode swapping can lead to ill-posed optimization problems [14]. Eigenpairs are typically numbered by the magnitude of their eigenvalues. Mode swapping occurs when physical eigenvector mode shapes have corresponding eigenvalues that are in a different eigenvalue magnitude order than the target model. The optimization problem is ill-posed if modal frequencies of swapped modes are constrained to their swapped order. An example is illustrated in Fig. 3.46. Two local optimum designs are shown from an optimization problem that included the first two vibration eigenpairs. Design B is ill-posed.

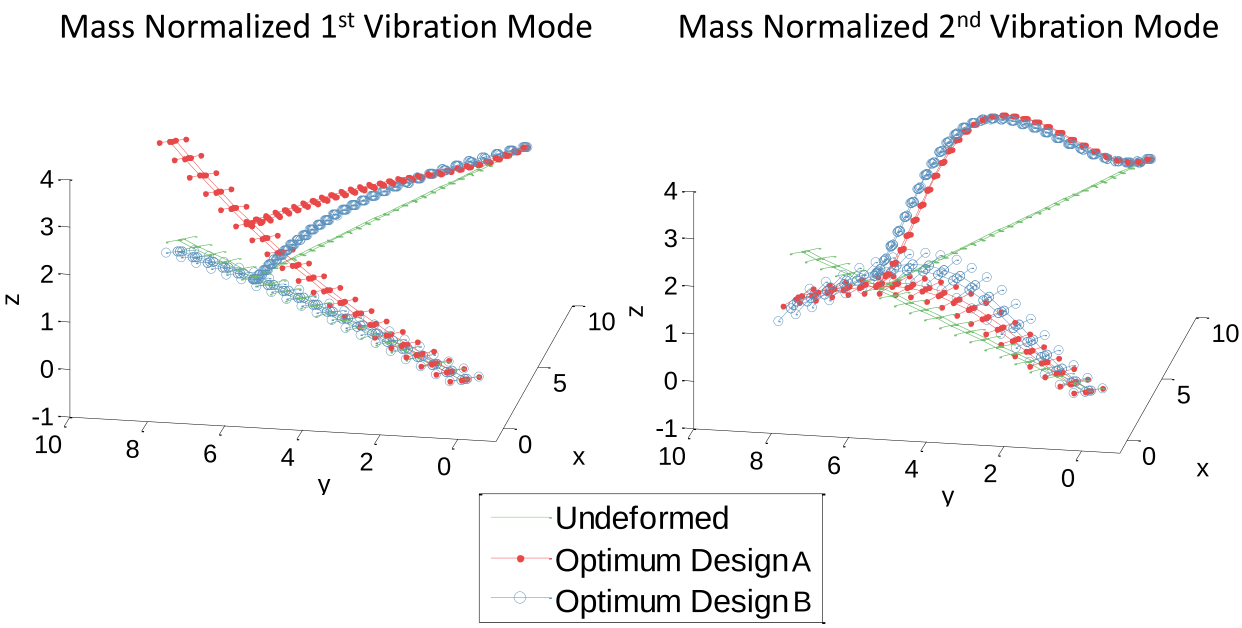

Figure 3.46: Comparison of multiple optima.

The first two eigenvector mode shapes of Design A have the same physical characteristics as the target model. Mode one is primarily forward wing first bending and mode two is forward wing second bending with aft wing first clamped bending. The first mode, numbered by eigenvalue magnitude order, of Design B is primarily aft wing in-plane bending. The optimizer has enforced a modal frequency constraint on the corresponding eigenvalue, which keeps the design stuck in an ill-posed local optimum.

The mode swapping issue can be eliminated by changing eigenpair numbering from eigenvalue magnitude order to target eigenvector mode shape order. Eigenpairs of the initial design are numbered based on physical eigenvector shape and tracked during the optimization. Cross-orthogonality check between the current design cycle and the previous cycles is used to track the mode shape order [23, 24].

One issue that is not addressed in previous scaling work is the difficulty of numbering the mode shapes of the initial design, and the problems of mode shape *mixing*. The initial numbering can be automated with a cross-orthogonality check between the initial design and the target mode shapes, or by human judgment. The initial numbering can be difficult or impossible when there is mode shape mixing. Mode shape mixing occurs when physical characteristics of the initial mode shapes have mixed compatibility with the target mode shapes. Consider the following hypothetical example: a target model results show the

- fifth mode is a combination of forward wing third bending and aft wing second twist and the
- sixth mode is a combination of forward wing second bending and aft wing third twist

while an initial scaled model design results show the

- fifth mode is a combination of forward wing second bending and aft wing second twist and the
- sixth mode is a combination of forward wing third bending and aft wing third twist.

The initial mode shape order is unclear for this example. This predicament becomes more likely as the number of eigenpairs in the optimization is increased. Global optimization may be required to handle cases with initial mode mixing. The global objective function will be higher in areas of mode mixing, which should point the optimizer to unmixed areas of the design space.

3.5.2 Close to Underdetermined Design Problem

Easier-to-satisfy weighted objective functions, such as matching only one vibration mode shape, coupled with many design variables may lead to a close to underdetermined problem. In these cases, drastically different designs may have close to the same value of the objective function. Two local optimum designs from a close to underdetermined case are shown in Fig. 3.47. The optimization matched only the first vibration eigenpair. The first vibration mode shapes are very similar and close to the target shape (as indicated buy the small weighted objective function values in Table 3.12). The designs are very different, and the static responses to scaled trim loads are vastly different.

For the problem studied, close to underdetermined optimization cases tended to produce poor scaled model designs (i.e., matching only one or two vibration eigenpairs and nothing else is not enough). The additional terms needed for better quality scaled model designs tend to reduce the underdetermined nature of the optimization.

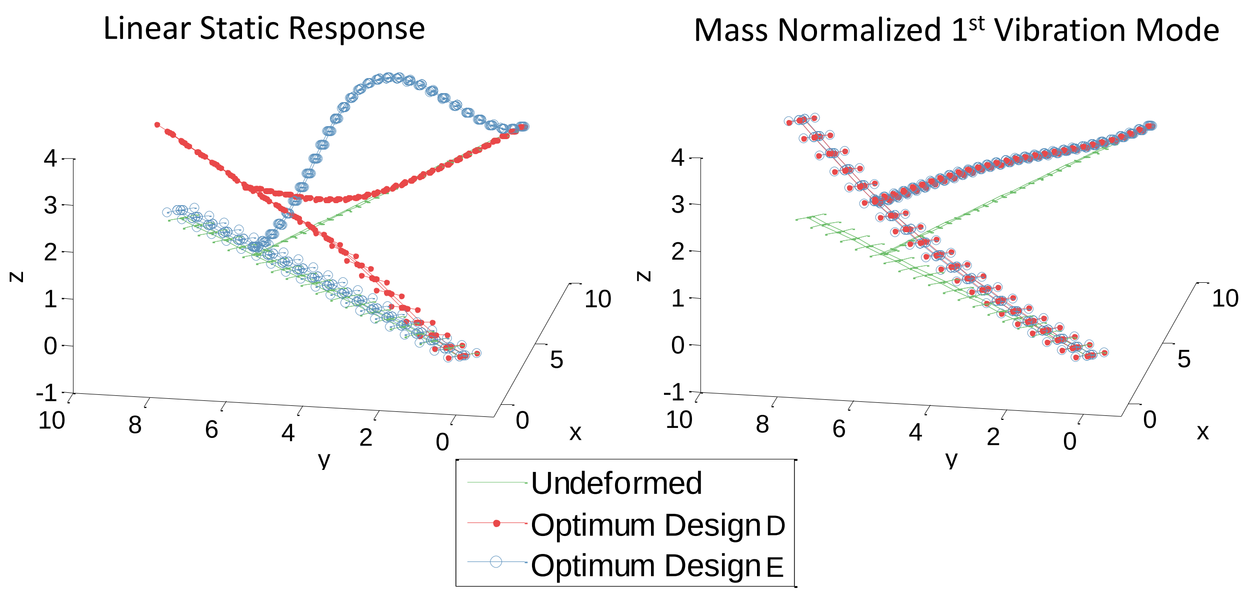

Figure 3.47: Comparison of multiple optima.

Table 3.12: Design Comparison

	Design D	Design E
Obj. Fun.	0.0947	0.1008
ω_1 (Hz)	1.8639	1.8639
d_1	0.0380	0.0427
d_2	0.1099	0.1094
d_3	0.1044	0.0595
d_4	0	0.0374
d_5	0	0
d_6	0.0363	0.0150
d_7	0.0176	0.0162
d_8	0.0082	0.0086
d_9	0.0000	0
d_{10}	0.0055	0

3.5.3 Nonlinear Objective Function Response W.R.T. Design Variables

Another source of local optima is the nonlinear objective function. It's possible that there are local optima that are close to the global optima. Figure 3.48 shows the response of two local opitmum designs that were optimized to match the first two target vibration eigenpairs. The first two vibration mode shapes match closely, but not exactly. The objective function values are shown in Table 3.13. Although both are qualitatively good, design one has a 40% lower objective function than design two. The designs are slightly different, but not drastically different.

Table 3.13: Design Comparison

	Design A	Design C
Obj. Fun.	0.1152	0.1622
ω_1 (Hz)	1.8400	1.8639
ω_2 (Hz)	3.3942	3.3942
d_1	0.0406	0.0400
d_2	0.1045	0.1090
d_3	0.0430	0.0534
d_4	0	0
d_5	0.0183	0.0164
d_6	0.0235	0.0359
d_7	0.0341	0.0096
d_8	0.0068	0.0433
d_9	0.0000	0
d_{10}	0.0022	0.0005

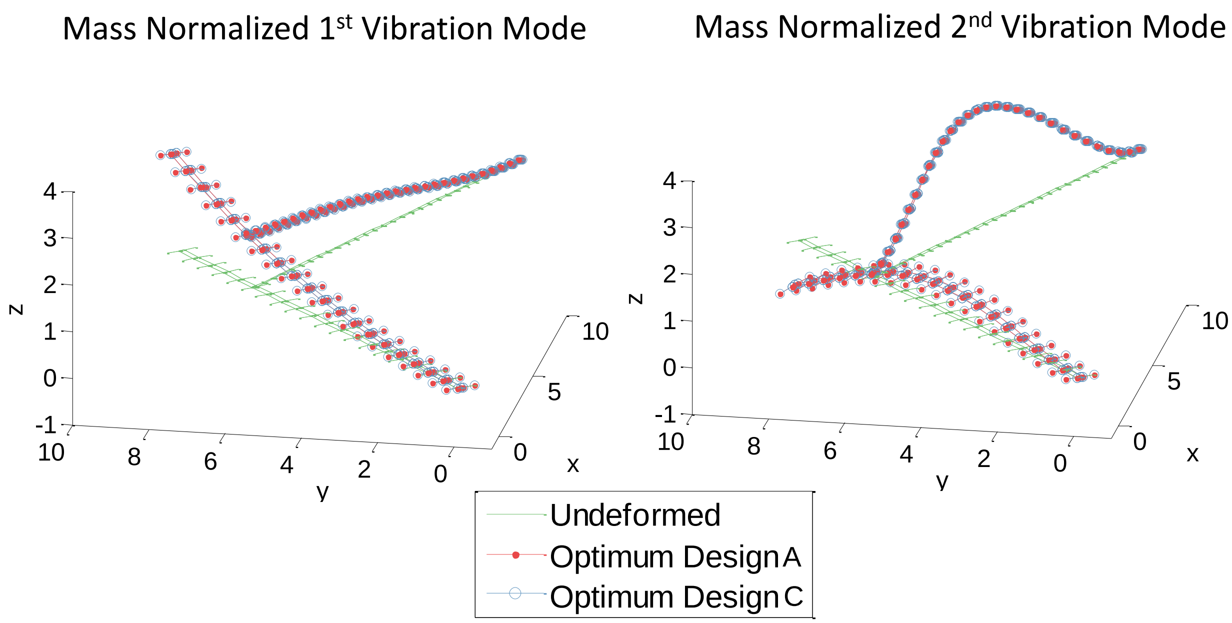

Figure 3.48: Comparison of multiple optima.

Chapter 4

Conclusions and Future Work

This dissertation aimed to address methodology needs for aeroelastic scaling of aircraft with geometrically nonlinear behavior. Classical and modern approaches to aeroelastic scaling were reviewed. The review identified potentially unsound assumptions in the scaling methodologies, which were originally developed for geometrically linear applications. Omission of stiffnesses (e.g., axial stiffness) from classical aeroelastic analysis and truncation of higher-frequency modal degrees of freedom from the modern scaling optimization may lead to designs that do not correctly capture the nonlinear kinematic effects. More specifically, the omissions may lead to differences in internal forces between the target and scaled model. The differences would result in inconsistent internal force-stiffness coupling.

Theory was developed for a modern aeroelastic scaling approach by first nondimensionalizing the dynamic aeroelastic equation of motion. Aerodynamic scaling was accomplished by analytically matching the scaled flight condition through selection of the test altitude and velocity and scaling the outer model line (OML). The structural properties could not realistically be matched analytically. Partial global similitude was achieved by optimization of a truncated number of vibration eigenpairs (which correspond to nondimensional parameters from the modern scaling theory) so that they matched the scaled target values. Compatibility of the discretized models was possible through selection of a compatible subset of degrees of freedom. This work modifies the modern scaling approach to include matching of buckling eigenpairs and static responses to supplement losses from truncated information.

A systematic approach was examined that optimized different numbers of vibration eigenpairs, buckling eigenpairs, and optionally linear statics. For a joined-wing demonstration problem, matching three vibration eigenpairs and the linear static response to scaled $2.5g$ target aeroelastic loads produced the best scaled model designs. Addition of buckling eigenpair matching in the scaled model optimization did not substantively change the design quality when linear statics matching was already included. Greater or fewer than three vibration eigenpairs in the optimization slightly reduced the quality of the scaled model designs for this case. The quality of the designs reduced significantly when linear statics matching was omitted from the optimization. It is implicit that the linear statics matching provides scaled models with superior on-design responses (i.e., response to expected aeroelastic loads); cases in this demonstration also showed improvements in linear and linearized dynamic response and flutter speed when linear statics matching was included in the optimization.

The insignificance of the buckling eigenpair matching was a counterintuitive result for this demonstration problem, which had an indeterminate structure and geometrically nonlinear response. An internal-loads sensitivity study was performed to explain the counterintuitive results. The analytical solution to an indeterminate two-beam frame example was used to show that internal loads, though dependent on the stiffnesses, can be insensitive to changes in the stiffnesses for certain cases. A sensitivity analysis of a target-equivalent model for the three-dimensional joined-wing demonstration case showed that the internal loads are insensitive to the axial stiffnesses of the structure. Future scaling efforts for geometrically nonlinear problems with indeterminate load paths should estimate the nondimensional characteristic transverse to axial stiffness ratio, $\frac{EI}{EAL^2}$, of target structure members and use Eq. (3.2) to approximate the possible changes in internal forces as $\frac{EI}{EAL^2} \to 0$. If the transverse to axial stiffness ratio is sufficiently low, scaled model optimization should be attempted with linear static response matching and vibration eigenpair matching, as described in the Methodology chapter.

Cross-sectional analysis was used to determine the beam stiffness properties of the best scaled-model design and the target joined-wing model. Results showed that scaled out-of-plane bending stiffnesses and torsional stiffnesses of both the forward and aft wings of the scaled model matched the target model. Wing-plane bending stiffness matched for the forward wing but not the aft wing. Scaled axial stiffnesses did not match. The results indicated that a classical aeroelastic scaling approach that neglected the axial stiffness and wing-plane bending stiffness of the aft wing could be used to design a quality scaled model for the demonstration problem.

Simultaneous matching optimization of four vibration eigenvalues, a linear static response, and a nonlinear static response to scaled 2.5g target aeroelastic loads was demonstrated for a variation of the joined-wing demonstration model. An equivalent static loads approach (ESL) was used for nonlinear static response matching. This was the first demonstration of ESL optimization that simultaneously included vibration response. The resulting design outperformed a baseline scaled model that was designed omitting the linear and nonlinear static response matching in the optimization. Results for the previously discussed systematic approach indicate that aircraft with typical transverse to axial stiffness ratios will not require nonlinear static response matching for stiffness design. For the demonstrated cases, the stiffness matching performance can be preserved by retaining the linear static response matching while omitting the nonlinear static response matching. Nonlinear statics may be necessary for enforcing failure constraints and may be beneficial for scaling target designs that have unconventionally high transverse to axial stiffness ratios.

Two recommendations of this work pervade beyond geometrically nonlinear applications to any modern aeroelastic scaling problem. First, scaling requirements based on nondimensionalization of the dynamic aeroelastic equation of motion require nondimensional modal masses of the target and scaled model to match. The modal mass matching requirement was not specifically addressed in modern scaling optimization work. This work included the modal mass matching by optimizing the nondimensional mass-normalized vibration eigenvectors to match. The second general recommendation was to address the issues of newly identified local optima. Mode swapping was a previously identified issue that can be avoided by mode identification and mode tracking. This was the first scaling work to point out issues with mode identification in cases of initial mode mixing. Initial mode mixing occurs when vibration mode shapes of the initial scaled model design have physical characteristics that are not identifiable with a single vibration mode shape of the target model, but are rather a combination of features from multiple target eigenvector modes. In addition to mode swapping and mixing, local optima can also result because the objective function is nonlinear with respect to the design variables and because the optimization problem can be close to underdetermined. Previous work in aeroelastic scaling has not addressed these sources of local optima. Additional scaling requirements (e.g., more vibration eigenpairs) should be added if optimization problems are close to underdetermined. A global search was recommended for optimizing the nonlinear objective function and to avoid mode tracking in cases with initial mode mixing.

In the near future, the presented modifications to the modern aeroelastic scaling approach should be tested for scaling a vehicle with an indeterminate load path and an unconventionally high transverse to axial stiffness ratio. The scenario could be tested quickly with a fictitious beam case. Realizing physical concepts with these specific unconventional properties would be challenging.

In the longer term, this work should be applied to design experimental models that can demonstrate aeroelastically-scaled geometrically-nonlinear responses in flight. The scaled models should be used as low-cost platforms for validating analysis tools, and for validation of flight control and load elevation systems. The methodology should be tested on higher fidelity computational models with more complicated structural layouts that include taper, twist, and composite materials. Additional off-design aeroelastic verification should be included in the scaled model evaluation. Additional verification could include nonlinear aeroelastic trim responses at more load factors and different velocities and altitudes. Comparison of nonlinear transient response to atmospheric gust should also be considered in the scaled model verification. Future methodology enhancements should consider using the modal participation of the target model flutter eigenvector to inform weighting the importance of the structural vibration modes in the scaled model optimization.

Bibliography

[1] *ZAERO User's Manual.* ZONA Technology, Inc, 2008.

[2] *ZAERO Version 8.4 Theoretical Manual.* ZONA Technology, Inc., 2008.

[3] *MSC Nastran 2012 - Design Sensitivity and Optimization User's Guide.* MSC.Software Corporation, 2011.

[4] T. Aarons. Development and implementation of a flight test program for a geometrically scaled joined wing sensorcraft remotely piloted vehicle. Master's thesis, Virginia Polytechnic Institute and State University, October 2011.

[5] J. Arora. *Introduction to Optimum Design 3rd edition.* Academic Press, 2011.

[6] O. O. Bendiksen. Transonic flutter prediction. In *Proc. CEAS/AIAA/NVvL International Forum on Structural Dynamics and Aeroelasticity*, 2003.

[7] O. O. Bendiksen. Nonlinear mode interactions and period-tripling flutter in transonic flow. *Journal of Fluids and Structures*, 19:591606, 2004.

[8] O. O. Bendiksen. Transonic limit cycle flutter/lco. In *5th AIAA/ASME/ASCE/AHS/ASC Structures, Structural Dynamics, and Materials Conference, Palm Springs, CA*, number 2004-1694., 2004.

[9] J. Bertin. *Aerodynamics for Engineers 4th Edition*. Prentice Hall, 2001.

[10] S. Bhasin. Nonlinear aerodynamics nonlinear structure interaction for a dynamic aeroelastic analysis of the joined wing configuration. Master's thesis, San Diego State University, 2010.

[11] M. Bhatia, R. K. Kapania, M. van Hoek, and R. Haftka. Structural design of a truss braced wing: Potential and challenges. In *50th AIAA/ASME/ASCE/AHS/ASC Structures, Structural Dynamics, and Materials Conference.*, number AIAA 2009-2147, 2009.

[12] R. L. Bisplinghoff, H. Ashley, and R. L. Halfman. *Aeroelasticity*. Dover Publications, 1996.

[13] M. Blair, R. A. Canfield, and R. W. Roberts. Joined-wing aeroelastic design with geometric nonlinearity. *AIAA Journal of aircraft*, 42(4):832–848, 2005.

[14] V. L. Bond, R. A. Canfield, A. Suleman, and M. Blair. Aeroelastic scaling of a joined wing for nonlinear geometric stiffness. *AIAA Journal*, 50:513–522, March 2012.

[15] P. W. Bridgman. *Dimensional analysis*. Yale University Press, 1922.

[16] E. Buckingham. On physically similar systems; illustrations of the use of dimensional equations. *Phys. Rev.*, 4:345–376, Oct 1914.

[17] E. Carvallo. Sur une similitude dans les fonctions des machines. *Journal de Physique Théorique et Appliquée*, 1(1):209–212, 1892.

[18] C. E. S. Cesnik and E. L. Brown. Modeling of high aspect ratio active flexible wings for roll control. In *43rd AIAA/ASME/ASCE/AHS Structures, Structural Dynamics, and Materials Conferences, Denver, CO*, number 1719, 2002.

[19] C. E. S. Cesnik and E. L. Brown. Active wing warping control of a joined-wing airplane configuration. *Proceedings of the 44 th AIAA/ASME/ASCE/AHS Structures, Structural Dynamics, and Materials Conferences, Norfolk, Virgina, April 7-10, AIAA Paper No. 2003-1715*, 2003.

[20] M. Drela. Integrated simulation model for preliminary aerodynamic, structural, and control-law design of aircraft. In *AIAA/ASME/ASCE/AHS/ASC Structures, Structural Dynamics, and Materials Conference and Exhibit, 40th, St. Louis, MO, Apr. 12-15*, number 1394, 1999.

[21] M. Drela and H. Youngren. Avl 3.30 user primer. Technical report, Massachusetts Institute of Technology, 2010.

[22] C. A. G. Eger, A. P. Ricciardi, R. A. Canfield, and M. J. Patil. Design of a scaled flight test vehicle including linear aeroelastic effects. In *54th AIAA/ASME/ASCE/AHS/ASC Structures, Structural Dynamics, and Materials Conference.*, number AIAA 2013-1563, April 2012.

[23] M. S. Eldred. *Full order eigenpair perturbations with mode tracking applications in aeroelasticity and optimization.* University of Michigan., 1993.

[24] M. S. Eldred, V. B. Venkayya, and W. J. Anderson. Mode tracking issues in structural optimization. *AIAA Journal*, 33:1926–1933, 1995.

[25] C. Farhat, M. Lesoinne, and P. Le Tallec. Load and motion transfer algorithms for fluid/structure interaction problems with non-matching discrete interfaces: Momentum and energy conservation, optimal discretization and application to aeroelasticity. *Computer Methods in Applied Mechanics and Engineering*, 157(12):95 – 114, 1998.

[26] D. E. Finkel. *DIRECT Optimization Algorithm User Guide*. Center for Research in Scientific Computation, North Carolina State University Raleigh, NC 27695-8205, March 2003.

[27] J. B. Fourier. *Théorie analytique de la chaleur*. Paris, 1822.

[28] M. French. An application of structural optimization in wind tunnel model design. In *AIAA/ASME/ASCE/AHS/ASC Structures, Structural Dynamics and Materials Conference, 31 st, Long Beach, CA*, pages 127–134, 1990.

[29] M. French and F. E. Eastep. Aeroelastic model design using parameter identification. *Journal of aircraft*, 33(1):198–202, 1996.

[30] E. H. Friedmann and P. Peretz. Rotary-wing aeroelastic scaling and its implications for adaptive-materials-based actuation. In *1999 Symposium on Smart Structures and Materials*, pages 60–79. International Society for Optics and Photonics, 1999.

[31] P. P. Friedmann, D. Guillot, and E. Presente. Adaptive control of aeroelastic instabilities in transonic flow and its scaling. *Journal of Guidance, Control, and Dynamics*, 20(6):1190–1199, 1997.

[32] F. H. Gern, A. Ko, E. Sulaeman, J. F. Gundlach, R. K. Kapania, and R. T. Haftka. Multidisciplinary design optimization of a transonic commercial transport with strut-braced wing. *Journal of aircraft*, 38(6):1006–1014, 2001.

[33] N. Green, R. A. Canfield, E. Swenson, M. Blair, and W. Yu. Structural optimization of joined-wing beam model with bend/twist coupling using esl. In *50th AIAA/ASME/ASCE/AHS/ASC Structures, Structural Dynamics, and Materials Conference 17th AIAA/ASME/AHS Adaptive Structures Conference 11th AIAA No, Palm Springs, California, May 4-7, 2009*, number AIAA-2009-3644, 2009.

[34] S. Han. A globally convergent method for nonlinear programming. *Journal of optimization theory and applications*, 22(3):297–309, 1977.

[35] R. L. Harder and R. N. Desmarais. Interpolation using surface splines. *Journal of Aircraft*, 9:189–191, 1972.

[36] D. H. Hodges. A Mixed Variational Formulation Based on Exact Intrinsic Equations for Dynamics of Moving Beams. *International Journal of Solids and Structures*, 26(11):1253–1273, 1990.

[37] D. H. Hodges. Geometrically Exact, Intrinsic Theory for Dynamics of Curved and Twisted Anisotropic Beams. *AIAA Journal*, 41(6):1131–1137, 2003.

[38] J. J. Hollkamp, R. W. Gordon, and S. M. Spottswood. Nonlinear modal models for sonic fatigue response prediction: a comparison of methods. *Journal of Sound and Vibration*, 284:11451163, June 2005.

[39] J. W. Strutt (Lord Rayleigh). *The Theory of Sound*. Macmillan, 1877.

[40] Y. I. Kim, G. J. Park, R. M. Kolonay, M. Blair, and R. A. Canfield. Nonlinear response structural optimization of a joined wing using equivalent loads. *AIAA journal*, 46(11):2703–2713, 2008.

[41] Y. I. Kim, G. J. Park, R. M. Kolonay, M. Blair, and R. A. Canfield. Nonlinear dynamic response structural optimization of a joined-wing using equivalent static loads. *Journal of aircraft*, 46(3):821–831, 2009.

[42] H. W. Kuhn and A. W. Tucker. Nonlinear programming. In *Proc. Second Berkeley Symp. on Math. Statist. and Prob.*, pages 481–492. Univ. of Calif. Press, 1951.

[43] H. A. Lee, Y. I. Kim, G. J. Park, R. M. Kolonay, M. Blair, and R. A. Canfield. Structural optimization of a joined wing using equivalent static loads. *Journal of aircraft*, 44(4):1302–1308, 2007.

[44] I. Lee and G. Jung. An efficient algebraic method for the computation of natural frequency and mode shape sensitivities–part ii. multiple natural frequencies. *Computers and Structures*, 62:437–443, 1997.

[45] I. Lee and G. Jung. An efficient algebraic method for the computation of natural frequency and mode shape sensitivities-part i. distinct natural frequencies. *Computers and Structures*, 62:429–435, 1997.

[46] D. J. Lucia. The sensorcraft configurations: A non-linear aeroservoelastic challenge for aviation. In *46 th AIAA/ASME/ASCE/AHS/ASC Structures, Structural Dynamics, and Materials Conference*, number 1943, 2005.

[47] E. O. Macagno. Historico-critical review of dimensional analysis. *Journal of the Franklin Institute*, 292(6):391 – 402, 1971.

[48] W. H. Mason. Applied computational aerodynamics. Technical report, Virginia Tech, 1998.

[49] T. Melin. A vortex lattice matlab implementation for linear aerodynamic wing applications. Master's thesis, Royal Institute of Technology, 2000.

[50] MSC Software Corporation, 2 MacArthur Place Santa Ana, CA 92707 USA. *MSC Nastran 2004 Reference Manual*.

[51] M. Nikbay, L. Oncu, and A. Aysan. Multidisciplinary code coupling for analysis and optimization of aeroelastic systems. *Journal of Aircraft*, 46(10.2514/1.41491):1938–1944, 2009.

[52] M. J. Patil and D. H. Hodges. Flight dynamics of highly flexible flying wings. *Journal of Aircraft*, 43(6), 2006.

[53] P. Pereira, L. Almeida, A. Suleman, V. Bond, R.A. Canfield, and M. Blair. Aeroelastic scaling and optimization of a joined-wing aircraft concept. In *48th AIAA/ASME/ASCE/AHS/ASC Structures, Structural Dynamics, and Materials Conference*, number AIAA-2007-1889, 2007.

[54] D. A. Peters and M. J. Johnson. Finite-state airloads for deformable airfoils on fixed and rotating wings. In *Symposium on Aeroelasticity and Fluid/Structure Interaction, Proceedings of the Winter Annual Meeting*. ASME, 1994.

[55] D. A. Peters, S. Karunamoorthy, and W. M. Cao. Finite state induced flow models; Part I: Two-dimensional thin airfoil. *Journal of Aircraft*, 32(2), 1995.

[56] A. S. Pototzky. Scaling laws applied to a modal formulation of the aeroservoelastic equations. In *43rd AIAA Structures, Structural Dynamics, and Materials Conference, Denver, Colorado*, number 2002-1598, 2002.

[57] M. J. D. Powell. Algorithms for nonlinear constraints that use lagrangian functions. *Mathematical programming*, 14(1):224–248, 1978.

[58] E. H. Presente. *Innovative scaling laws for aeroelastic and aeroservoelastic problems in compressible flow*. University of California, Los Angeles, 1999.

[59] E. H. Presente and P. P. Friedmann. Aeroservoelasticity in compressible flow and aeroelastic scaling considerations. In *International Symposium on Fluid-Structure Interactions, Aeroelasticity, Flow-Induced Vibration and Noise, 4 th, Dallas, TX*, pages 105–119, 1997.

[60] E. H. Presente and P. P. Friedmann. Aeroservoelasticity in subsonic flow and associated scaling laws. In *AIAA/ASME/ASCE/AHS/ASC Structures, Structural Dynamics, and Materials Conference, Kissimmee, FL*, number AIAA-1997-1079, 1997.

[61] E. H. Presente and P. P. Friedmann. Aeroservoelasticity in compressible flow and its scaling laws. In *39th AIAA/ASME/ASCE/AHS/ASC Structures, Structural Dynamics, and Materials Conference and Exhibit*, number AIAA-98-1899, 1998.

[62] A. P. Ricciardi, C. A. G. Eger, R. A. Canfield, and M. J. Patil. Nonlinear aeroelastic scaled model optimization using equivalent static loads. In *54th AIAA/ASME/ASCE/AHS/ASC Structures, Structural Dynamics, and Materials Conference*, number AIAA 2013-1785, 2013.

[63] A. P. Ricciardi, C. A. G. Eger, R. A. Canfield, M. J. Patil, and N. Lindsley. High fidelity nonlinear aeroelastic analysis for scaled vehicle design. In *14th AIAA/ISSMO Multidisciplinary Analysis and Optimization Conference*, number AIAA-2012-5624, 2012.

[64] J. Richards, T. Aarons, J. Garnand-Royo, A. Suleman, R. A. Canfield, C. Woolsey, N. Lindsley, and M. Blair. Airworthiness evaluation of a scaled joined-wing aircraft. In *53rd AIAA/ASME/ASCE/AHS/ASC Structures, Structural Dynamics and Materials Conference*, number AIAA-2012-1721, 2012.

[65] J. Richards, T. Aarons, A. Suleman, R. A. Canfield, C. Woolsey, N. Lindsley, and M. Blair. Design for flight test of a scaled joined wing sensorcraft. In *52nd AIAA/ASME/ASCE/AHS/ASC Structures, Structural Dynamics and Materials Conference*, 2011.

[66] J. Richards, J. S. Garnand-Royo, A. P. Ricciardi, A. Suleman, R. A. Canfield, and Woolsey C. A. Design and evaluation of aeroelastically tuned joined-wing sensorcraft

flight test article. In *54th AIAA/ASME/ASCE/AHS/ ASC Structures, Structural Dynamics, and Materials Conference*, 2013.

[67] J. Richards, A. Suleman, R. A. Canfield, and M. Blair. Design of a scaled rpv for investigation of gust response of joined-wing sensorcraft. In *50th AIAA/ASME/ASCE/AHS/ASC Structures, Structural Dynamics, and Materials Conference 4 - 7 May 2009, Palm Springs, California*, number AIAA 2009-2218, 2009.

[68] K. Schittkowski. Nlpql: A fortran subroutine for solving constrained nonlinear programming problems. *Annals of Operations Research*, 5:485–500, 1985.

[69] C. Scruton and N. C. Lambourne. Similarity requirements for flutter model testing. *AGARD Manual on Aeroelasticity*, 4, 1963.

[70] M. Spillman and R. A. Canfield. *sqp.m documentation.* Air Force Institute of Technology, AFIT/ENY, Bldg. 640 2950 Hobson Way WPAFB, OH 45433-7665, June 2011.

[71] K. Svanberg. The method of moving asymptotesa new method for structural optimization. *International Journal for Numerical Methods in Engineering*, 24:359373, 1987.

[72] A. Vaschy. Sur les lois de similitude en physique. In *Annales télégraphiques*, volume 19, pages 25–28, 1892.

[73] A. Vaschy. *Théorie de l'électricité.* Baudry, 1896.

[74] Z. Wan and C. E. S. Cesnik. Geometrically nonlinear aeroelastic scaling for very flexible aircraft. In *54th AIAA/ASME/ASCE/AHS/ASC Structures, Structural Dynamics, and Materials Conference. April*, number AIAA 2013-1894, 2013.

[75] L. S. Wasserman and W. J. Mykytow. Model construction. *AGARD Manual on Aeroelasticity*, 4, 1963.

[76] J. Weber and G. G. Brebner. Low-speed tests on 45-deg sweptback wings, part i: Pressure measurements on wings of aspect ratio 5. In *Reports and memoranda 2882, Aeronautical research council*, 1958.

[77] W. Yu. *VABS Manual for Users*. Analyswift, LLC, 1780 North Research Park Way, Suite 108 North Logan, UT 84341, March 2011.

Appendix A

Additional Results

A.1 Systematic Optimization

Table A.1: Systematic optimization results.

	Static Response			Vibration Modes										Buckling Modes	
Case. Obj. Fun.	Linear Nastran	Linear CoFFe	Nonlinear	1	2	3	4	5	6	7	8	9	10	1	2
0.23028	0.233221	0.23028	0.595433	0.452379	0.1717	0.37944	2.134484	11.47346	0.977701	13.67641	2.646853	0.101793	2.816527	1.306627	133.94645
0.475127	0.273842	0.271974	0.165511	0.203153	0.082769	0.785884	9.279102	53.60743	24.7428	107.2654	231.3292	41.17342	105.12432	1.074819	1.257179
0.495118	0.269656	0.267417	0.152696	0.21772	0.009981	0.304707	6.544996	38.37532	13.20722	125.7097	12.96476	7.029941	807.60326	1.035347	1.159091
0.67379	0.273128	0.271215	0.203358	0.248157	0.011	0.143418	4.586212	15.99679	18.37897	62.33074	9.595975	30.3436	677.9537	0.916727	0.932938
1.491722	0.306351	0.305101	0.543387	0.300518	0.008741	0.237333	0.640029	126.3013	49.51805	18.16924	3.369366	0.147386	6.699889	1.121699	1.28952
2.027334	0.465119	0.46429	1.277384	0.338406	0.010644	0.23592	0.527051	0.451023	1.201728	16.28182	3.38681	0.151676	8.299128	1.147464	1.287188
2.817631	0.598541	0.596189	1.200233	0.358016	0.031417	0.297281	0.468117	0.493499	0.573112	13.19748	3.591317	0.139446	6.958072	1.187682	1.395916
15.974645	1.31782	1.313171	0.543445	0.458589	0.232849	0.726386	1.233149	2.698125	0.276929	9.035447	13.66628	0.259542	3.579815	1.178666	1.523152
18.550475	1.396106	1.388744	0.482222	0.498032	0.015062	0.514144	1.071076	4.229143	0.166606	9.154218	1.51345	0.132091	9.838892	1.299564	1.748452
18.681959	1.388213	1.380405	0.485666	0.497734	0.015613	0.510427	1.072701	4.219941	0.167358	9.151165	1.535719	0.130896	9.728884	1.303255	1.753617
43.173943	1.297123	1.286077	1.082811	0.273674	0.016984	0.538234	3.830007	21.03834	2.464437	9.302027	3.487363	0.13374	0.803063	1.485142	2.241815

Vibration Frequencies										Buckling Eigenvalues	
1	2	3	4	5	6	7	8	9	10	1	2
0.045117	0.053228	0.03036	0.013991	0.035199	0.035953	0.167923	0.054642	0.043181	0.108594	0.03219	0.071415
0.024138	0.043055	0.017737	-0.0351	-0.03053	0.039889	-0.08841	0.003115	-0.10931	-0.085291	0.077133	0.108524
0.019891	0.03	0.01062	-0.03576	-0.02678	0.067099	-0.00372	0.018372	-0.01933	0.108564	0.055134	0.085984
0.018171	0.006293	-0.00822	0.033079	0.01913	0.102695	0.29368	0.004197	0.03728	0.184998	0.012225	0.040683
0.03	0.015937	-0.00432	0.003573	-0.12968	0.153431	0.220853	0.007831	0.018708	0.111168	0.012516	0.047013
0.03	-0.01192	-0.03	-0.02015	-0.01871	0.010774	0.195475	-0.02039	-0.00593	0.095627	-0.03755	-0.001132
0.03	-0.01108	-0.03	-0.0246	-0.02241	0.00772	0.164406	-0.02239	-0.00219	0.095812	-0.0298	0.007631
0.03	0.003429	-0.02211	-0.03	-0.02762	0.012438	0.03	-0.01978	0.020011	0.101621	0.032477	0.069271
0.03	0.001797	-0.01587	-0.03	-0.01128	0.005386	0.03	-0.00425	0.008948	0.112179	0.030397	0.069255
0.03	0.001845	-0.01591	-0.03	-0.01144	0.005441	0.03	-0.0044	0.009084	0.112078	0.0303	0.069211
0.009226	0.023075	-0.00309	-0.03	-0.01673	-0.01136	0.03	0.009521	0.025602	0.03	0.011105	0.055855

Table A.2: Systematic optimization results.

	Static Response			Vibration Modes										Buckling Modes	
Case. Obj. Fun.	Linear Nastran	Linear CoFFe	Nonlinear	1	2	3	4	5	6	7	8	9	10	1	2
0.115165	24.638917	24.654572	56.519693	0.094684	2.905387	2.46238	12.37355	24.46518	13.39799	3172.136	164.6828	6.789095	387.89227	21.55435	32.417521
0.302354	3.339964	3.341915	0.72977	0.109601	0.005564	0.812733	3.973355	21.91063	7.309662	31.70456	4.559385	0.155603	85.387805	4.563976	4.598663
1.000603	76.439147	76.446768	1.145864	0.174687	0.009321	0.118346	17.03973	67.89313	32.23147	76.22047	136.9036	32.50919	1680.6697	29.48745	81.005151
1.377937	18.118449	18.104069	0.711954	0.261754	0.014196	0.246361	0.478292	0.602631	1.022656	15.42685	1108.961	862.3355	700.93397	13.47677	36.981515
1.915847	6.607982	6.586324	0.903217	0.309677	0.059848	0.283811	0.406176	0.318425	0.747569	13.49886	7.914507	0.238211	8.97053	6.729383	15.821832
12.623695	5.504956	5.486798	0.609069	0.329206	0.129194	0.324523	0.390912	0.32012	0.421892	11.72356	7.209842	0.216522	7.242198	5.48236	11.958297
15.248793	33.358411	33.298546	2.838997	0.363102	1.035812	0.685546	1.340354	1.488974	0.2687	7.441207	25.02031	0.83077	1764.9963	11.47738	37.129497
15.701264	33.630704	33.576827	2.874907	0.411628	0.340652	1.382468	0.846373	2.434824	0.522138	7.90309	1.40762	0.51111	9.446353	11.7252	40.174506
41.483962	29.170373	29.117409	2.038734	0.418726	0.267362	1.177206	0.872377	2.716878	0.395738	7.983209	1.467604	0.402164	9.23105	11.55828	38.936053
44.769817	3.310076	3.285855	0.221506	0.254532	0.066868	0.567249	3.663494	21.27939	1.855276	9.109646	3.833769	0.057933	0.795805	1.438802	2.549764

Vibration Frequencies										Buckling Eigenvalues	
1	2	3	4	5	6	7	8	9	10	1	2
-0.03	0.017557	-0.08079	-0.04447	-0.01958	0.043423	-0.05875	-0.0073	0.019084	0.171827	-0.38369	-0.16029
-0.01679	-0.03	-0.07005	-0.08586	-0.08565	-0.01097	0.165343	-0.04509	-0.02925	-0.038027	0.088809	0.180008
0.03	-0.01318	-0.03	0.062848	0.034428	0.115206	0.292626	0.070169	0.057559	0.169822	0.220676	0.334295
0.03	-0.01192	-0.03	-0.02399	-0.02047	0.008646	0.188715	-0.01912	0.040989	0.174855	0.135057	0.224327
0.03	-0.01798	-0.03	-0.02559	-0.0227	0.007584	0.175501	-0.02488	-0.00754	0.093073	0.04831	0.123255
0.03	-0.0176	-0.03	-0.02932	-0.02603	0.006696	0.145934	-0.02693	-0.00401	0.093388	0.058501	0.1264
0.03	-0.00248	-0.01046	-0.03	-0.02128	0.027674	0.03	-0.01664	0.024486	0.106693	0.25041	0.328265
0.03	-0.00543	-0.00609	-0.03	-0.00571	0.019149	0.03	-0.0026	0.011549	0.113873	0.240143	0.320081
0.03	-0.00402	-0.00719	-0.03	-0.00663	0.017515	0.03	-0.0029	0.011658	0.113452	0.223076	0.304545
-0.00912	0.021199	0.004231	-0.03	-0.01158	-0.00131	0.03	0.01268	0.029635	0.03	0.090604	0.129835

Table A.3: Systematic optimization results.

	Static Response			Vibration Modes										Buckling Modes	
Case. Obj. Fun.	Linear Nastran	Linear CoFFe	Nonlinear	1	2	3	4	5	6	7	8	9	10	1	2
1.235576	0.320382	0.318585	0.108252	0.347897	0.161792	0.531114	27.31346	92.29669	35.04611	80.74354	132.3823	18.07989	651.98501	0.569094	0.59104
1.253557	0.306574	0.303875	0.068414	0.348007	0.004541	0.141285	32.04184	67.73728	23.09331	89.12799	136.0576	24.30682	693.91624	0.597134	0.61459
1.393831	0.301349	0.29836	0.08419	0.333773	0.005685	0.132675	20.6289	72.59255	31.42951	79.85539	130.1856	23.20942	700.63653	0.623338	0.635972
2.57444	0.346568	0.345704	0.256651	0.283699	0.005106	0.221807	0.711711	1.050777	2.264083	21.82881	3.496759	0.114057	6.208171	1.006413	1.109074
3.136267	0.477551	0.477473	1.004353	0.341602	0.012557	0.234269	0.52447	0.448529	1.246026	16.47828	3.417057	0.148319	8.253113	1.097367	1.204859
3.948535	0.617476	0.615554	0.947542	0.357515	0.037144	0.296654	0.461683	0.474661	0.58578	13.26573	3.667917	0.137289	6.914789	1.119544	1.281424
17.160644	1.257832	1.253335	0.580322	0.460602	0.223344	0.730828	1.239766	2.752351	0.286627	9.030038	13.5577	0.265024	3.590076	1.183753	1.526826
19.770291	1.47752	1.469554	0.4618	0.500295	0.017319	0.526642	1.054106	4.1234	0.163449	9.180789	1.549934	0.134175	9.834722	1.184803	1.57016
19.903782	1.46416	1.45635	0.467279	0.500139	0.017841	0.522113	1.056492	4.117134	0.164122	9.177615	1.573596	0.13283	9.720952	1.18555	1.570271
44.503513	1.374778	1.362524	0.996887	0.272995	0.016604	0.537571	3.819623	21.05454	2.405065	9.306799	3.549572	0.122738	0.800973	1.254509	1.852194

Vibration Frequencies										Buckling Eigenvalues	
1	2	3	4	5	6	7	8	9	10	1	2
-0.02562	-0.02416	-0.03839	0.097542	0.040426	0.099356	0.282307	0.137793	0.038347	0.169355	0.03	0.046716
-0.0243	-0.03	-0.03566	0.07311	0.023485	0.08311	0.199748	0.12449	0.049048	0.151289	0.015238	0.033164
-0.02545	-0.02174	-0.03	0.065875	0.031279	0.109602	0.278385	0.091378	0.055239	0.163	0.026558	0.044796
0.0105	0.005111	-0.01402	-0.00884	-0.00375	0.029633	0.222915	-0.00223	0.007777	0.087756	0.03	0.060025
0.03	-0.01248	-0.03	-0.02017	-0.01888	0.011069	0.197097	-0.02061	-0.00604	0.095287	-0.02669	0.008023
0.03	-0.01144	-0.03	-0.02452	-0.02255	0.008055	0.165674	-0.02263	-0.00203	0.095718	-0.01909	0.01648
0.03	0.003645	-0.02223	-0.03	-0.02767	0.012153	0.03	-0.01971	0.019993	0.101649	0.03	0.067008
0.03	0.001301	-0.01575	-0.03	-0.01107	0.005735	0.03	-0.00429	0.009	0.112263	0.028948	0.066294
0.03	0.001359	-0.01581	-0.03	-0.01124	0.005779	0.03	-0.00444	0.009143	0.112161	0.028605	0.065979
0.005156	0.02278	-0.00268	-0.03	-0.01631	-0.01064	0.03	-0.05775	0.088133	0.03	0.010977	0.052579

Vibration Eigenpairs – 2, With Linear Static Matching

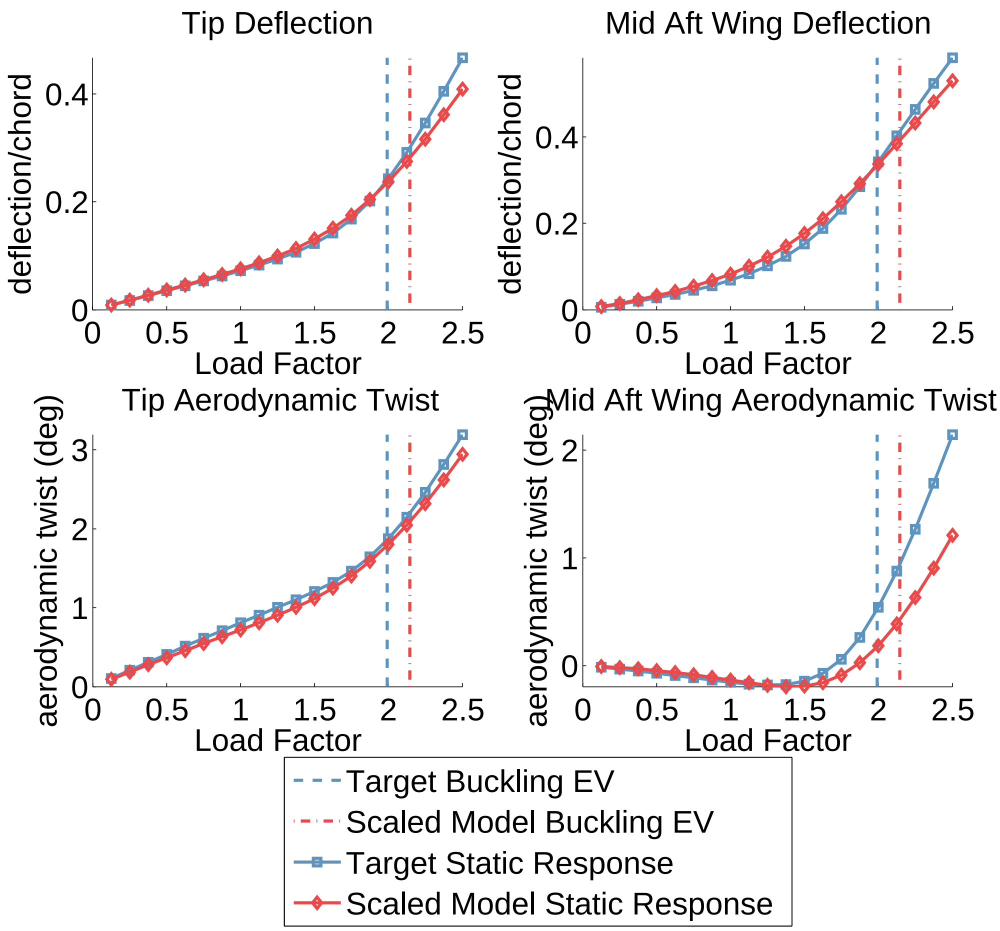

Figure A.1: Response to 2.5 nonlinear aeroelastic trim loads.

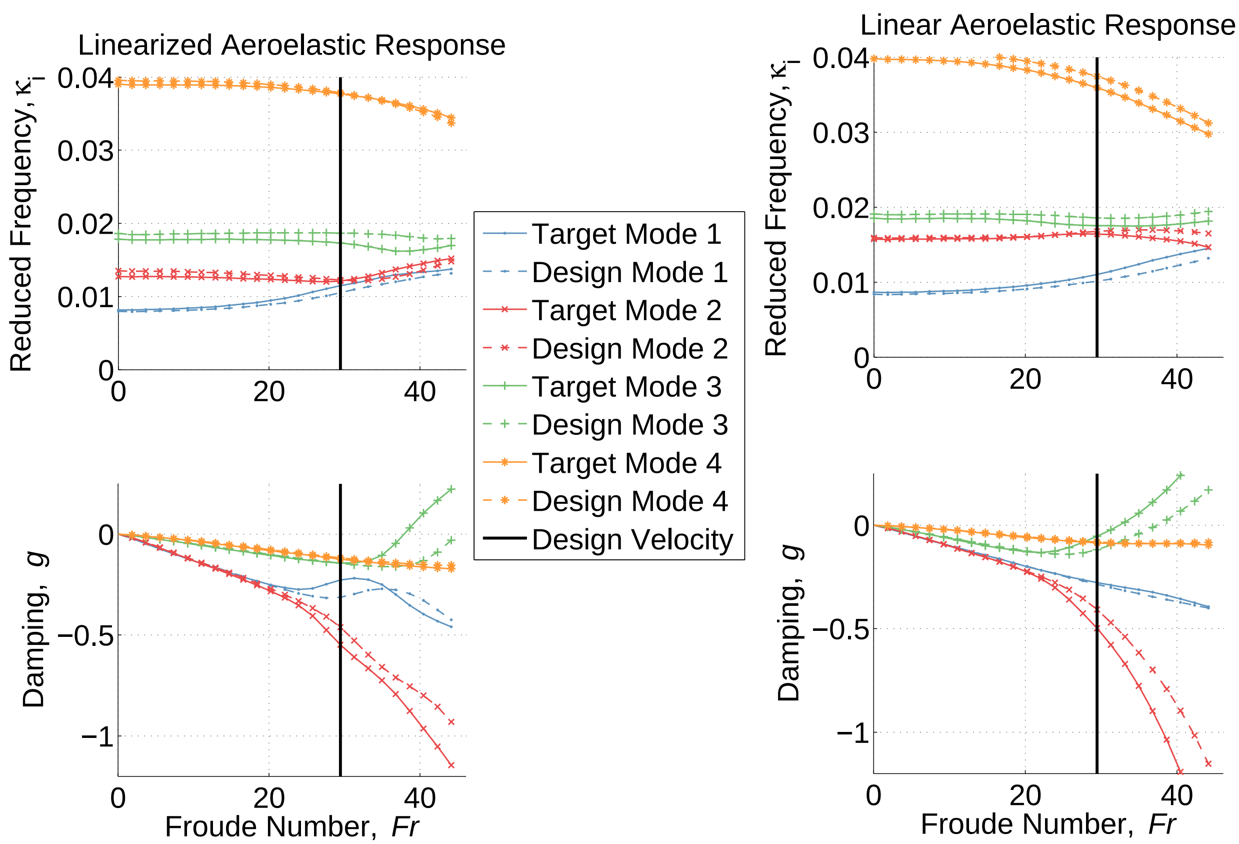

(a) Stiffness linearized about $1g$ nonlinear trim. (b) Undeformed stiffness.

Figure A.2: Dynamic aeroelastic response.

Vibration Eigenpairs – 6, With Linear Static Matching

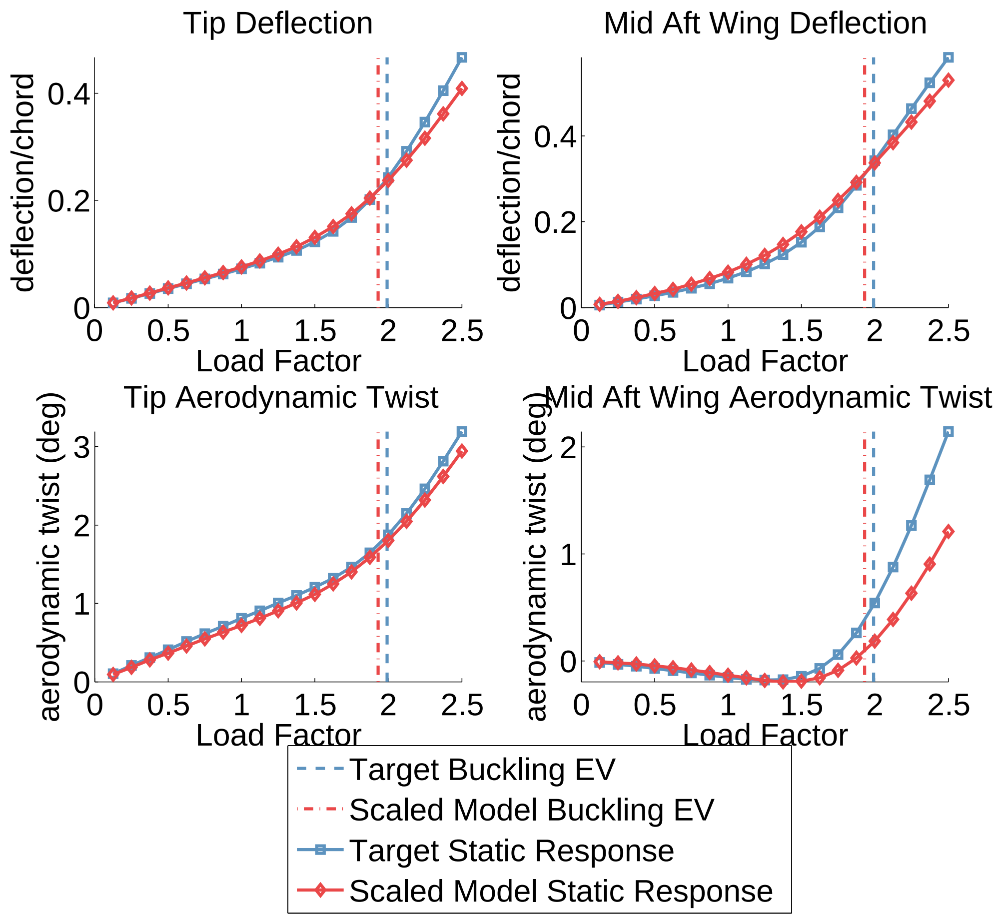

Figure A.3: Response to 2.5 nonlinear aeroelastic trim loads.

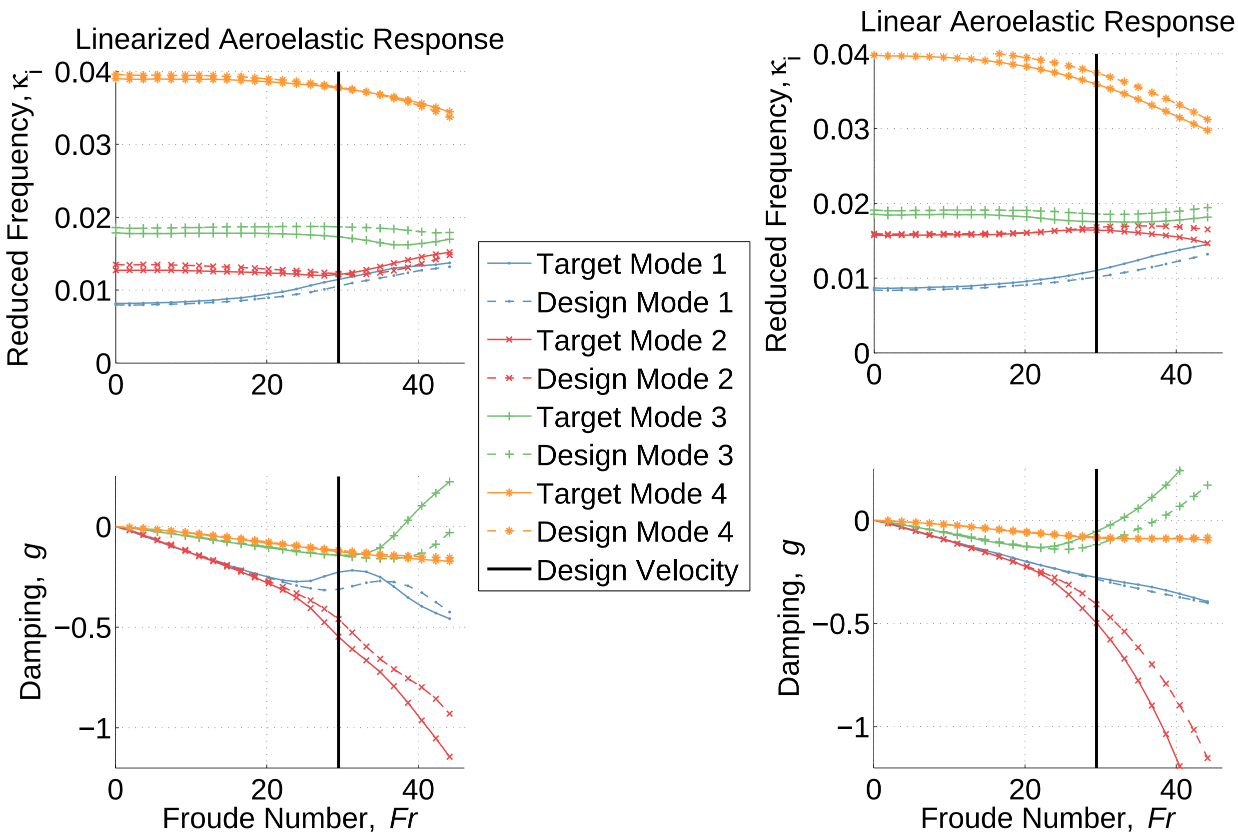

(a) Stiffness linearized about $1g$ nonlinear trim.

(b) Undeformed stiffness.

Figure A.4: Dynamic aeroelastic response.

Vibration Eigenpairs – 9, With Linear Static Matching

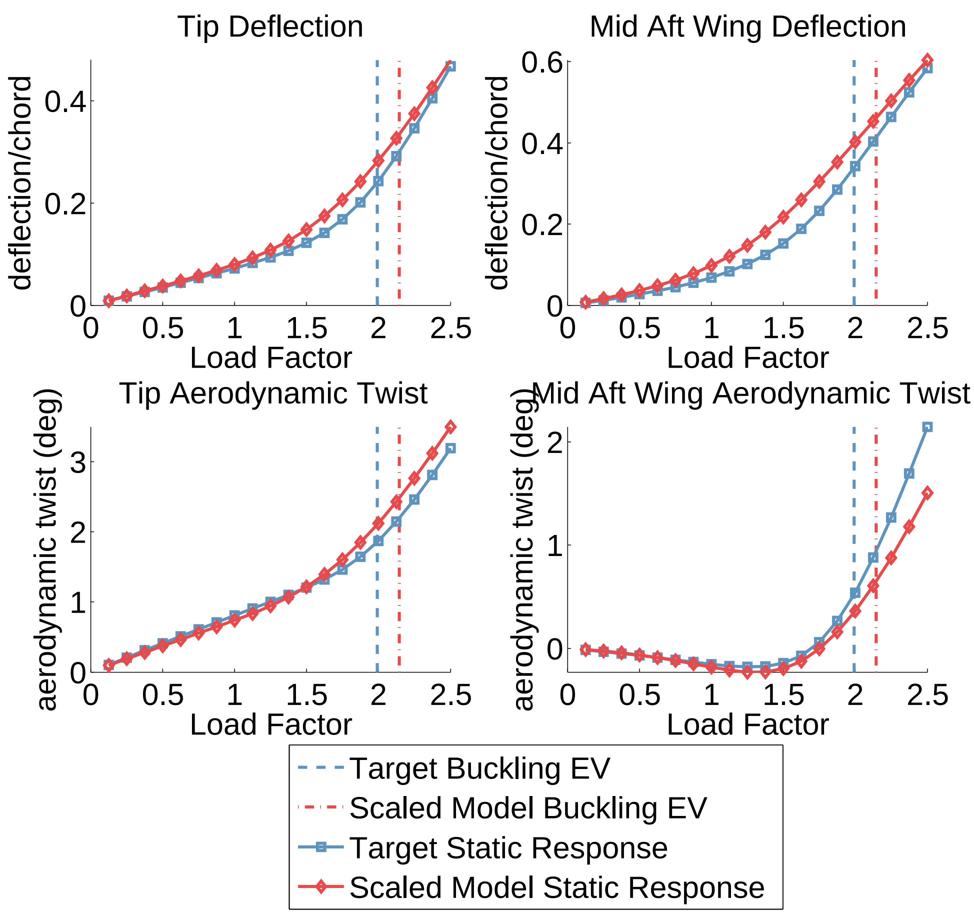

Figure A.5: Response to 2.5 nonlinear aeroelastic trim loads.

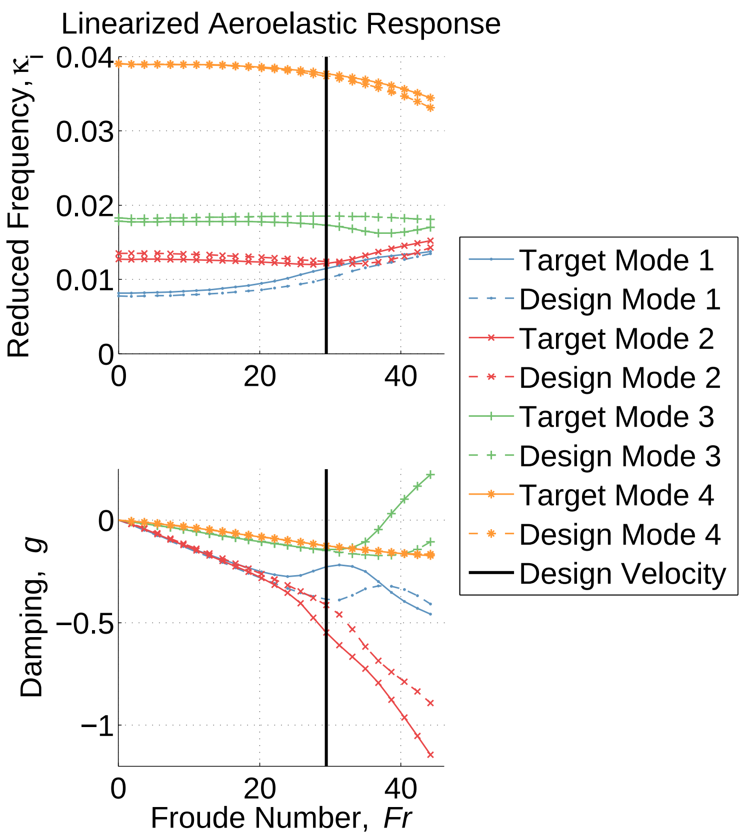

(a) Stiffness linearized about $1g$ nonlinear trim.

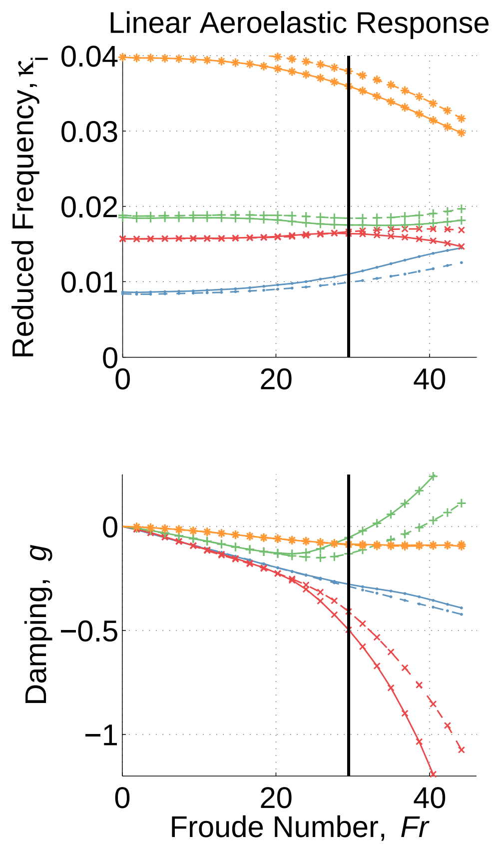

(b) Undeformed stiffness.

Figure A.6: Dynamic aeroelastic response.

Vibration Eigenpairs – 3, Without Linear Static Matching

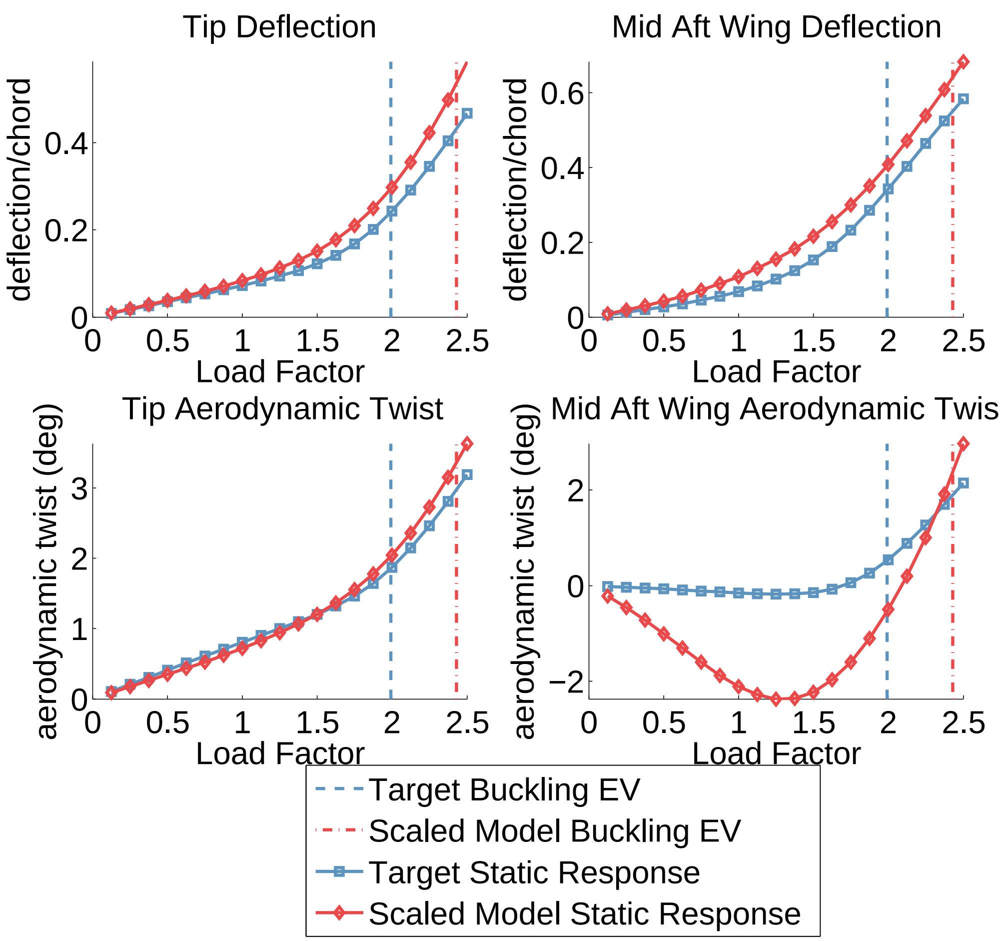

Figure A.7: Response to 2.5 nonlinear aeroelastic trim loads.

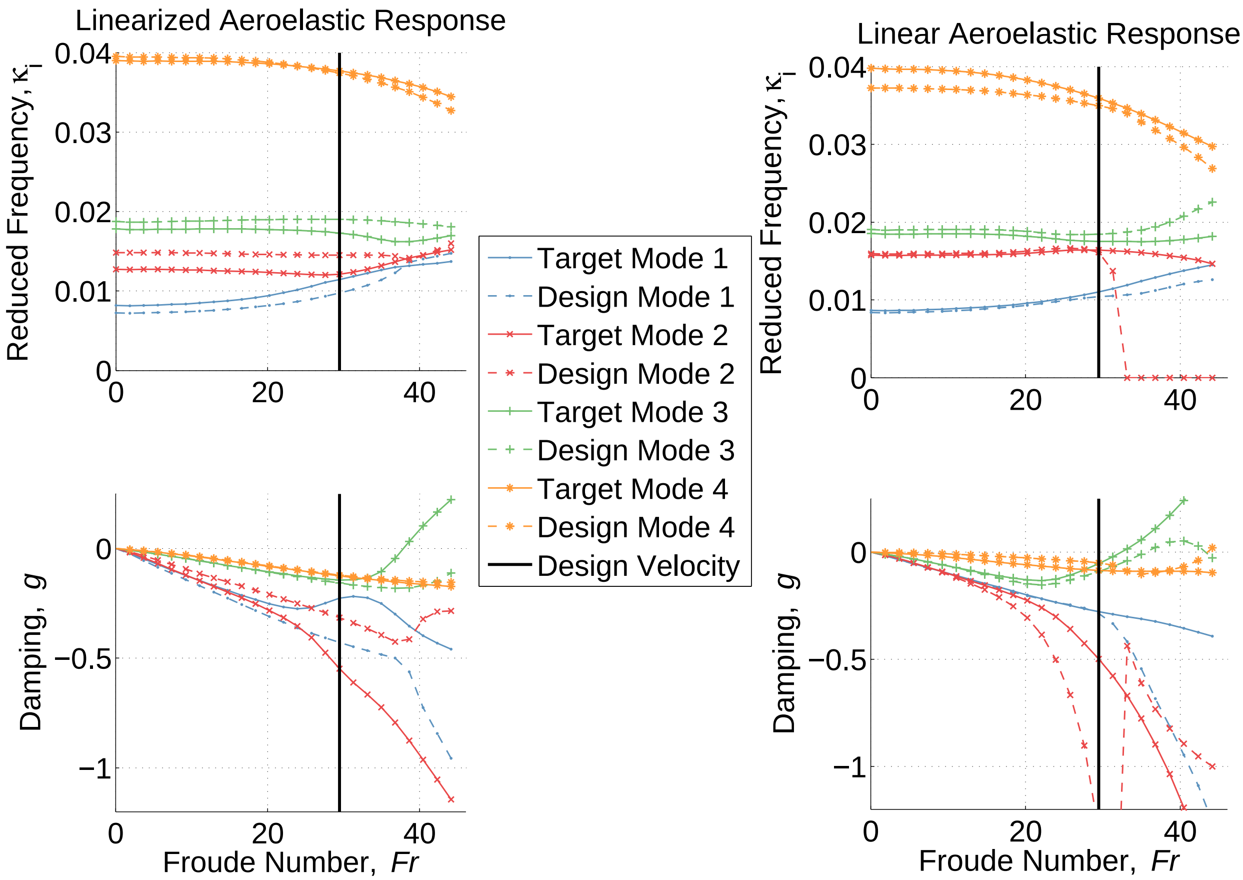

(a) Stiffness linearized about $1g$ nonlinear trim.

(b) Undeformed stiffness.

Figure A.8: Dynamic aeroelastic response.

Vibration Eigenpairs – 6, Without Linear Static Matching

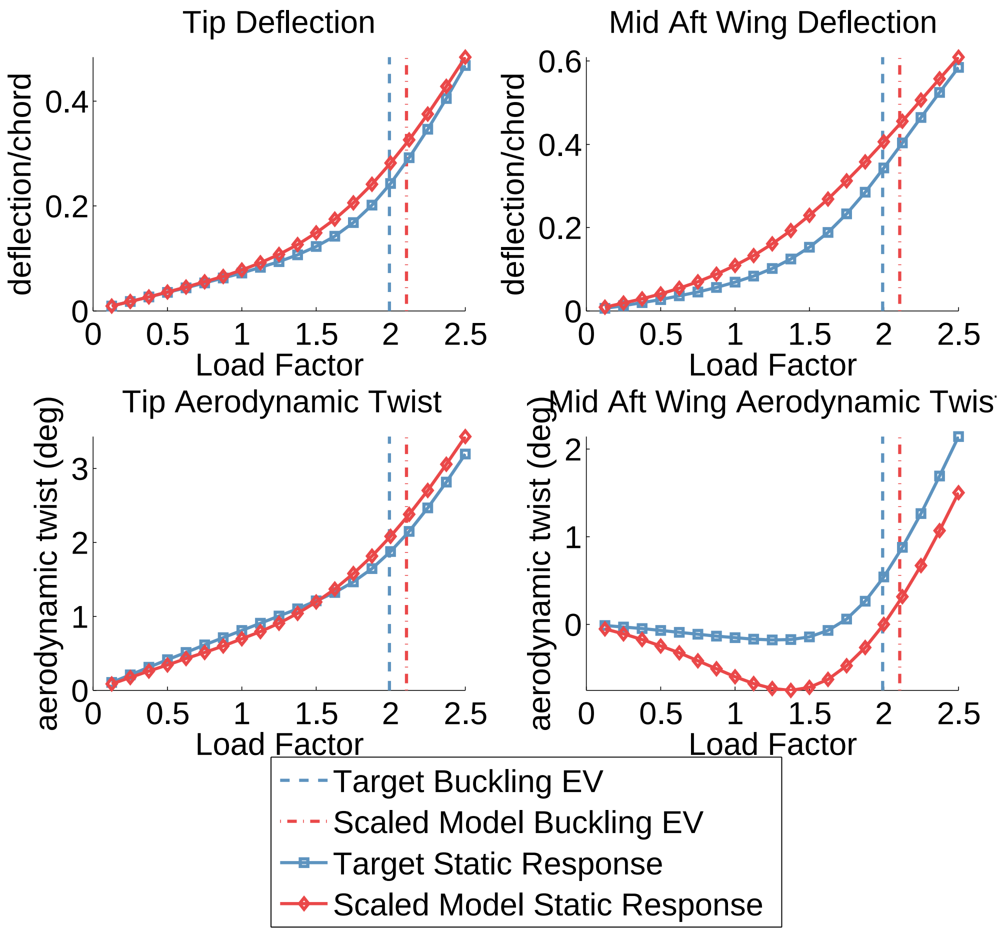

Figure A.9: Response to 2.5 nonlinear aeroelastic trim loads.

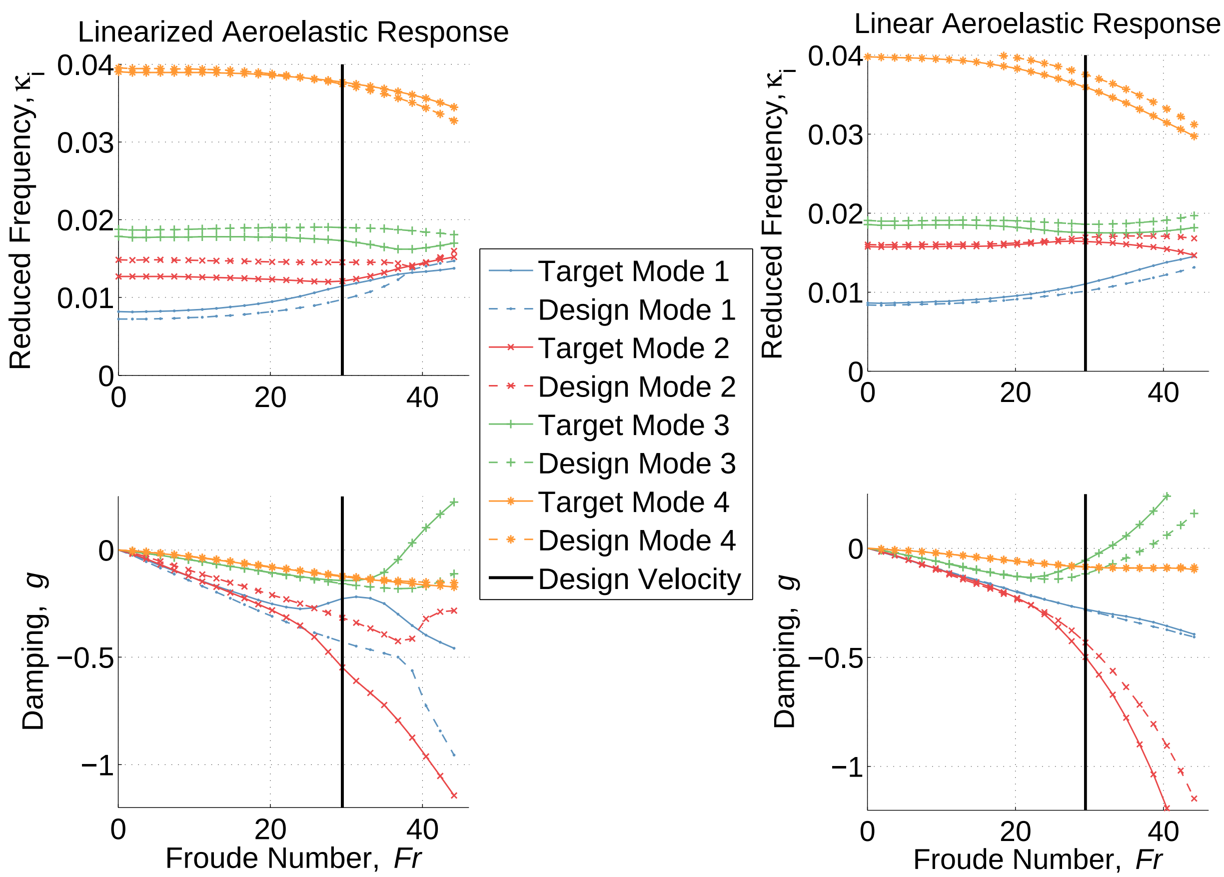

(a) Stiffness linearized about $1g$ nonlinear trim.

(b) Undeformed stiffness.

Figure A.10: Dynamic aeroelastic response.

Vibration Eigenpairs – 10, Without Linear Static Matching

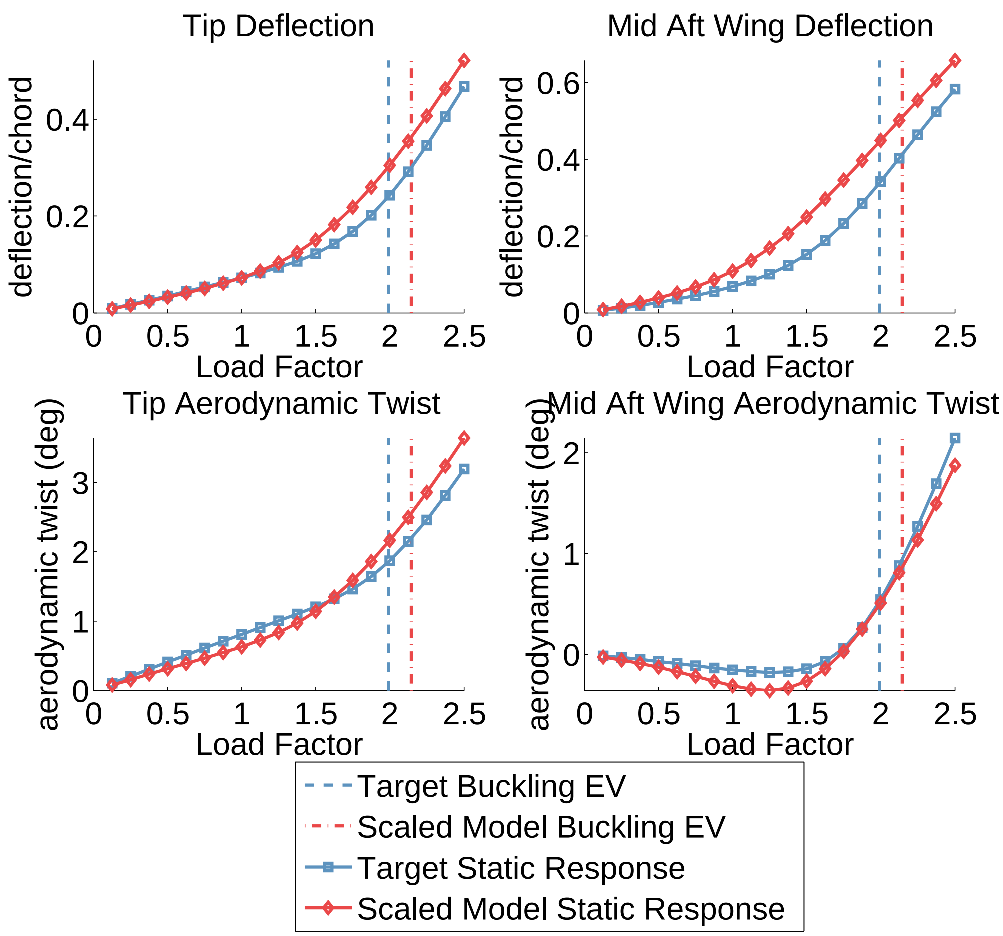

Figure A.11: Response to 2.5 nonlinear aeroelastic trim loads.

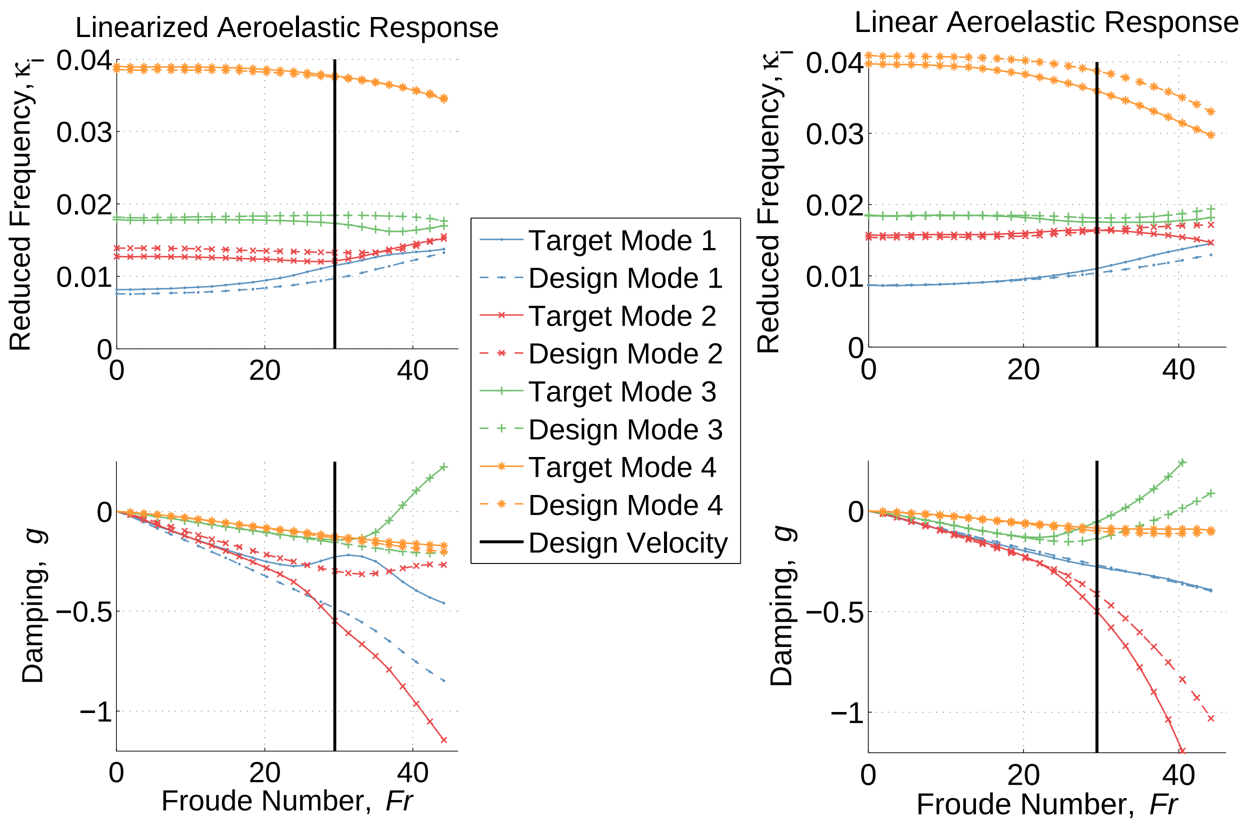

(a) Stiffness linearized about $1g$ nonlinear trim.

(b) Undeformed stiffness.

Figure A.12: Dynamic aeroelastic response.

Vibration Eigenpairs – 3, Buckling Eigenpairs – 1, With Linear Static Matching

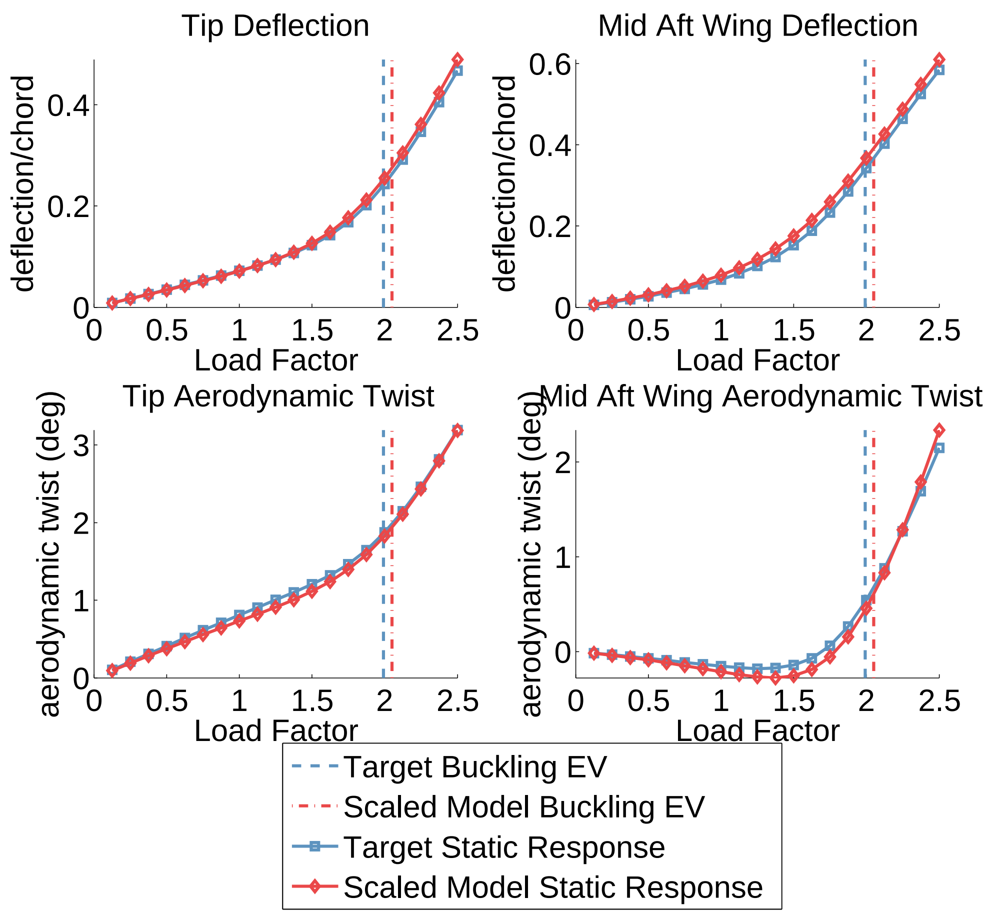

Figure A.13: Response to 2.5 nonlinear aeroelastic trim loads.

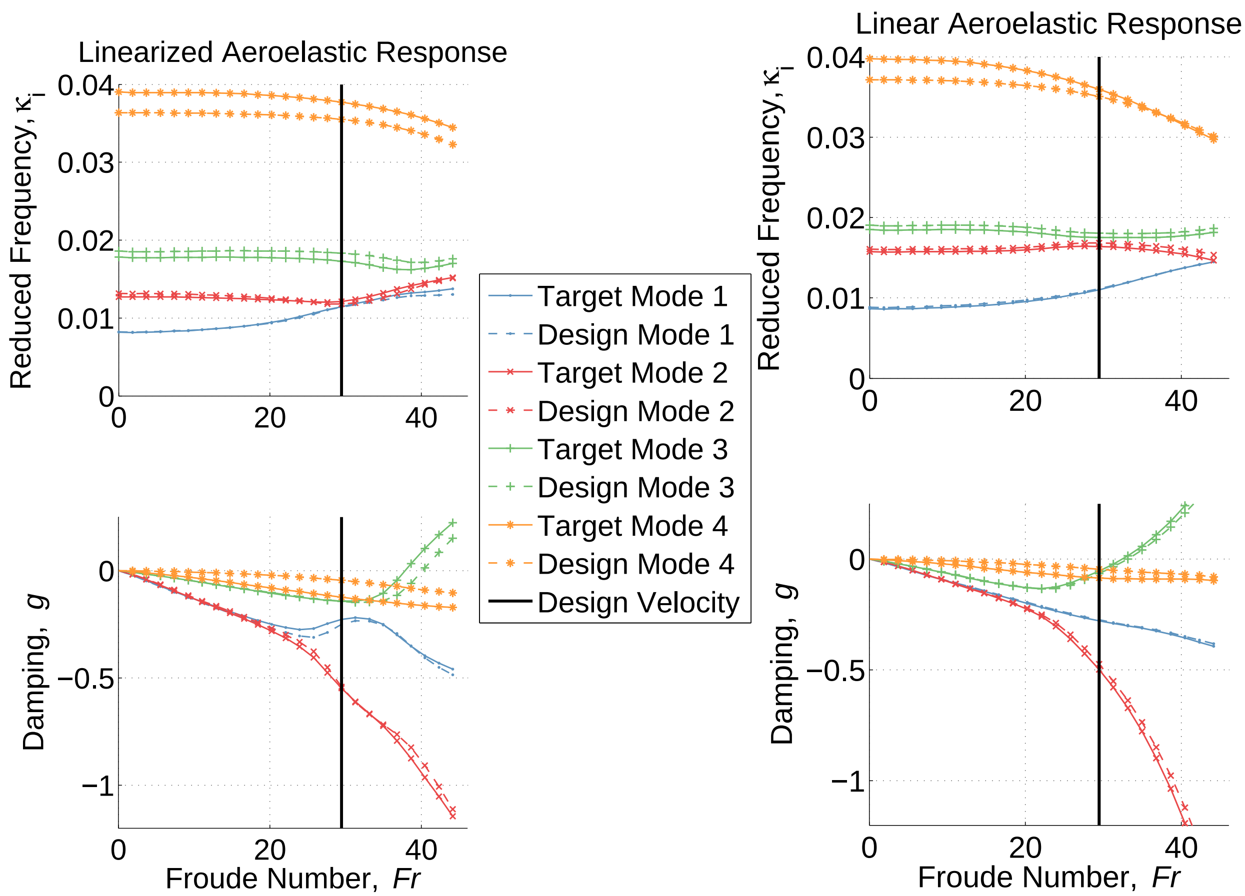

(a) Stiffness linearized about $1g$ nonlinear trim.

(b) Undeformed stiffness.

Figure A.14: Dynamic aeroelastic response.

Vibration Eigenpairs – 6, Buckling Eigenpairs – 1, With Linear Static Matching

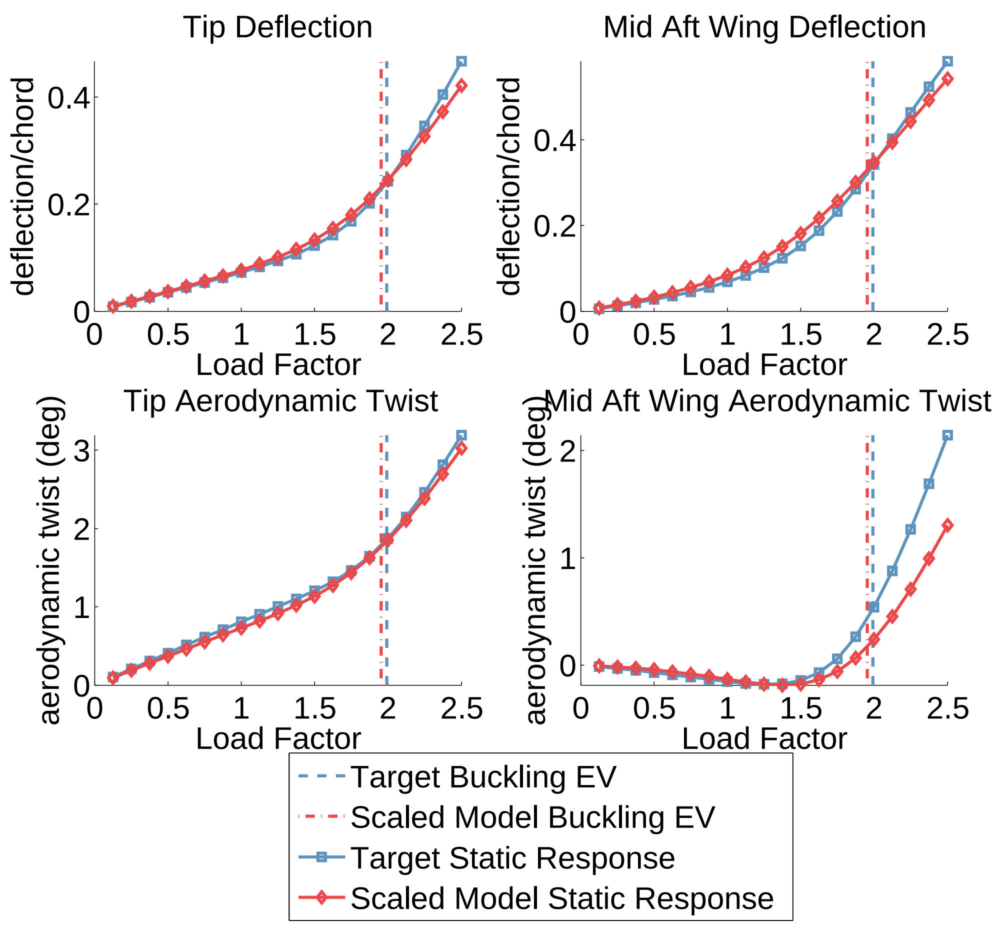

Figure A.15: Response to 2.5 nonlinear aeroelastic trim loads.

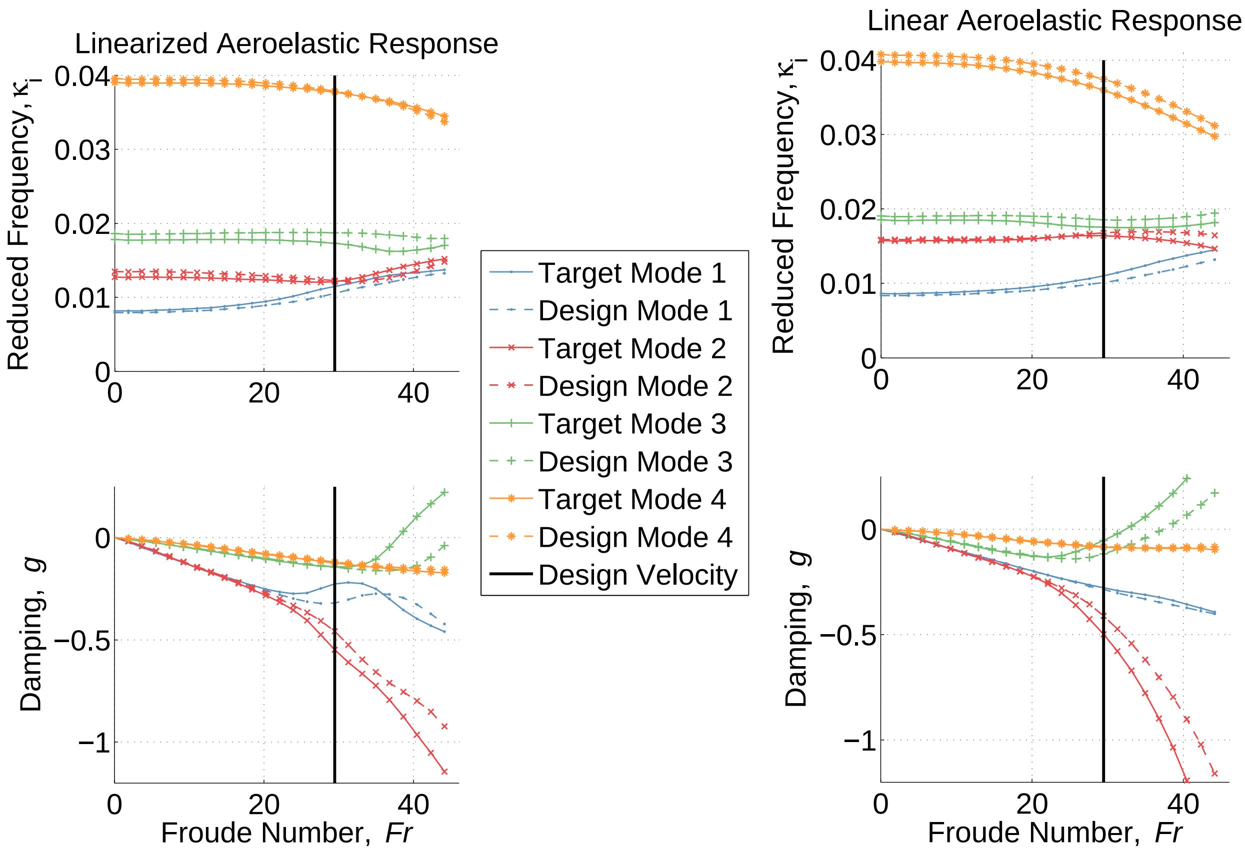

(a) Stiffness linearized about $1g$ nonlinear trim.

(b) Undeformed stiffness.

Figure A.16: Dynamic aeroelastic response.

A.2 ESL Tables

Table A.4: Target model properties.

Fig. 2.10 Label	Section	Dimension (ft)	Nonstructural Mass
	Forward Wing		
t_{sk}	Skin Thickness	0.0250	
t_{fa}	Fore/aft Web Thickness	0.0833	
t_c	Center Web Thickness	0.0833	4 slug/ft^2
t_r	Rib Thicknesses	0.0250	
m	Discrete Masses		10.06 slug
d_c	Box Chord	9.27	
d_t	Box Thickness	0.70	
d_s	Rib Spacing	4.88	
	Aft Wing		
t_{sk}	Skin Thickness	0.0250	
t_{fa}	Fore/aft Web Thickness	0.0250	
t_c	Center Web Thickness	0.0250	1.33 slug/ft^2
t_r	Rib Thicknesses	0.0250	
m	Discrete Masses		0.831 slug
d_c	Box Chord	2.35	
d_t	Box Thickness	0.35	
d_s	Rib Spacing	2.43	

Table A.5: Scaled model dimensions.

	Scaled Model from Traditional Linear Method	Scaled Model from Nonlinear Method
Forward Wing		
Spar width (in)	1.4810	2.1741
Spar height (in)	0.4398	0.3755
Spar running mass (slug/ft)	3.967E-3	2.854E-3
Rung radius (in)	0.3047	0.1816
Rung running mass (slug/ft)	0.0	0.0
Discrete masses (slug)	2.015E-2	1.591E-2
Rung spacing (in)	6.51	6.51
Ladder spacing (in)	2.47	2.47
Aft Wing		
Spar width (in)	0.8882	0.6305
Spar height (in)	0.1972	0.2455
Spar running mass (slug/ft)	1.270E-3	2.355E-03
Rung radius (in)	0.0273	0.0459
Rung running mass (slug/ft)	1.426E-3	2.660E-3
Discrete masses (slug)	5.396E-4	9.9156E-4
Rung spacing (in)	3.24	3.24
Ladder spacing (in)	1.88	1.88

Table A.6: Weight breakdown of target and scaled designs. Weights are in pounds.

	Full Scale Target	Target at 1/9th Scale	Scaled Model from Traditional Linear Design	Scaled Model from Nonlinear Method
Wings Structural	26,285	36.06	41.59	47.27
Wings Nonstructural	46,792	64.19	60.95	51.77
Wings Total	73,077	100.24	102.54	99.04
Fuselage (Rigid)	26,923	36.93	34.64	38.14
Total	100,000	137.17	137.17	137.17

Table A.7: Normalized modal frequencies.

Mode Number	Target Full Scale Model	Scaled Model from Traditional Linear Method	*Error*	Scaled Model from Nonlinear Method	*Error*
1	0.0173	0.0168	*2.7543 %*	0.0177	*2.4625 %*
2	0.0315	0.0304	*3.3249 %*	0.0306	*2.8669 %*
3	0.0370	0.0368	*0.6800 %*	0.0379	*2.3119 %*
4	0.0795	0.0808	*1.6268 %*	0.0804	*1.0752 %*
5	0.0906	0.0927	*2.3175 %*	0.0914	*0.8819 %*
6	0.1062	0.1084	*2.0997 %*	0.0999	*5.8808 %*
7	0.1573	0.1551	*1.3494 %*	0.1252	*20.4094 %*
8	0.1767	0.1682	*4.8272 %*	0.1653	*6.4722 %*
9	0.1919	0.1872	*2.4577 %*	0.1977	*3.0343 %*
10	0.2342	0.2105	*10.1157 %*	0.2267	*3.2086 %*